PB-227 347

LIDAR STUDIES OF STACK PLUMES IN RURAL AND URBAN ENVIRONMENTS

STANFORD RESEARCH INSTITUTE

PREPARED FOR
ENVIRONMENTAL PROTECTION AGENCY

OCTOBER 1973

DISTRIBUTED BY:

NTIS
National Technical Information Service
U. S. DEPARTMENT OF COMMERCE

PB 227 347
EPA-650/4-73-002

LIDAR STUDIES OF STACK PLUMES IN RURAL AND URBAN ENVIRONMENTS

by

Warren B. Johnson, Jr., Robert J. Allen, and William E. Evans

Stanford Research Institute
333 Ravenswood Avenue
Menlo Park, California 94025

Contract No. CPA 70-49
Project Element No. 1AA009

EPA Project Officer: Francis Pooler, Jr.

Meteorology Laboratory
National Environmental Research Center
Research Triangle Park, North Carolina 27711

Reproduced by
NATIONAL TECHNICAL
INFORMATION SERVICE
U S Department of Commerce
Springfield VA 22151

Prepared for

OFFICE OF RESEARCH AND DEVELOPMENT
U.S. ENVIRONMENTAL PROTECTION AGENCY
WASHINGTON, D.C. 20460

October 1973

This report has been reviewed by the Environmental Protection Agency and approved for publication. Approval does not signify that the contents necessarily reflect the views and policies of the Agency, nor does mention of trade names or commercial products constitute endorsement or recommendation for use.

BIBLIOGRAPHIC DATA SHEET	1. Report No. EPA-650/4-73-002	2.	3. Recipient's Accession No.

4. Title and Subtitle

LIDAR STUDIES OF PLUMES IN RURAL AND URBAN ENVIRONMENTS

5. Report Date: October 1973

6.

7. Author(s)

Warren B. Johnson, Robert J. Allen, and William E. Evans

8. Performing Organization Rept. No. 8509

9. Performing Organization Name and Address

Stanford Research Institute
333 Ravenswood Avenue
Menlo Park, California 94025

10. Project/Task/Work Unit No. 1AA009

11. Contract/Grant No. EPA CPA 70-49

12. Sponsoring Organization Name and Address

Meteorology Laboratory
National Environmental Research Center
Research Triangle Park, N.C. 27711

13. Type of Report & Period Covered: Final

14.

15. Supplementary Notes

16. Abstracts

Experimental results are presented from field studies of smoke plume diffusion and pollution-layer structure in both rural and urban areas, using the Mark VIII mobile lidar (laser radar) system. This new system was first applied to study the behavior of smoke plumes from the 250-m stacks of a large coal-burning power plant, the Homer City Generating Station, in western Pennsylvania. Examples from the Homer City study of characteristic changes in plume diffusion and low-level aerosol structure resulting from time-varying meteorological conditions are presented in the form of vertical plume cross sections. Helicopter-measured SO_2 cross sections and the lidar-obtained smoke cross sections are compared on a case-study basis. Estimates of diffusion parameters derived from the lidar observations are compared with those used in a fluctuating plume diffusion model.

The mobile lidar observations in urban areas (San Jose, California, and St. Louis, Missouri) reveal significant variabilities in the pollution-layer structure associated with urban effects, transitional meteorological conditions, and apparent convective influences.

An analysis of the eye-safety aspects of lidar use in the atmosphere is also included. It is pointed out that the probability of eye damage from lidar usage under current operational procedures is extremely small. However, remedial suggestions are offered for reducing the eye hazard even further.

17. Key Words and Document Analysis. 17a. Descriptors

Lidar
Laser radar
Plume dispersion
Mixing-layer structure
Diffusion modeling
Air pollution meteorology

17b. Identifiers/Open-Ended Terms

17c. COSATI Field/Group

18. Availability Statement	19. Security Class (This Report)	21. No. of Pages
Unlimited	UNCLASSIFIED	109 ///
	20. Security Class (This Page) UNCLASSIFIED	22. Price

CONTENTS

LIST OF ILLUSTRATIONS vii

LIST OF TABLES ix

ACKNOWLEDGMENTS xi

I INTRODUCTION 1

A. Background 1
B. Nature and Objectives of This Study 2

II LIDAR TECHNIQUES AND INSTRUMENTATION 5

A. Techniques 5
B. Instrumentation 7

III HOMER CITY STACK PLUME EXPERIMENT 11

A. Objectives 11
B. Experimental Techniques 11
C. Data Summary 15
D. Observed Plume Characteristics 15
1. Plume Evolution with Time During Transitional Periods 17
2. Time-Averaged Cross Sections 21
3. Plume Trapping: Relation to Ambient Atmospheric Stratification 23
4. Plume Condensation 26

E. Estimates of Plume Dispersion 29
F. Comparison of Lidar Data with Plume SO_2 Cross Sections Observed by Helicopter 32

IV SAN JOSE URBAN POLLUTION-LAYER TEST 37

V ST. LOUIS URBAN POLLUTION-LAYER EXPERIMENT 43

A. Objectives 43
B. Experimental Techniques 44

Preceding page blank

C. Data Summary 45
D. Results 45

VI RELEVANT SUBSEQUENT LIDAR APPLICATIONS 55

A. Diurnal Variation of the St. Louis Mixing Layer (NSF/SRI METROMEX Projects) 55
B. Spatial and Temporal Variations of the Los Angeles Mixing Layer (EPA Project) 57

VII CONCLUDING REMARKS 61

REFERENCES 63

APPENDIX A--Mark VIII Lidar System Details: Reprint of "Laser Radar (LIDAR) for Mapping Aerosol Structure," by R. J. Allen and W. E. Evans A-1

APPENDIX B--Lidar Data Summary, Homer City Experiment B-1

APPENDIX C--Lidar Data Summary, St. Louis Experiment C-1

APPENDIX D--Design Considerations for an Eye-Safe Lidar System D-1

ILLUSTRATIONS

1	SRI/EPA Mark VIII Lidar System Installed in Van for May 1970 Study of Diffusion of Stack Plumes from Large Power Plants in Western Pennsylvania	8
2	Locations of Lidar Sites Used for Observations of the Stack Plume from the Homer City Generating Station	13
3	Schematic Plan View of Typical Lidar Observational Technique for Plume Studies	14
4	Time Series of Smoke Plume Cross Sections observed by Mark VIII Lidar 2.5 km Downwind of 250-m Stack of Homer City Generating Station, Pennsylvania on 9 May 1970	18
5	Time Series of Vertical Plume Cross Sections on 9 May 1970, Except for Upper Left Photo that is a Zenith Scan Through the Haze Layer	20
6	Quasi-instantaneous (15 to 30 sec) Plume Cross Sections (top 10 photos) on 11 May 1970 and Corresponding 45-min Composite ("average") Cross Sections (bottom) at Downwind Distances of 1 km (left) and 2 km (right) from the Stack	22
7	Composite Cross Sections Showing Plume Trapping at 1500 m Height	24
8	Example of the Trapping of a Plume Rising in a Turbid Ambient Haze Layer	25
9	Time Evolution of Plume Structure at 2.5 km Downwind Within a Multilayered Haze Structure	27
10	Example of Cloud Formation Within the Smoke Plume 3 km Downwind from Stack	28
11	Comparison of Helicopter SO_2-(left) and Lidar Particulate-(right) Cross Sections for Two Cases During Homer City Experiment	34
12	Three of the Helicopter SO_2 Cross Sections Used for the Plume-Height Comparison in Table III-4	35

13 Height/Distance (Photos A, B, and C) and Height/Time (Photo D) Cross Sections Obtained During Special Tests of the Modified Mark VIII Lidar System in the Menlo Park, California Area 38

14 Lidar-Observed Time/Height Cross Sections of the Urban Haze Layer over San Jose, California on 11 December 1970 39

15 St. Louis Lidar Route and Checkpoints 46

16 Time Changes in Pollution-Layer Structure Approximately Along Wind Through East St. Louis 49

17 Vertical Pollution-Layer Structure in an Approximately Crosswind Direction Along I-70 in St. Louis 51

18 Vertical Pollution-Layer Structure in the Downwind Direction Along I-55 from the Arch in Central St. Louis 52

19 Vertical Pollution-Layer Structure in a West-East Direction Along I-270 Downwind of Central St. Louis 54

20 Height/Time Cross Section of the Aerosol Structure over St. Louis on 13 August 1971 as Observed by SRI/EPA Mark VIII Lidar System 56

21 Time Evolution of the Los Angeles Aerosol (Smog) Layer as Observed During an Early Afternoon Period by the Mark VIII Lidar over a South-North Route on the East Side of the Basin 58

22 Location/Time Contours of Lidar-Observed Aerosol Mixing Height (in Meters) Along a 70-Mile Freeway Loop over the Los Angeles Basin on 21 September 1971 59

23 Mobile Lidar Routes, Los Angeles Basin, September 1972 . . . 60

TABLES

1	Characteristics of the Mark VIII Mobile Lidar System	9
2	Chronological Summary: Homer City Lidar Experiment	16
3	Power Plant Precipitator Operation During the Homer City Lidar Experiment	17
4	Comparison of Observed and Calculated Values of Plume Radius-to-Dispersion Ratio (R/σ_y^*)	31
5	Comparison of Plume Heights (above stack base) Obtained from Helicopter SO_2 Cross Sections and Lidar Particulate Cross Sections	33
6	Comparison of Lidar-Observed Haze-Layer Tops over San Jose, California, with Mixing-Depth Estimates from Helicopter Profile Data and a Mixing-Depth Model	41
7	Data Summary: St. Louis Lidar Experiment	47

ACKNOWLEDGMENTS

The authors would like to give credit to a number of individuals who have made significant contributions to this project. With regard to personnel at Stanford Research Institute, Mr. Norman Nielsen played a key role throughout the course of the work. He helped to design the Mark VIII lidar system and was in charge of fabrication and testing of the system. In addition, he participated extensively in each of the field experiments. Mr. Russell Wolfram designed and supervised construction of the range-compensation module of the lidar system. Mr. Albert Smith participated in two of the experiments and assisted in the data analysis, as did Miss Joyce Keoloha. Dr. Walter Dabberdt conducted the comparison of the lidar and helicopter mixing-layer data from the San Jose tests. Mr. Ronald Collis furnished supervision and support throughout the course of the project.

We also wish to express appreciation for the technical and financial support furnished on behalf of the sponsoring agency by Dr. Francis Pooler and Mr. Lawrence Niemeyer of the Meteorology Laboratory, U.S. Environmental Protection Agency. In addition, the help of Mr. Frank Schiermeier of the same group in furnishing data from other elements of the LAPPES program was particularly valuable.

Preceding page blank

I INTRODUCTION

A. Background

Prediction of near-ground pollutant concentrations is a central factor in air pollution control and air resource management. In carrying out this role, however, the air pollution meteorologist and chemist must deal with the fact that pollutants move, disperse, and change character in a three-dimensional, dynamically open atmospheric system. Achievement of a fuller understanding of these processes, as needed to develop techniques for accurately predicting near-gound concentrations, requires that detailed observations be obtained in three dimensions within the atmospheric medium. In this regard, one of the classic problems has been to obtain detailed measurements in the vertical. Such measurements have been particularly needed in studies of diffusion from elevated sources such as tall stacks.

Consequently, increasing attention has been given to the capabilities of atmospheric indirect sensing techniques for supplementing conventional direct sounding systems that use balloons or instrumented aircraft. A variety of types of remote probing systems are under active development, including acoustic sounders (Shaw, 1972; McAllister, 1972; Hall, 1972; Little, 1972; Uthe and Shaw, 1973), passive radiometric systems (Hosler and Lemmons, 1972), and various laser techniques. Of the latter, lidar (laser radar) has proven to be especially promising. Lidar applications in air pollution studies have been discussed extensively in the literature (Johnson, 1969a; Collis, 1970; Barrett and Ben-Dov, 1967; Hamilton, 1966, 1967, 1969). The advantages of the lidar technique basically stem from its ability to obtain useful measurements remotely and at a high density in space and time.

This report describes the results of an observational program that were obtained with the van-mounted Mark VIII mobile lidar system developed by Stanford Research Institute (SRI) with partial support from the U.S. Environmental Protection Agency (EPA) under this contract. This lidar system was designed particularly for air pollution applications and has a number of advanced features that are described in Section II and in Appendix A.

B. Nature and Objectives of This Study

The observational program included lidar experiments at one rural and two urban sites:

Homer City Generating Station (HCGS), Pennsylvania (rural)
San Jose, California (urban)
St. Louis, Missouri (urban)

The Pennsylvania experiment was the major part of the study and entailed lidar measurements of smoke plumes from the 250-m stacks of a coal-burning power plant (the HCGS). Results from a similar lidar study of nearby Keystone Generating Station have been previously reported (Johnson, 1969b; Johnson and Uthe, 1971). The Keystone and Homer City investigations have been carried out in conjunction with a coordinated EPA program called the Large Power Plant Effluent Study (LAPPES). As a part of this program, ground and airborne measurements of sulfur dioxide (SO_2) concentrations and wind and temperature profiles were taken quasi-concurrently with the lidar observations. The LAPPES data collected during the several experimental periods have been summarized by Schiermeier and Niemeyer (1970) and Schiermeier (1970, 1972a, 1972b); preliminary analyses have been reported by Pooler and Niemeyer (1970). One of the specific aims of the LAPPES was to develop and validate transport and diffusion models for calculating ground-level concentrations of effluents from large power

plants with tall stacks, since the results from previous studies of plumes from short stacks cannot simply be extrapolated with any degree of reliability. To accomplish this goal requires a better understanding of plume behavior; therefore, this was the main purpose of our lidar studies of the smoke plumes from these tall stacks. Although particulate emission is not the major air pollution problem associated with power plants (because of the efficiency of modern fly-ash removal devices), the smoke serves as a convenient tracer for study of diffusion processes. Because the particles are small, their diffusion should be essentially identical with that of a gas such as SO_2, the primary pollutant of interest.

The urban studies in San Jose and St. Louis were conducted to test the feasibility of a lidar system for mapping the three-dimensional structure of the urban haze (pollution) layer, including plumes within this layer. Such information is needed to aid in the further development of air quality simulation models for urban areas.

II LIDAR TECHNIQUES AND INSTRUMENTATION

A. Techniques

The Mark VIII lidar system is basically composed of a laser transmitter that emits a very brief, high-intensity pulse of coherent light, and a receiver that detects the energy at the laser wavelength backscattered from the atmospheric aerosol as a function of range. The factors affecting the strength of this received signal are best discussed in terms of the lidar equation, which may be written in the form:

$$P_r(R) = K E R^{-2} \beta(R) \exp\left[-2 \int_0^R \sigma(r)\, dr\right] , \qquad (2.1)$$

where

P_r = power collected (at a given instant) by the primary receiver optics from atmospheric backscatter of laser radiation

R = range

K = constant based on lidar characteristics

E = energy transmitted into the atmosphere

σ = volume extinction coefficient

β = volume backscatter coefficient.

This relation assumes a constant energy density across the beam, randomly distributed scatterers within the effective scattering volume, Bouguer's law of attenuation, and neglects multiple scattering effects. These assumptions are normally valid because of the very narrow field of view of lidar systems ($\approx$1 mrad).

Preceding page blank

Equation (2.1) shows that the lidar signature is dependent on the range distribution of two optical parameters: the volume backscatter coefficient (β) and the volume extinction coefficient (σ). The exponential term containing σ represents the two-way transmittance to the backscattering volume, and it can be seen that β and σ act in opposite directions on P_r. The backscatter coefficient is a function of the particle number concentration, size distribution, and optical properties, as is the extinction coefficient. However, since β enters into Eq. (2.1) as a direct factor (rather than in an integral expression, as does σ), it is apparent that rapid changes in the received signal can be ascribed primarily to β.

When atmospheric attenuation can be ignored, as in the case of a relatively clear atmosphere (Uthe and Johnson, 1971), the lidar backscatter signature provides a rapid means of qualitatively describing the distribution of atmospheric particles along an observing path. Multiple lidar observations can then be assembled to provide knowledge of the spatial or temporal variations of aerosol structure.

With the Mie scattering theory, quantitative mass concentration estimates can be derived from lidar data if the size distribution and optical characteristics of the aerosols are known or assumed. This has been successfully demonstrated but is a rather complex procedure (Johnson and Uthe, 1971).

The variation in optical scattering properties may be the result of either changes in the particle number density, or changes in particle size distribution, or optical properties of the particles. Although this nonuniqueness exists in single wavelength lidar measurements, lidar observations of particulate plumes or layers show boundaries and variations of meteorological interest regardless of the physical or chemical nature of the aerosol. The relative optical density of particulates as

observed by the lidar technique has been related to meteorological features by a number of investigators (Johnson, 1971; Johnson and Uthe, 1971; Uthe and Johnson, 1971; Gambling and Bartusek, 1971; Olsson et al., 1971; McCormick and Fuller, 1971; Viezee and Oblanas, 1969).

In lidar studies of smoke plumes or urban pollution layers, a frequently observed relationship is that between the vertical structure of temperature and aerosol density. Atmospheric stability associated with a temperature inversion normally limits convective penetration of aerosols across the inversion boundary; hence, strong vertical aerosol gradients that are easily identified on a lidar backscatter signature may form at the top of the mixing layer. The height of the mixing layer is one of the more important parameters in modeling the diffusion and transport of pollutants of near-surface origin. Pollutants are often effectively trapped beneath an elevated inversion, resulting in a greater aerosol density within the mixing layer. Experimental results along these lines are presented in Sections III, IV, V, and VI of this report.

B. Instrumentation

The Mark VIII lidar system in its initial form is shown in Figure 1, while Table 1 lists the characteristics of the system. A more detailed description is furnished in Appendix A. The Mark VIII and Mark IX* lidars are unique for their capability of video disc recording of large quantities of lidar data and rapid electronic processing of the data to obtain range-corrected, intensity-modulated CRT displays of particulate distributions in real-time. Also, these lidars use coaxial transmitter and receiver optics to minimize geometric effects in the backscatter

---

*The SRI Mark IX mobile lidar system, which is a similar but improved version of the Mark VIII, was recently designed and built by SRI with internal funding.

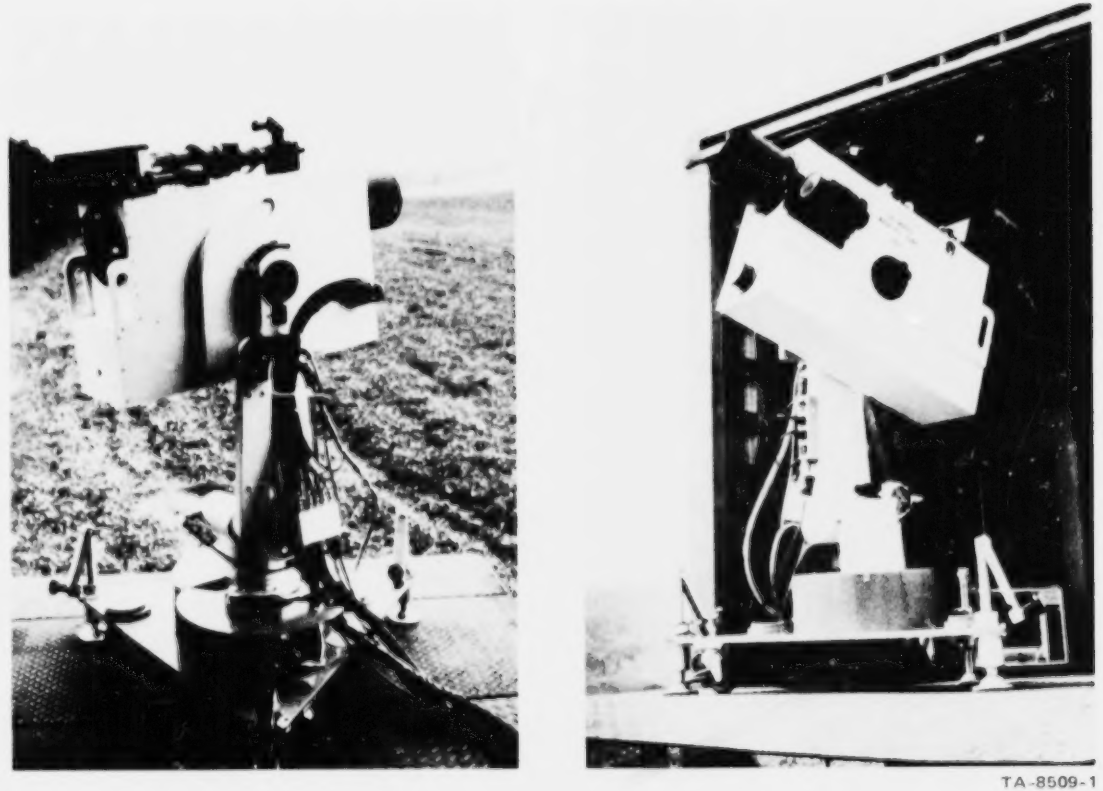

TA-8509-1

FIGURE 1 SRI/EPA MARK VIII LIDAR SYSTEM INSTALLED IN VAN FOR MAY 1970 STUDY OF DIFFUSION OF STACK PLUMES FROM A LARGE POWER PLANT IN WESTERN PENNSYLVANIA

Table 1

CHARACTERISTICS OF THE MARK VIII MOBILE LIDAR SYSTEM

Characteristics	Description
Transmitter	
Laser rod	Ruby (3/8 x 3 inches)
Wavelength (Å)	6943.0 ± 0.4
Beamwidth (mrad)	0.8
Optics	Lens (2-inch), coaxial with receiver telescope
Pulse energy (joules)	0.9
Pulse length (nsec)	30
Peak power (MW)	30
Q-switch	Pockels cell
Maximum PRF (pulses/min)	30
Cavity cooling	Refrigerated water
Receiver	
Optics	Newtonian reflector (6-inch)
Field of view (mrad)	Adjustable, 1 to 5
Predetection filter passband width (Å)	10
Detector	RCA-7265 PMT (S-20 photocathode)
Frequency response	Direct writing: >100 mHz Recording: 4.5 mHz
Automatic gain compensation	Inverse range-squared gain control of PMT
Signal conditioning	Log or linear amplification
Scanning and firing	
Elevation scan (degrees/shot) (mode 1)	Motor driven and selectable between 0.5 and 10
Azimuth scan	Motor driven
Firing rate (shots/min) (mode 2)	Selectable, 1 to 30
Mobile capability (Mode 3)	
Firing density (shots/mile)	Selectable, 10 or 20 (controlled by vehicle odometer)
Vehicle speed while firing (mi/hr)	Up to 60
Data recording and display	
Recording and storage	Magnetic video disk recorder
Direct recording	CRT oscilloscope photographs
Displays	Intensity-modulated range height indicator (RHI), height/time or height/distance, cross-sectional displays; also conventional A-scope (amplitude versus time)

signature, which permits valid data to be obtained at a shorter distance from the lidar than is possible with bistatic systems.

As indicated in Table 1, three basic modes of lidar operation are possible with the Mark VIII system:

- Mode 1--Van stationary; programmed lidar elevation scan. This produces a radar-type intensity-modulated, RHI fan-shaped display on an oscilloscope.
- Mode 2--Van stationary; lidar firing at programmed increments of time while pointing upward (or in any other direction). This produces an intensity-modulated, height/time cross-sectional display.
- Mode 3--Van moving; lidar firing at programmed increments of distance while pointing upward. This produces an intensity-modulated, height/distance cross-sectional display. Large areas can be mapped in this fashion.

For this study, successful field operations with the system were conducted under Modes 1, 2, and 3 at Homer City, San Jose, and St. Louis, respectively.

During the plume experiment at Homer City, the fast firing rate, in conjunction with the automatic elevation scanning feature, permitted detailed cross-sectional scans of most plumes to be completed within one minute. In addition, the RHI display capability has been an important advantage. It not only eliminates the need for costly and time-consuming digital calculations but also furnishes a quick look at the data in the field for experimental control in real-time. The resulting vertical cross sections can be analyzed individually or as time-average composites through multiple displays and photographic exposures. Hamilton (1969) has also carried out lidar plume studies along these lines, but with less advanced instrumentation.

III HOMER CITY STACK PLUME EXPERIMENT

A. Objectives

As mentioned in Section I, the objectives of this experiment were to:

- Test the improved capabilities of the newly developed Mark VIII lidar system for plume studies
- Use the lidar data to investigate the characteristics of the behavior and diffusion of the smoke plume from the Homer City Generating Station (HCGS)
- Compare the lidar plume measurements with SO_2 measurements from an instrumented helicopter operated by the EPA.

These objectives have been successfully achieved through the results of the field program, which will be discussed later in this section.

B. Experimental Techniques

The field program was conducted in the vicinity of Homer City, Pennsylvania, about 80 km northeast of Pittsburgh, during the period 29 April to 15 May 1970. Since at this time the lidar system had not yet been installed in a van, the equipment was boxed and transported by air to Pennsylvania, where it was installed on a temporary basis in a rented van for the duration of the experiment. Two motor-generator sets mounted in a pick-up truck provided the electrical power for field operation.

Before the data collection period, a field survey was conducted within a 10-km radius of the HCGS* to locate suitable lidar sites that

---

*Located 5 km SW of Homer City.

were accessible and would provide relatively unobstructed viewing of the HCGS stack plume. Of these predetermined sites, a total of six were used in the experiment, as indicated in Figure 2. The individual sites used for each observational period were selected on the basis of the wind direction prevailing at that time and the resulting plume orientation relative to the various sites.

The ideal geometric arrangement of plume and lidar for this situation is to have a horizontal distance, perpendicular to the plume centerline, of approximately 2 to 5 km between the lidar and the downwind plume portion of interest, as illustrated in Figure 3. This is because the basic lidar observational mode used for plume measurements consists of scanning the plume in the vertical plane, thus producing cross-sectional displays.

The geometric arrangement mentioned above has the plume close enough to the lidar to subtend a sufficiently large elevation angle to permit detailed measurements at 1° elevation angle increments, yet far enough away so that plume cross sections from elevation scans at other azimuth angles can also be obtained, as indicated in Figure 3.

During the Homer City experiment, the vertical plume scans were carried out automatically by the motor-driven, programmable elevation scan feature of the Mark VIII system. Such scans were usually carried out at a lidar firing rate of 20 shots/min and at elevation angle increments of 0.5°, 1°, or 2°. This permitted a plume scan covering a 20° to 90° elevation sector to be completed within 30 sec to 2 min. Occasionally, overhead scans covering a 90° to 135° sector were conducted to observe the general ambient aerosol structure in the mixing layer.

Where possible, the lidar was positioned at each site so that it could be aimed in a direction approximately perpendicular to the plume axis, as in Figure 3. (On a few occasions when the wind direction

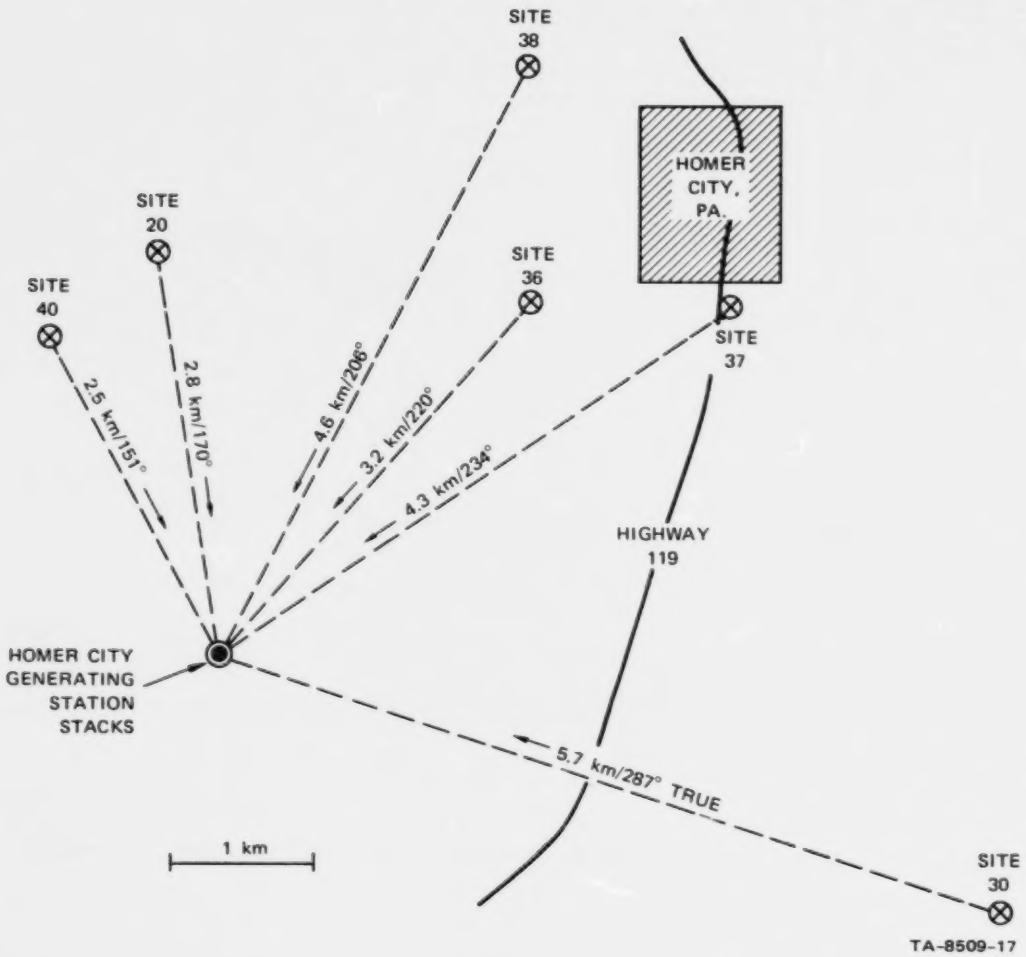

FIGURE 2 LOCATIONS OF LIDAR SITES USED FOR OBSERVATIONS OF THE STACK PLUME FROM THE HOMER CITY GENERATING STATION

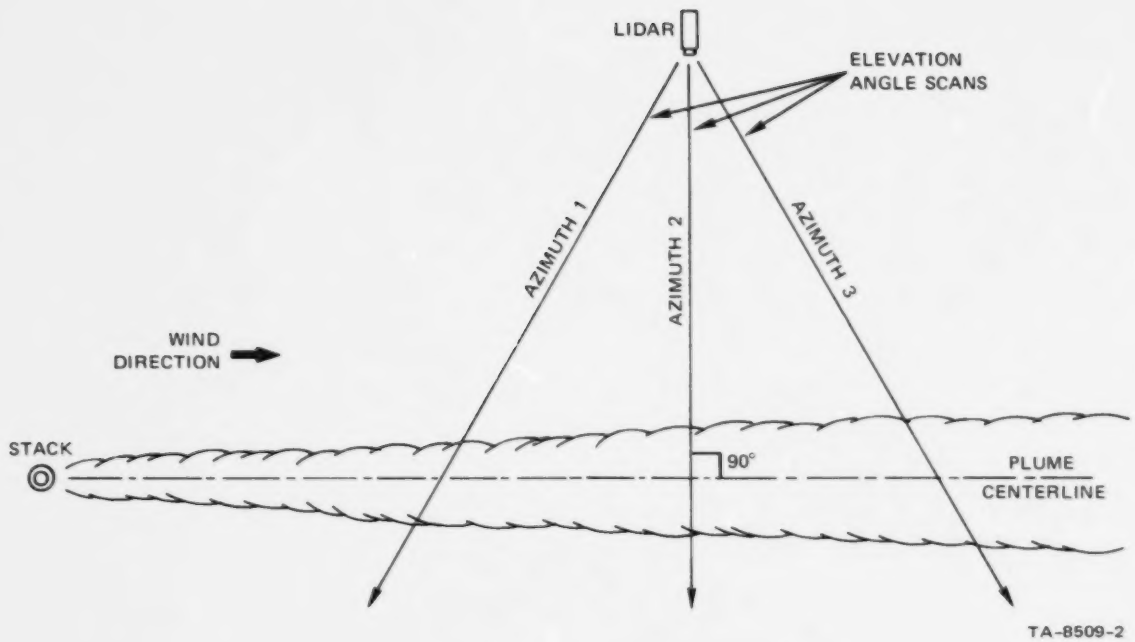

FIGURE 3 SCHEMATIC PLAN VIEW OF TYPICAL LIDAR OBSERVATIONAL TECHNIQUE FOR PLUME STUDIES

changed substantially, the lidar van had to be moved to another site.) Vertical cross sections through the plume were normally obtained at several azimuth angles and thus at several downwind distances from the stack so that spatial differences in plume behavior and diffusion could be documented.

C. Data Summary

A chronological field activities and data summary is given in Table 2. A more detailed data summary is included in Appendix B.

As may be noted, weather conditions were far from ideal during the experimental period, with snow occurring on 6 May and rain occurring on several days. In addition, data were lost in a few cases because of equipment malfunctions. (This was perhaps to be expected during the first field trials of a completely new and sophisticated electro-optical system that had been completely designed and built "from scratch" in less than four months immediately preceding the experiment.)

Despite these problems, a large amount of high-quality data was obtained, particularly on 3, 9, 11, and 15 May. These experimental results will be presented in the next section.

D. Observed Plume Characteristics

In this section, we present a number of the lidar cross sections of the smoke plume from the HCGS obtained during the May 1970 observational period. These data have been selected to illustrate certain features of the plume structure and behavior, some of which are observable only by means of the lidar technique. Throughout the observational period, the power plant's stack-gas particulate removal system (using electrostatic precipitators) was operated at least at 75% capacity (see Table 3) so that a very "clean" plume resulted with regard to particulates.

Table 2

CHRONOLOGICAL SUMMARY: HOMER CITY LIDAR EXPERIMENT

Date (1970)	Day	Site Number	Observational Periods (EST)	C.S.* Numbers	Number of C.S.	Remarks
29 Apr	Wed	--	---	--	--	Unpacked equipment
30 Apr -2 May	Thurs -Sat	--	---	--	--	Instrumentation check and recalibration
3 May	Sun	36	1601-1755	1-8	8	Upper inversion apparent
4 May	Mon	30	0756-1000	9-24	16	Very light winds, plume ill-defined; generator outage
5 May	Tues	37	0701-0709	25-26	2	Wind direction changing
		20	0922-0951	27-33	7	Wind direction changing
		37	1113-1141	34-38	5	Plume looping; equipment malfunction
6 May	Wed	30	0835-0905	39-42	4	Weather poor, snow flurries; Advisory Committee meeting
7 May	Thurs	37	1131-1501	43-69	27	Demonstration for Advisory Committee during AM
8 May	Fri	--	---	---	--	Laser down for repairs
9 May	Sat	37	0656-1452	70-153	84	
		36	1551-1653	154-164	11	Upper inversion apparent
10 May	Sun	37	0548-0651	165-174	10	Wind direction changing
		38	0858-1452	175-217	43	Rain started 1355 EST
11 May	Mon	38	0933-1053	218-235	18	Low ceilings earlier
		20	1230-1700	236-318	83	
12 May	Tues	20	1044-1506	319-391	73	Low ceilings earlier: data improperly recorded due to electronic malfunction
13 May	Wed	20	0820-0830	392-395	4	Low ceilings, light rain
			1419-1503	396-408	13	Equipment repaired; rain started 1605 EST
14 May	Thur	--	---		--	Poor weather all day
15 May	Fri	40	1008-1253	409-443	35	Rain earlier
		36	1414-1704	444-493	50	Very hazy, 2-3 mi visibility
Total cross-sections recorded				493		
Total lidar observations recorded				20,000 (approximate)		

*C.S.--Cross Section.

Table 3

POWER PLANT PRECIPITATOR OPERATION
DURING THE HOMER CITY LIDAR EXPERIMENT

(May 1970)	Time (EST)	Percentage of Precipitator Sections in Operation	
		No. 1 Stack	No. 2 Stack
1	0500-1100	75	100
3	All day	100	100
4	0500-1100	83	100
5	0500-1300	92	92
6	0500-1300	Stack off	83
7	0800-1700	Stack off	83
8	0500-1700	83	Stack off
9	0500-1700	83	Stack off
10	All day	100	Stack off
11	0500-1700	83	Stack off
12	0500-1700	83	Stack off
13	0500-1700	75	Stack off
15	0500-1700	75	Stack off

This plume was frequently virtually invisible to the eye at a short distance downwind from the plant, but was nevertheless consistently detected by the lidar at distances of several km.

1. Plume Evolution with Time During Transitional Periods

Figure 4 shows a time sequence of 15 plume cross sections during the period from 0656 EST to 1003 EST on 9 May 1970. In this instance, the lidar vertical scan intersects the plume at an angle of approximately 25° at about 2.5 km downwind of the stack. Because of this rather oblique viewing angle, the plume cross sections shown in this series appear about 2.5 times wider than the true plume width at

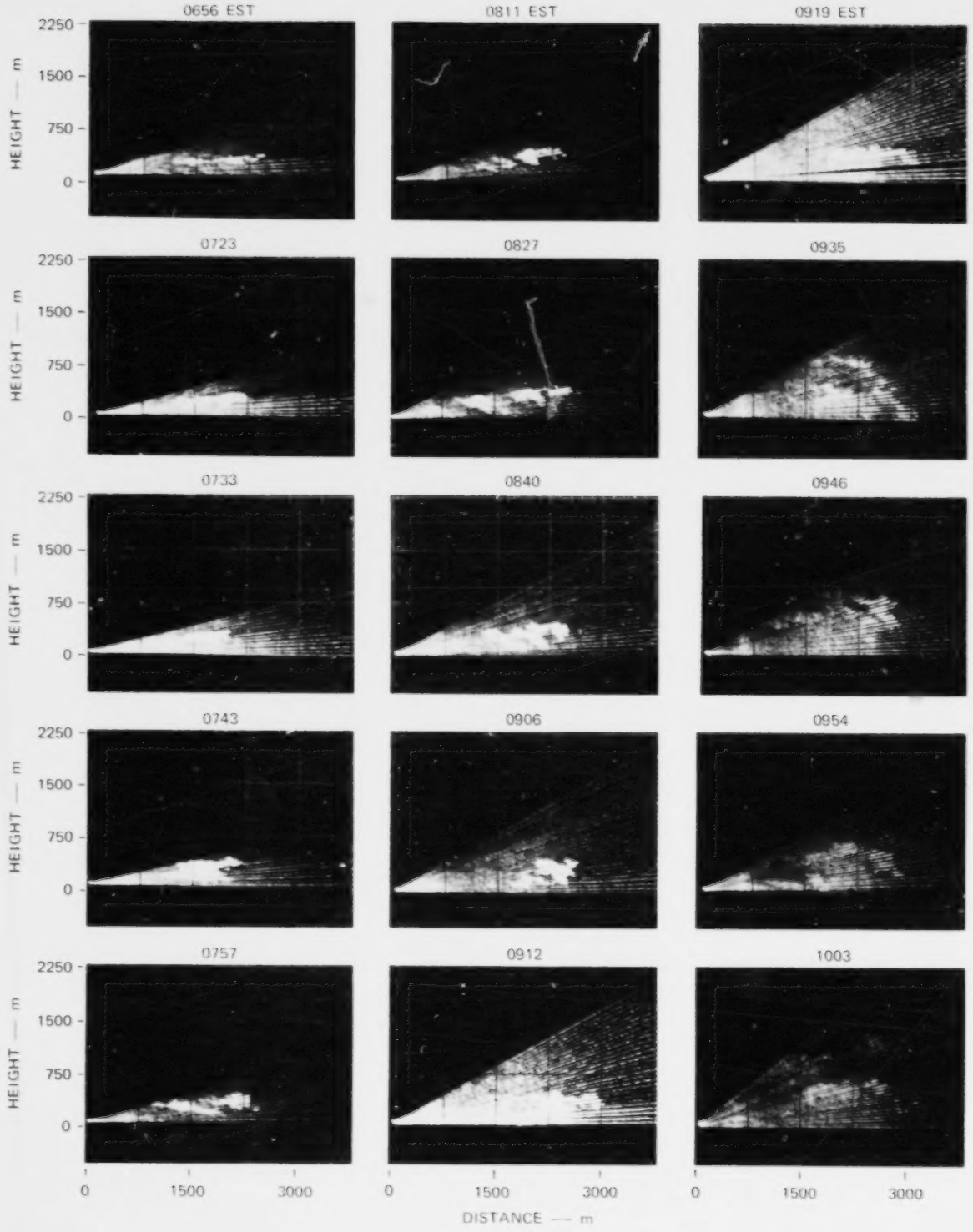

TA-8509-3

FIGURE 4 TIME SERIES OF SMOKE PLUME CROSS SECTIONS OBSERVED BY MARK VIII LIDAR 2.5 km DOWNWIND OF 250 m STACK OF HOMER CITY GENERATING STATION, PENNSYLVANIA ON 9 MAY 1970

the 2.5-km downwind distance. The power plant stack was located to the right of the lidar so that the cross sections in the figure are viewed roughly in the downwind direction.

The sky was clear during the early morning, with an estimated 7 mile visibility and with scattered cumulus clouds forming by 0730 EST. Surface winds were from the southwest at about 5 mi/hr, increasing to 10 mi/hr by 1000 EST.

The time change in the plume shape is quite dramatic as the atmospheric stability decreases during the course of the morning. The plume shape progresses from the typical fanning, tilting shape in the early morning--caused by the wind veering with height in stable conditions--to a partial ground fumigation by 0906 EST and full downward mixing by 0946 EST. Portions of the plume apparently begin to be mixed downward into the rising convective layer by 0827 EST. During the period from 0912 to 0935 EST, one area of the plume (on the right side of the cross sections in Figure 4) retains its identity as its height decreases, finally reaching the ground at 0935 EST. The plume just after exit from the stack was observed to be barely visible by eye at 0946 EST, indicating that the atmosphere dilution had become pronounced.

A related sequence of cross sections is depicted in Figure 5. This sequence was observed on the same day and during the same time period as those in the previous figure. However, in this case, the lidar was pointed at a different azimuth angle, such that it intercepted the plume axis at an angle of approximately 50°, at a downwind distance of about 3.5 km from the stack. The plume-width exaggeration in these cross sections is about 1.3.

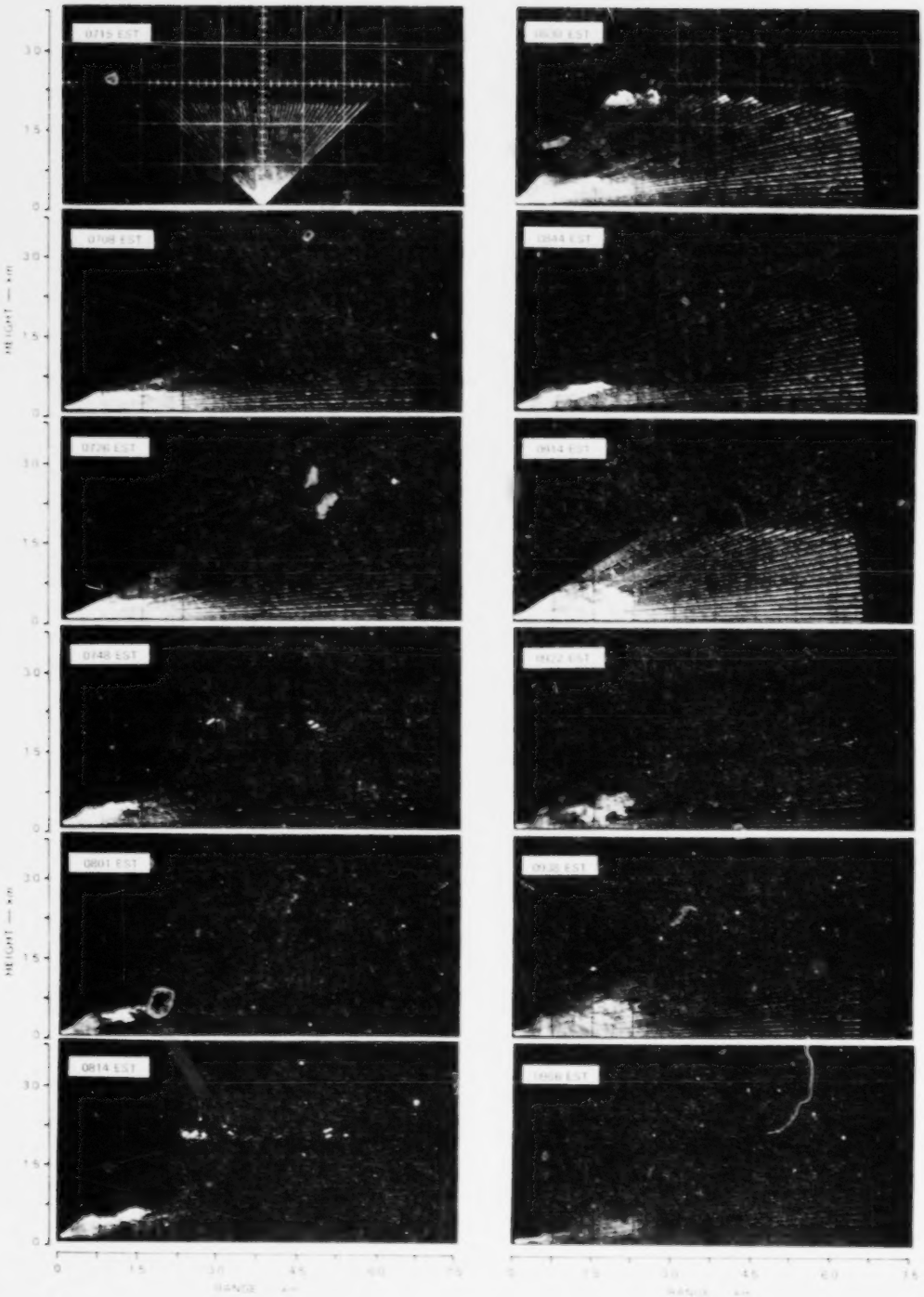

TA-8509-18

FIGURE 5 TIME SERIES OF VERTICAL PLUME CROSS SECTIONS ON 9 MAY 1970, EXCEPT FOR UPPER LEFT PHOTO, WHICH IS A ZENITH SCAN THROUGH THE HAZE LAYER

The cross sections are oriented at 55° to the plume axis, 3.5 km downwind from the stack.

Unfortunately, the plume turned out to be closer to the lidar than was desirable and caused somewhat poorer definition of the plume structure than in the previous sequence. However, the beginning of the fumigation at 0914 EST and the rather complete downward mixing at 0938 EST are still readily apparent at this distance from the stack (1 km farther than in Figure 4).

The first frame in Figure 5 shows the results of a zenith scan to measure the height of the haze layer in which the plume is embedded, which turns out to be 1900 m above the lidar. Scattered clouds later form near this haze top and are apparent in the plume photographs at 0748, 0814, and 0830 EST.

2. Time-Averaged Cross Sections

Figure 6 illustrates the averaging capability of the display system. The two bottom pictures represent time-averaged plume cross sections over approximately a 1-hr period, at downwind distances of 1 km (left) and 2.5 km (right). Five of the six individual quasi-instantaneous cross sections that were superimposed to develop the average cross sections are shown above each of the latter. These and other data from 11 May 1970 have been used to estimate plume dispersion as needed for input to a fluctuating-plume dispersion model, as described later in this section.

In view of the late-afternoon observational time of these data and the partly cloudy, light wind weather conditions prevailing at the time, the atmospheric stability was probably neutral to slightly unstable. The plume is well above the surface at 1 km downwind and quite compact. The hole in the plume bottom apparent at 1541 and 1600 EST is probably caused by the vortex-roll bifurcation phenomenon described by Scorer (1958) and previously observed in the lidar observations of the plume

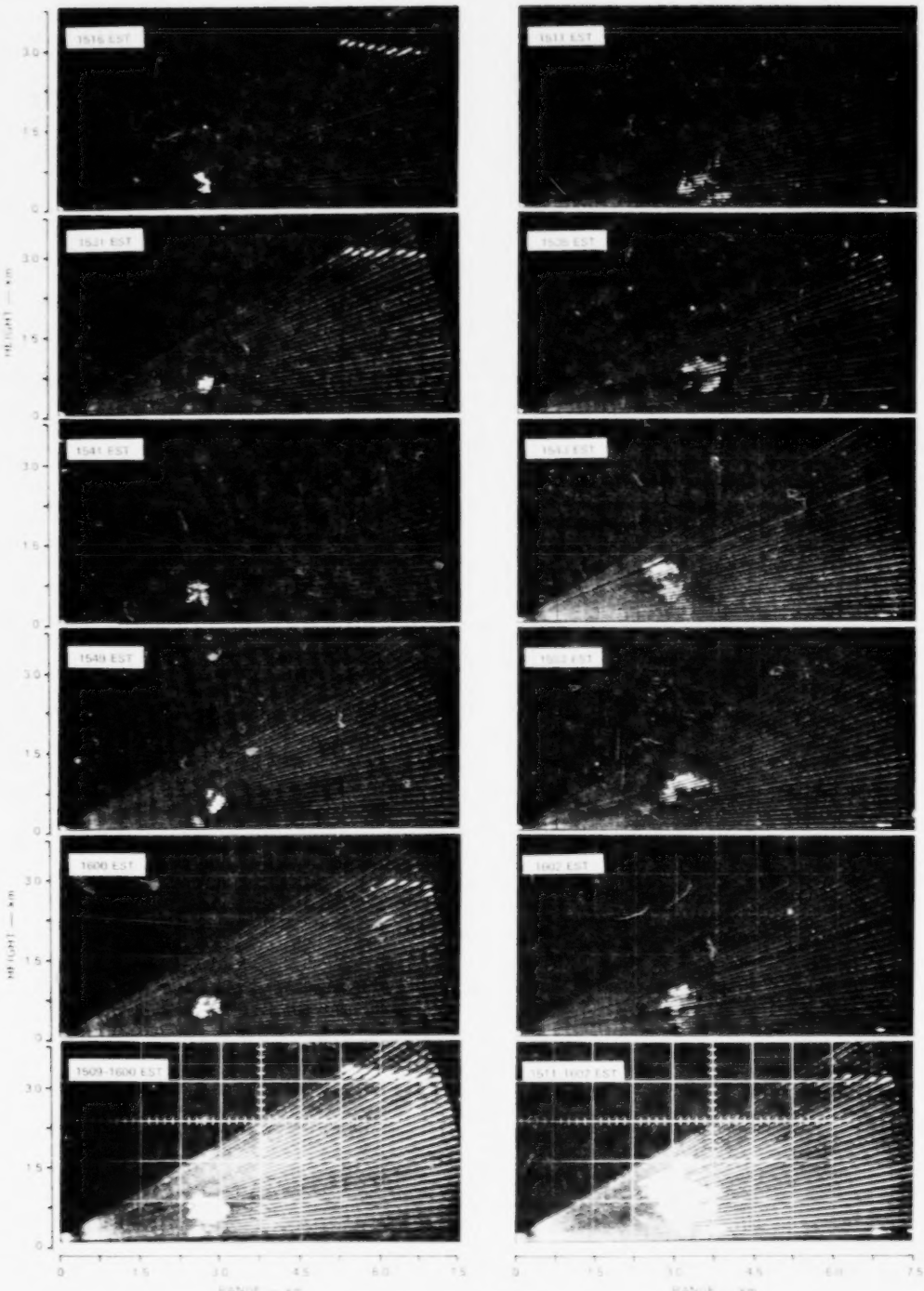

FIGURE 6 QUASI-INSTANTANEOUS (15 TO 30 SEC) PLUME CROSS SECTIONS (TOP 10 PHOTOS) ON 11 MAY 1970, AND CORRESPONDING 45-MINUTE COMPOSITE ("AVERAGE") CROSS SECTIONS (BOTTOM), AT DOWNWIND DISTANCES FROM THE STACK OF 1 km (LEFT) AND 2.5 km (RIGHT)

from the Keystone Generating Station (Johnson and Uthe, 1971). At 2.5 km downwind, however, the plume has diffused considerably and occasionally reaches the ground.

Very little plume-width distortion is present in this series of photographs because the vertical scans at 1 km downwind from the stack intersect the plume axis at approximately 90°, while the scan at 2.5 km downwind intersects the plume axis at an angle of about 60°.

3. Plume Trapping: Relation to Ambient Atmospheric Stratification

As was illustrated in the first frame of Figure 5, lidar returns are obtained from the ambient aerosols in the clean background air as well as from the particulates in the smoke plume. Since the upward diffusion of the ambient aerosols, as well as the plume, is controlled by the ambient thermal stratification, the lidar observations during the Homer City experiment frequently revealed features of the general meteorological regime within which the plume diffusion was taking place.

Figure 7 gives an example of plume trapping by a thermal lid at 1500 m height. The signal returns from scattered clouds at the top of and above this layer are also apparent. The composite cross sections pictured here show that plume mixing was taking place over the entire layer between the surface and 1500 m height during the two periods of 22 and 27 minutes duration.

Another example of plume trapping is presented in Figure 8. Here, the plume is seen to rise through a turbid, ambient haze layer and to be trapped, along with the ambient aerosols, by a thermally stable layer at 1500 m height. Near-neutral stability conditions within the layer covered by the rise of the plume probably existed at the time of these observations. The "hole" in the bottom of the plume caused by bifurcation is again apparent.

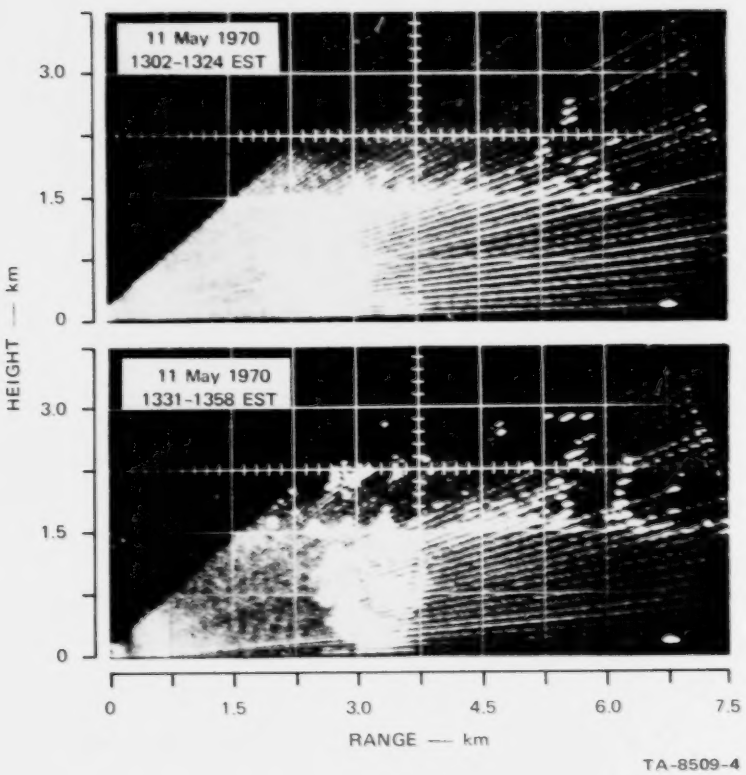

FIGURE 7 COMPOSITE CROSS SECTIONS SHOWING PLUME TRAPPING AT 1500 m HEIGHT

Each composite represents nine individual cross sections at a downwind distance of 2.5 km. Clouds are visible at and above the top of the trapped layer.

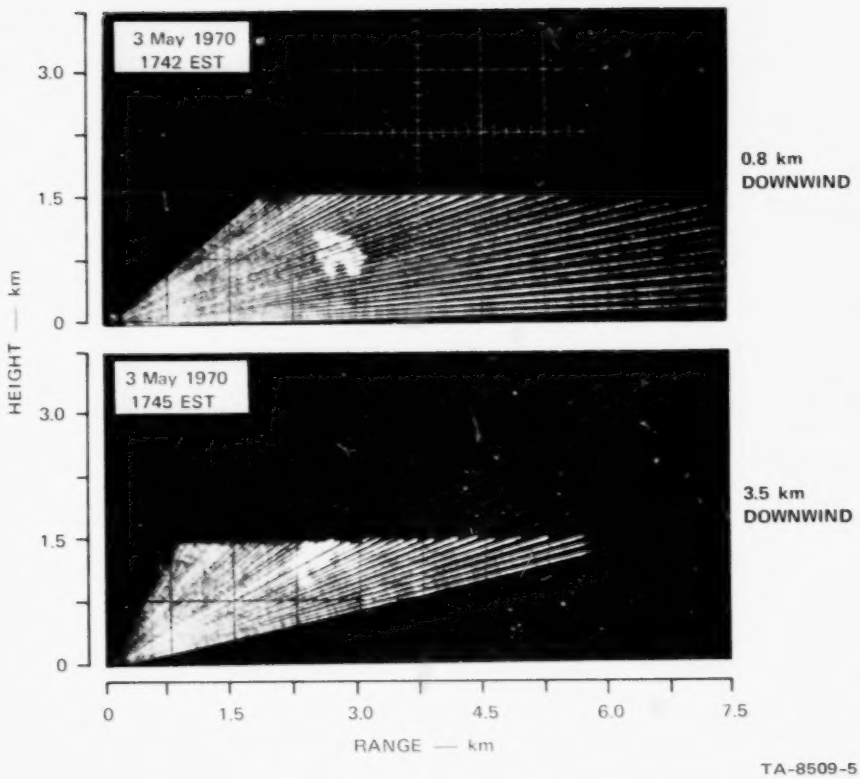

FIGURE 8 EXAMPLE OF THE TRAPPING OF A PLUME RISING IN A TURBID AMBIENT HAZE LAYER

The vertical extent of both the plume and the ambient haze is limited to 1500 m by a stable layer.

On 15 May, the plume observations showed an unusual multi-layered atmospheric haze structure, as illustrated in the time sequence of photographs in Figure 9. Up to six distinct haze layers are visible in the lower 3000 m of the atmosphere. The stack plume is embedded in the lowermost of these layers, which extends up to a well-defined top at 750 m. The tilted and elongated (but intact) shape of the plume indicates that the atmosphere within the plume layer was probably still somewhat stable, giving rise to vertical shear in the wind direction (veering). The presence of the cloud layer at 2700 m may be partly responsible for the continuation of this stability condition into the late morning hours.

4. Plume Condensation

On frequent occasions, condensation of the water vapor in the smoke plume formed visible clouds at the top of the plume. Figure 10 shows two lidar cross sections of this phenomenon that were obtained during the morning of 11 May. These scans were made in a direction approximately normal to the plume axis, at about 3 km downwind from the stack. As presented, the pictures are viewed in the downwind direction.

The helicopter temperature profile at 1036 EST indicated a lapse rate that was nearly dry adiabatic from the surface up to 950 m, with high relative humidities near the top of this layer. The lidar observations show that at 3 km downwind the plume top has already risen to an elevation of 1400 m above the lidar (1150 m above the stack top).

Thin clouds caused by condensation are clearly apparent near the bottom of the plume and along the outer boundaries of the upper portion of the plume where the plume gas has been cooled by entrainment with the surrounding air. Visual observations at this time confirmed that the cooling tower plume was not intercepting the smoke plume.

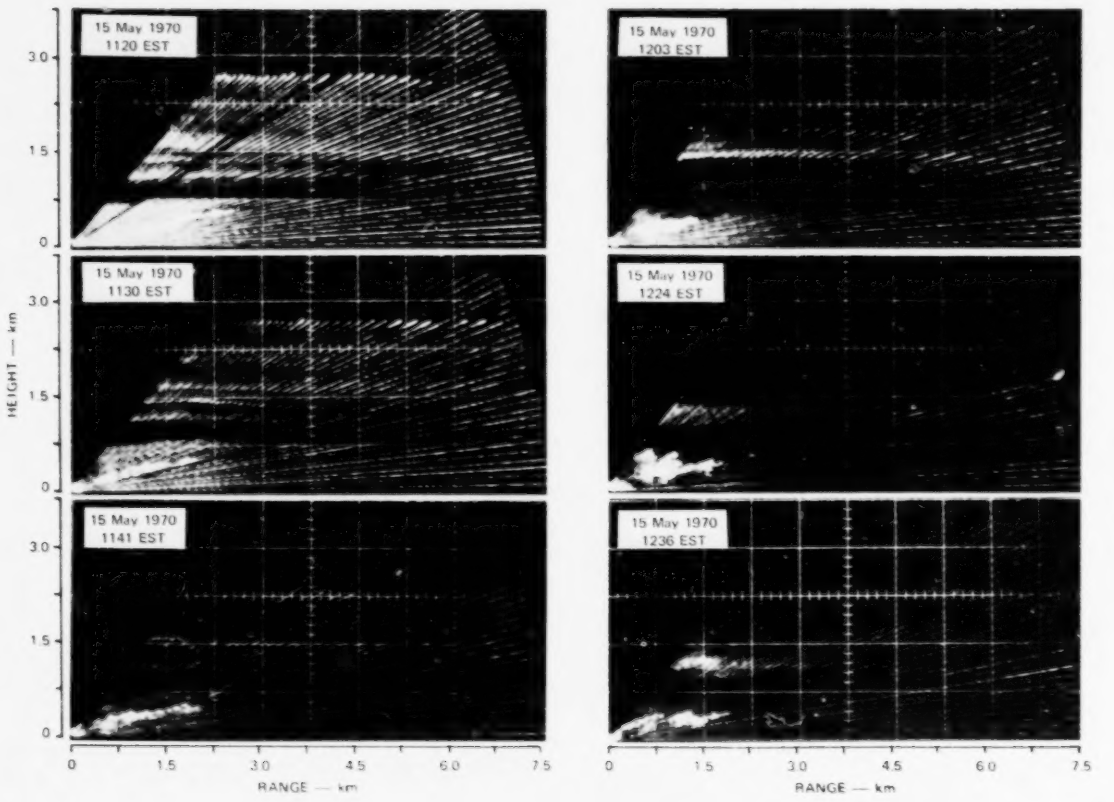

FIGURE 9 TIME EVOLUTION OF PLUME STRUCTURE AT 2.5 km DOWNWIND, WITHIN A MULTILAYERED HAZE STRUCTURE

The plume is contained in the lower layer with top at 750 m. A cloud layer is visible at 2700 m (first two photographs), and lower clouds are forming at 1300 m at 1236 EST.

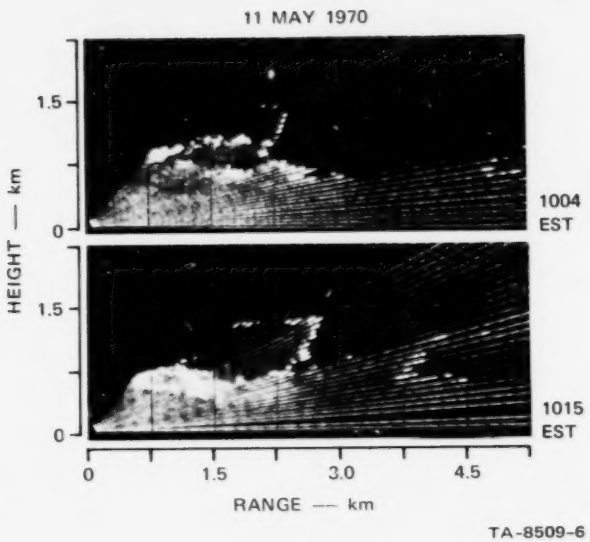

FIGURE 10 EXAMPLE OF CLOUD FORMATION WITHIN THE SMOKE PLUME 3 km DOWNWIND FROM STACK

E. Estimates of Plume Dispersion

Gifford (1971) has suggested that a "top-hat" fluctuating plume model can furnish reasonable estimates of peak-to-mean concentration ratios. This simple model is appealing in that it incorporates concepts of buoyant plume rise and assumes a uniform plume-concentration distribution that conforms reasonably well to the quasi-instantaneous distributions observed by lidar.

Gifford's model uses as a parameter the plume radius-to-dispersion ratio defined as

$$R/\sigma_y^* = (2.96 \times 10^{-5})\, Q_H^{1/3} U^{-1} x^{2/3} \sigma_y^{-1} \qquad (3.1)$$

where R = average value of instantaneous plume radius

σ_y^* = standard deviation of plume centerline location

Q_H = stack heat emission in cal sec^{-1}

U = mean wind speed

x = downwind distance

σ_y = crosswind standard deviation of the mean Gaussian concentration distribution.

Previous work (Singer and Smith, 1966) has resulted in the following well-known estimates of σ_y as a function of downwind distance (x) and atmospheric stability:

$$\sigma_y = 0.32\, x^{4/5} \quad \text{(neutral conditions).} \qquad (3.2)$$

$$\sigma_y = 0.36\, x^{13/15} \quad \text{(unstable conditions).} \qquad (3.3)$$

Using these estimates, Equation 3.1 becomes

$$R/\sigma_y^* = (0.95 \times 10^{-5})\, Q_H^{1/3} U^{-1} x^{-2/15} \qquad (3.4)$$

(neutral conditions)

$$R/\sigma_y^* = (1.03 \times 10^{-5})\, Q_H^{1/3} U^{-1} x^{-1/5} \qquad (3.5)$$

(unstable conditions)

A preliminary check of the validity of these expressions has been prepared with the aid of the lidar data from 11 May, using values of U = 6 m/sec* and $Q_H = 18 \times 10^6$ cal/sec as applicable for the afternoon period. The results of a comparison between the observed and calculated values of R/σ_y^* are given in Table 4.

As indicated in the table, the observed R/σ_y^* values for the time period 1500-1700 EST compare reasonably well with the values given by Eq. (3.4) if a near-neutral atmosphere is assumed.

However, the data for the earlier time period (1325-1458 EST) give larger values of R/σ_y^*, even though there is good reason to believe that the atmosphere was more unstable; e.g., σ_z^*/σ_y is larger than for the later period. The reason for this discrepancy is unknown, but the effect of plume trapping may be involved (see Section III-D-3). It should be noted from Eqs. (3.4) and (3.5) that small changes in U can significantly change the calculated values of R/σ_y^*. This could explain the discrepancy between calculated and observed values if the actual wind speed occurring at plume level during the period 1325-1458 EST was smaller than that estimated on the basis of the surface wind measurements.

---

*The surface winds, measured at the Jimmy Stewart Airport about 16 km north-northeast of the lidar site, were reasonably steady at approximately 6 m/sec from 215° during the period 1400-1700 EST. The upper-level wind measurement nearest to the observing time was at 1250 EST at the same airport. This sounding showed a speed of about 6 m/sec at the plume elevation (500 m above the surface), with little vertical wind shear. Hence, the best estimate for U was taken to be 6 m/sec.

Table 4

COMPARISON OF OBSERVED AND CALCULATED VALUES OF PLUME RADIUS-TO-DISPERSION RATIO (R/σ_y^*)

	Time Period--11 May 1970		
	1500-1656 EST	1503-1658 EST	1325-1458 EST
Downwind distance (m)	1000	2500	2500
Number of cases	13	13	21
Surface wind direction†	215°	215°	215°
Surface wind speed†(m/sec)	6	6	6
Plume rise (m)	175	340	240
R (m)	207	467	546
σ_R (m)	63	103	125
σ_y^* (m)	123	400	242
σ_z^* (m)	149	189	197
σ_z^*/σ_y^*	1.21	0.47	0.81
R/σ_y^* (observed)	1.68	1.17	2.25
R/σ_y^* (calculated):			
Neutral	1.46	1.28	1.28
Unstable	0.80	0.67	0.67

†As observed at Jimmy Stewart Airport, Indiana, Pennsylvania.

F. Comparison of Lidar Data with Plume SO_2 Cross Sections Observed by Helicopter

Only particulate distributions are observable by the lidar, and the question of how well the diffusion of the plume particulates reflects that of the plume gases, such as SO_2, has been of interest for some time. In an attempt to furnish additional information on this point, in this section some of the lidar plume cross sections are compared with the SO_2 cross sections obtained by plume traverses with the LAPPES-instrumented helicopter.

These comparisons are necessarily limited in number because only a small number of sets of lidar and helicopter cross sections were obtained sufficiently close together in space and time to make the comparison meaningful. Most of the helicopter observations were in the early morning, when the ground-based lidar measurements were frequently restricted by ground fog. An additional complicating factor was an occasional lack of coordination arising when communications were lost. Finally, there were a few days when one or the other observational system (lidar or helicopter) was not operating.

Nevertheless, some quasi-concurrent data were obtained, and the results regarding observed plume heights are presented in Table 5. Figures 11 and 12 show the helicopter data and some of the lidar data used in Table 5. Cases 1 and 5 (see Table 5) give reasonably comparable average plume heights (within 50 m) for both helicopter and lidar data. In Case 2, the lidar gives a considerably lower plume height than does the helicopter, while the opposite situation holds for Case 3.

These results are much too sparse to enable any conclusions to be drawn, particularly since a considerable time difference exists between some of the helicopter and lidar cross sections. Overall, however, there is a slight indication that the particulate plume heights are lower than the SO_2, which might be explained by some settling or sinking of the

Table 5

COMPARISON OF PLUME HEIGHTS (ABOVE STACK BASE) OBTAINED FROM HELICOPTER SO_2 CROSS SECTIONS AND LIDAR PARTICULATE CROSS SECTIONS

Case No.	Date (1970)	Helicopter Cross Section*					Lidar Cross Section Closest in Time				
		Time (EST)	Plume Top (m)	Plume Base (m)	Average Plume Height (m)	Downwind Distance (km)	Time (EST)	Plume Top (m)	Plume Base (m)	Average Plume Height (m)	Downwind Distance (km)
1	4 May	0559-0631	825	400	610	4	0804	700	475	580	4.5
2	9 May	0600-0610	475	275	375	4	0711	355	130	240	4.0
3	11 May	0839-0858	625	275	450	4	1001	870	320	600	3.5
4	15 May	0612-0629	500	250	375	4	--	--	--	--	--
5	15 May	0810-0837	675	225	450	4	1008	550	250	400	1.8

*The helicopter cross sections listed are those that were obtained at 4 km downwind of the stack on days when the lidar was fully operational.

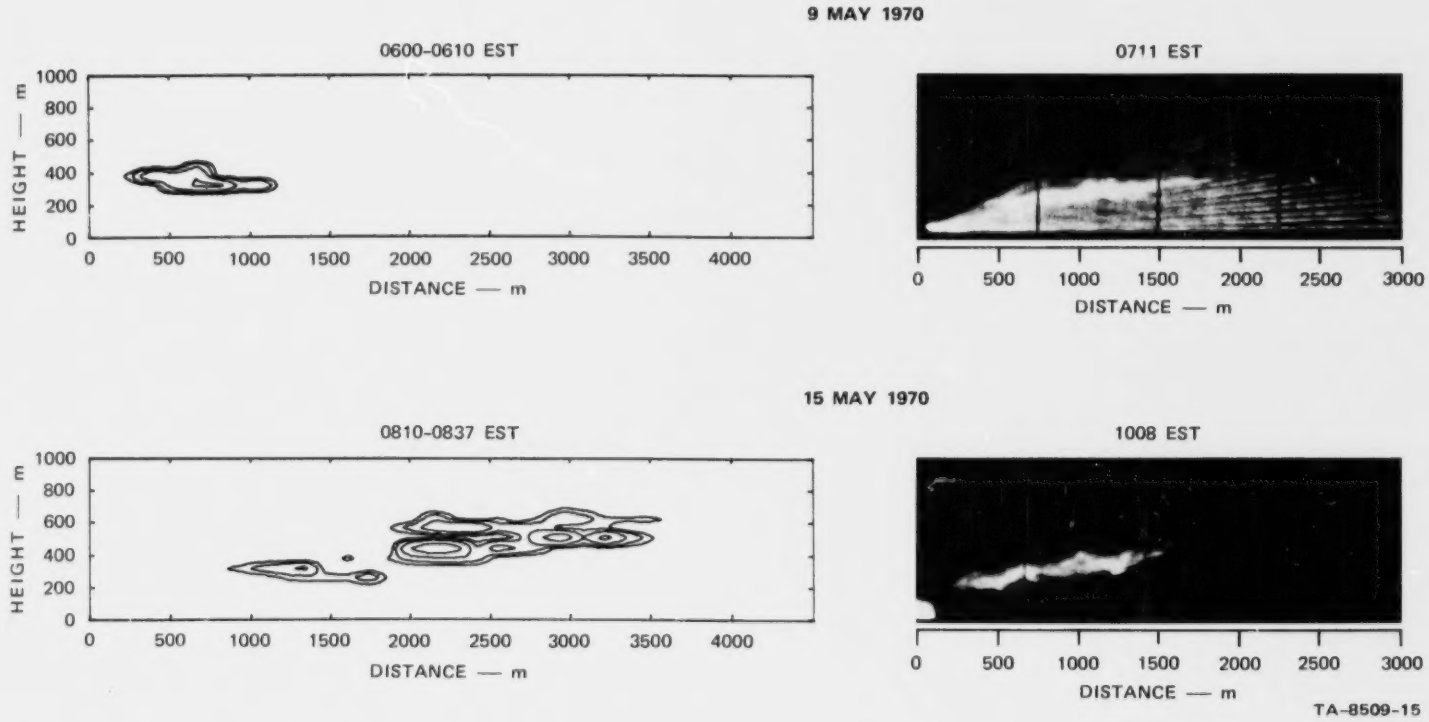

FIGURE 11 COMPARISON OF HELICOPTER SO_2-(LEFT) AND LIDAR PARTICULATE-(RIGHT) CROSS SECTIONS FOR TWO CASES DURING HOMER CITY EXPERIMENT

The SO_2 contours represent concentrations in pphm: 5, 10, 20, 40, 80, 120, 160, etc. The lidar elevation on 9 May was 20 m below the stack base elevation which was used as the reference height in the helicopter data, while on 15 May the lidar elevation was 34 m above this reference height.

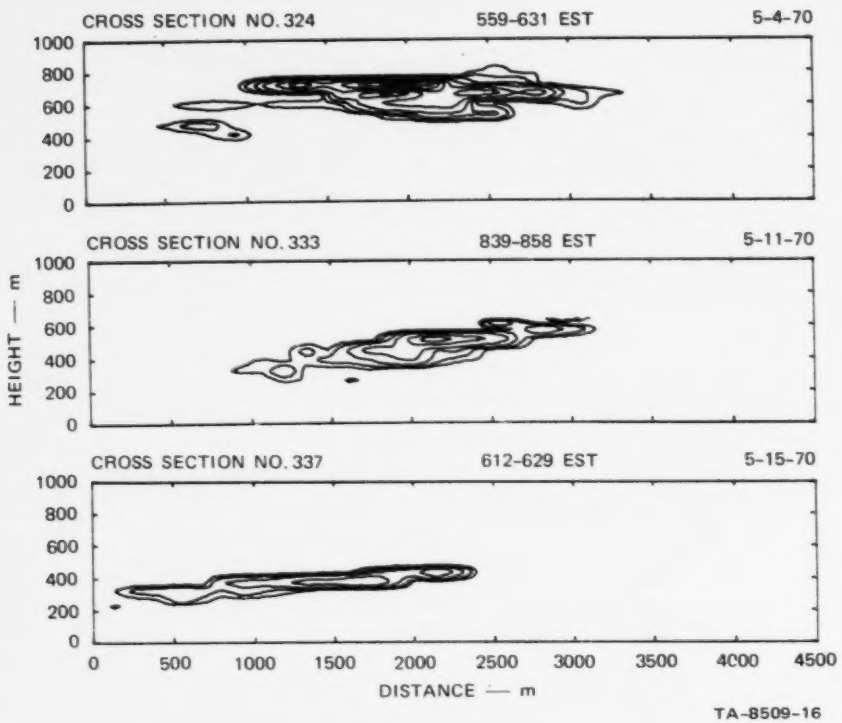

FIGURE 12 THREE OF THE HELICOPTER SO_2 CROSS SECTIONS USED FOR THE PLUME-HEIGHT COMPARISON IN TABLE III-4

The contours represent SO_2 concentrations in pphm: 5, 10, 20, 40, 80, 120, 160, etc.

particulates. Not much of the latter, would be expected, though, if the power plant precipitators are removing the large particulates as they are designed to do.

IV SAN JOSE URBAN POLLUTION-LAYER TEST

While the Mark VIII system was being prepared for the urban pollution-layer observations in St. Louis, mobile and stationary tests were conducted in the Menlo Park area and along local freeways. The results of several of these special tests are presented for general interest in Figure 13. These height/distance and height/time cross sections were among the first such observations obtained by the newly modified Mark VIII lidar system.

At about this same time, another field project concerned with the evaluation of an urban diffusion model* was being conducted in nearby San Jose (15 miles southeast of Menlo Park). Since this latter experiment included the measurement of carbon monoxide (CO) and air temperature profiles over San Jose by means of an instrumented helicopter, it seemed worthwhile as part of the lidar system checkout to conduct a brief series of comparative measurements.

On several days during December 1970, the Mark VIII was situated in the vicinity of Spartan Stadium near central San Jose and operated in the vertically pointing stationary mode. Figure 14 presents a time series of time/height cross sections obtained by lidar observations spaced 12 seconds apart throughout most of one day.† Concurrent temperature and CO profiles obtained by the helicopter are given in the lower right portion of the figure.

---

*Jointly sponsored by the Coordinating Research Council and by the EPA.

†Some minor technical problems occurred during this series. The horizontal wavy lines at low heights and the occasional vertical white bands on the photographs were caused by electronic ringing and intermittent noise. However, these do not affect the general validity of the data.

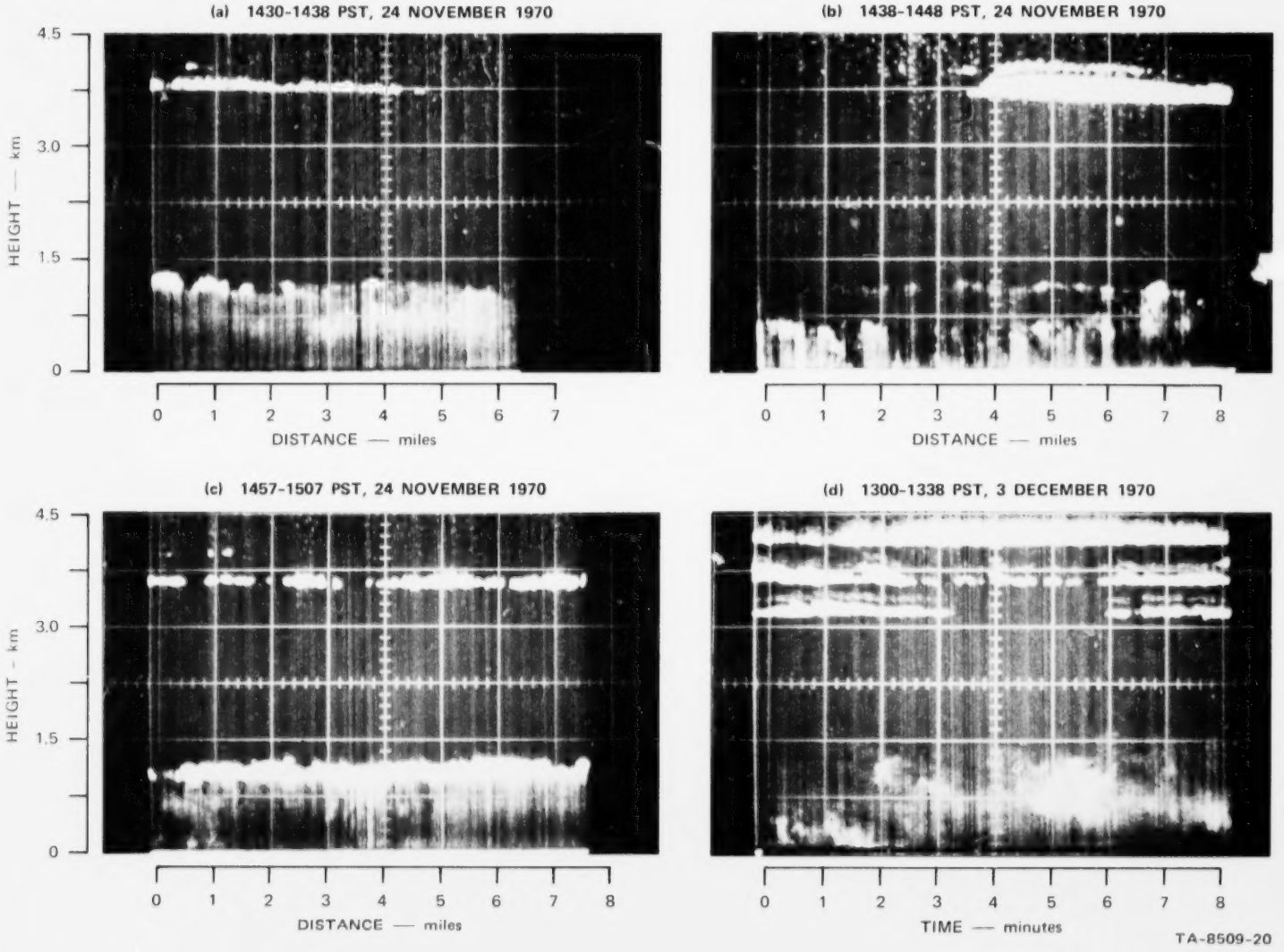

FIGURE 13 HEIGHT/DISTANCE (PHOTOS A, B, AND C) AND HEIGHT/TIME (PHOTO D) CROSS SECTIONS OBTAINED DURING SPECIAL TESTS OF THE MODIFIED MARK VIII LIDAR SYSTEM IN THE MENLO PARK, CALIFORNIA AREA

Cloud layers (brightest areas) are apparent at the top of the lower haze layer and at higher levels.

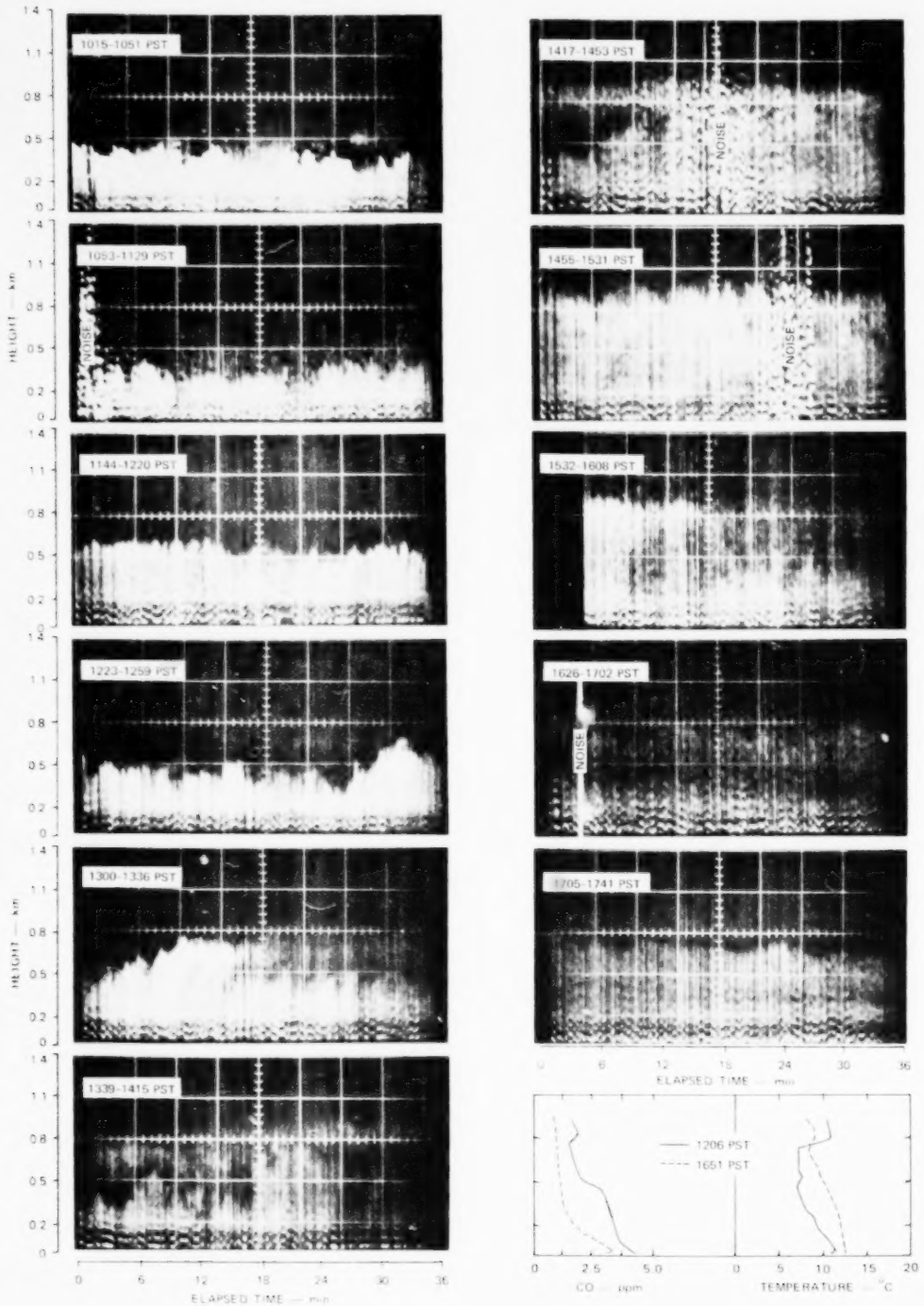

TA-8509-13

FIGURE 14 LIDAR-OBSERVED TIME/HEIGHT CROSS SECTIONS OF THE URBAN HAZE LAYER OVER SAN JOSE, CALIFORNIA, ON 11 DECEMBER 1970

Concurrent helicopter profiles of carbon monoxide (CO) and air temperature are shown at the bottom right.

The noon helicopter sounding shows temperature inversions at two levels, approximately 450 m and 750 m above the surface, while the late afternoon sounding indicates that the lower inversion has dissipated. The lidar data reveal a haze layer persisting during the morning hours, with the haze top varying between 400 and 600 m. (Scattered clouds initially present at 400 m height have dissipated by 1045 PST.) During the period from about 1250 to 1320 PST, the lower inversion is apparently penetrated by an aerosol-laden air mass, which in turn is trapped by the upper inversion at 750 m. The lower haze layer immediately becomes reestablished but expands at about 1425 PST to become a rather uniformly mixed layer up to a height of about 900 m. By the time of the 1651 PST helicopter sounding, the top of this layer corresponds closely to the 750-m height of the temperature-inversion base. This rather close correspondence indicates that the lidar-observed aerosol layers are indeed reflecting true mixing heights. In addition, the rapid variation in these heights clearly illustrates the potential lack of representativeness of a single temperature sounding.

The helicopter profiles of temperature and CO concentration have been used to estimate the depth of the San Jose urban mixing layer for the period 7, 9, 10, and 11 December 1970. In Table 6, these estimates are compared with values obtained from the haze tops observed by the Mark VIII lidar. As indicated in Table 6, the overall agreement in mixing depths obtained by the two methods is reasonably good.

The helicopter and lidar data often indicate the presence of multiple stable layers in the lowest 1000 m above the surface. The CO profiles on these occasions show some penetration of CO through the near-surface mixing layer. This occurs when the lid is not particularly strong (as indicated by the temperature profile), but the concurrent lidar observations frequently indicate intermittancy in the occurrence height of the lid. This intermittancy may be the result of local (convective) or advective effects and seems to represent a transitional stage in the lower atmospheric structure.

Table 6

COMPARISON OF LIDAR-OBSERVED HAZE-LAYER TOPS OVER SAN JOSE, CALIFORNIA, WITH MIXING-DEPTH ESTIMATES FROM HELICOPTER PROFILE DATA

Date	Time (PST)	Mixing Depths (m) Derived from Helicopter Data	Lidar-Observed Haze-Layer Tops* (m)
7 December	1240	215	450, 850†
9 December	0800	100	300-500 (variable)
	1200	125, 675†	450-600 (variable)
	1700	200, 725	750
10 December	0800	125	300
	1200	425	450‡
	1700	500, 750	250
11 December	0800	60, 550	Low Clouds
	1200	500, 725	350-700 (variable)
	1700	600	600-750 (variable)

*Indicating the height variation over a one-half hour period.

†Multiple values for the helicopter and lidar data represent the tops of the surface and elevated mixing layers.

‡Lidar observation made at 1430 PST.

Source: Johnson et al. (1971).

V ST. LOUIS URBAN POLLUTION-LAYER EXPERIMENT

A. Objectives

This experiment was basically a feasibility test of the usefulness of lidar in urban areas with regard to air pollution applications. To the best of our knowledge, it constituted the first field trial of a truly ground-mobile lidar system*--one that could take observations from a vehicle while in motion. (Previous lidar systems had been only portable or transportable and were thus capable of taking observations only in the fixed mode.)

The reason for developing the mobile system was to permit observations of the spatial, as well as the temporal, distribution of particulates in urban pollution layers. As described by Clarke (1969) and a number of other investigators, the structure of the pollution layer over and downwind of cities, as determined by the relevant geophysical and meteorological variables, is a central concern in air pollution meteorology. The nocturnal urban mixing layer and the diffusion of any pollutant plumes released within it depend significantly on the urban heat output, urban roughness, ambient thermal stratification, wind speed, and long-wave radiational processes.

A truly comprehensive study of the modification of the lower atmosphere as the air moves over a city would require measurement or estimates of all of these variables. This first urban lidar experiment was a brief and rather modest effort that was mainly concerned with determining the capabilities of

---

*As of that date, three air-mobile lidar experiments using fixed-wing aircraft had previously been conducted by SRI.

Preceding page blank

lidar in this context, so that its future role in later studies entailing a greater variety of types of measurements could be better defined. Thus, the objectives of the study were limited to obtaining spatial distributions of mixing depths over and downwind of St. Louis, by means of lidar observations in a moving frame of the vertical particulate-layer structure over the city.

B. Experimental Techniques

The system was prepared for the experiment by installing the Mark VIII lidar in a specially modified van with a 16-ft box-type body. Two 5-kW motor-generator sets (operated from the van fuel system) were installed in the front portion of the van to provide electrical power to the lidar while the van was in motion. This area was partitioned off from the lidar section and suitably vented to minimize noise and fumes in the lidar operating area. A hatchway was installed in the roof of the van to permit vertical observations by the lidar. (Additional elongated trap doors were also installed in the roof to permit elevation scanning while stationary.) A special modification was made to the van odometer so that it could control the lidar firing rate. In this way, lidar observations could be taken at uniform increments of distance, regardless of the speed of the van. Provision was made for operator selection of a firing density of either 10 shots/mile or 20 shots/mile. An intercom was installed to permit communication between the driver of the van and the lidar operator.

During the experiment, the van was driven over street routes in and around St. Louis while lidar measurements were taken. The route followed at any particular time was selected to give spatial coverage appropriate to the wind direction prevailing at that time. Generally the maximum shot density, 20 shots/mile, was used. The lidar data were cross-referenced to spatial location by means of a written log in which specific road checkpoints, disk recorder track numbers, and times were recorded. Each disk

recorder track covered 160 lidar observations, or a route distance of 8 miles. Sometimes fewer shots/track were recorded to permit ending a track at a convenient checkpoint.

The routes covered and the checkpoints used are indicated in the St. Louis map depicted in Figure 15.

C. Data Summary

A general summary of the data collected during the experiment, along with the prevailing weather conditions, is given in Table 7. A more detailed summary of the individual runs, or route segments, is presented in Appendix C.

D. Results

As indicated in Table 7, the wind speeds encountered during the observational period were rather consistently moderate to strong, as would normally be expected in St. Louis in March. This prevented any significant pollution-layer buildup during the observational period. The strength of the return signal from this quite clean air was frequently too weak to permit delineation of the pollution-layer structure.

In addition, a number of equipment malfunctions occurred that resulted mainly from the low air temperatures and the rather severe road shock to which the optical components and electronic modules were exposed. These conditions had been anticipated, and heaters and heavy-duty shock mounts had been installed and tested, but these precautions unfortunately proved to be insufficient. Consequently, much of the resultant data contain excessive electronic noise.

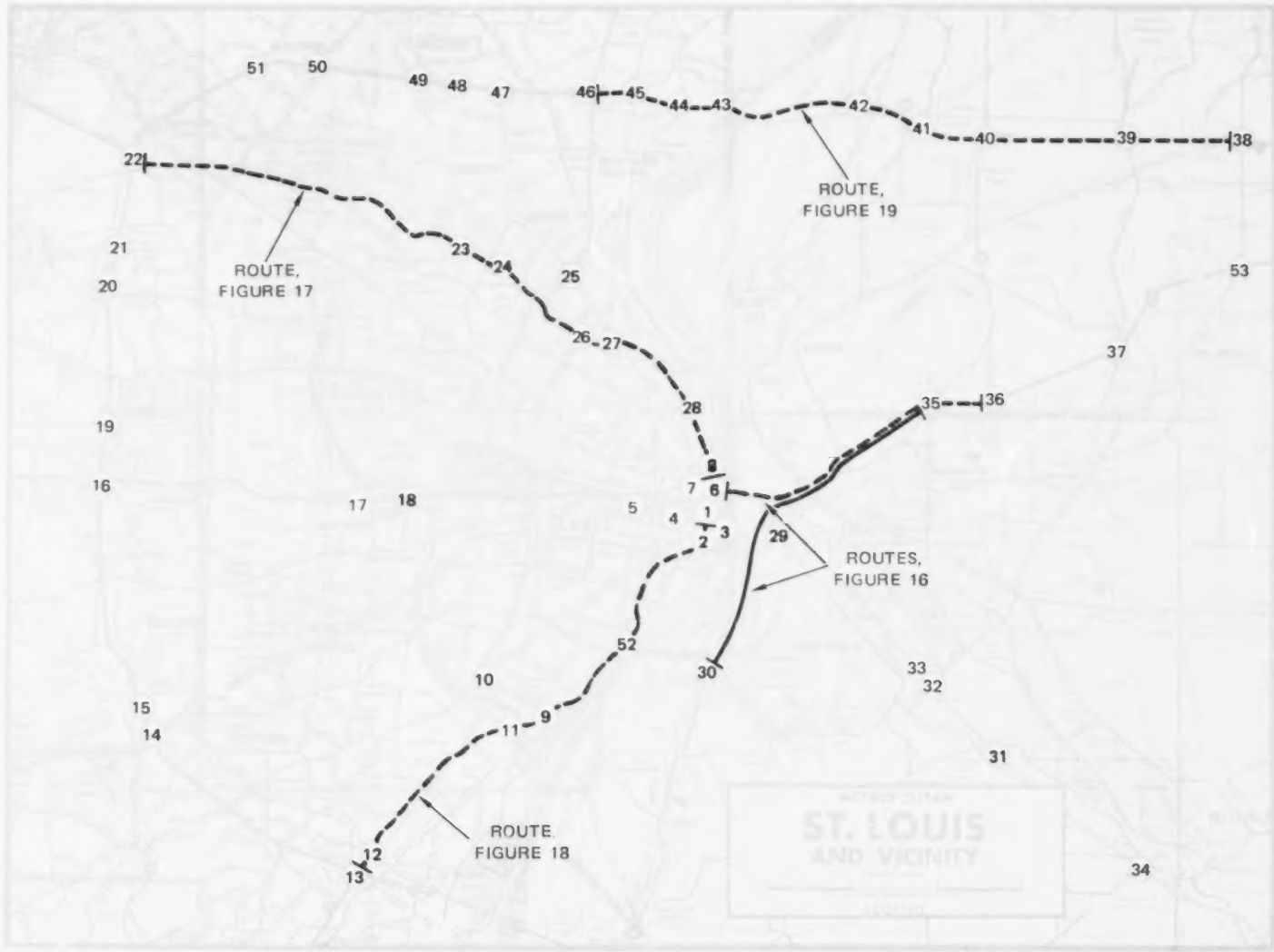

TA-8509-11R

FIGURE 15 ST. LOUIS LIDAR ROUTE AND CHECKPOINTS

Table 7

DATA SUMMARY: ST. LOUIS LIDAR EXPERIMENT
1971

Date	Period (CST)	Run Numbers	Number of Runs	Weather
1 March (Mon.)	0938-1148	32-54	12	○10 060°/15-20 32°
	1315-1525	56-78	12	80◑150◑10 060°/10
	1623-1627	80	1	90◑/⊕10 060°/10 50°
2 March (Tues.)	0820-1153	82-112	16	150⊕7 360/10-15 31°
	1252-1612	114-144	16	150⊕10 360°/15
4 March (Thurs.)	0450-0850	146-176	16	○10 270°/5 22°
	1002-1247	178-200	12	/◑7H 220°/5 36°
	1355-1405	202	1	○10 200°/5-10 45°
5 March (Fri.)	0437-0730	204-232	15	/◑10 180°/5 34°
	0759-1013	234-246	7	○10 200°/10
7 March (Sun.)	0424-0649	248-270	12	30◑10 270/15 31°
8 March (Mon.)	0638-1041	272-302	16	○15 300°/5 25°
	1219-1253	304*	1	○15 320°/10-15
9 March (Tues.)	0431-0826	306-336	16	100◑/◑10 130°/5 30°
	0859-1228	338-370	17	80⊕10 130°/10
			170	

*Stationary run with van parked near the National Weather Service Environmental Meteorological Support Unit (EMSU) balloon release site; all other runs are mobile.

It should also be noted at this point that an electronic problem in the video disk recorder during the St. Louis experiment prevented the collection of valid data within the first 150 m from the lidar. Thus, only data above 150-m height are shown in the figures in this section. This, of course, is unfortunate because of the important meteorological processes and associated structure that often occur below this height within the nocturnal urban boundary layer.

The net result of these weather and equipment problems was that, out of the rather large amount of data collected, only a small amount turned out to be both of meteorological interest and sufficiently free of technical difficulties to be useful. Thus this first St. Louis lidar field study can be considered as only partly successful. The potential of lidar for studying urban air pollution was successfully demonstrated, but insufficient valid data were collected under conditions of interest to permit any definitive conclusions to be reached regarding the structure and behavior of the urban mixing layer.

In this section, we present and briefly discuss examples of the St. Louis lidar data. The purpose of this is not to shed any revelations about the air pollution meteorology of the St. Louis area, since the data are not sufficient for that, but rather to illustrate the nature of the capabilities of a mobile lidar for use in future studies of urban air pollution.

The fundamental advantage of the mobile lidar as an observational tool rests in its ability to obtain spatial as well as temporal distributions of aerosol-layer structure. This is well illustrated by Figure 16, which shows the time evolution--from early morning to mid-morning--of the vertical aerosol distribution over two approximately nine-mile routes through East St. Louis on 4 March 1971. The portions of each cross section marked

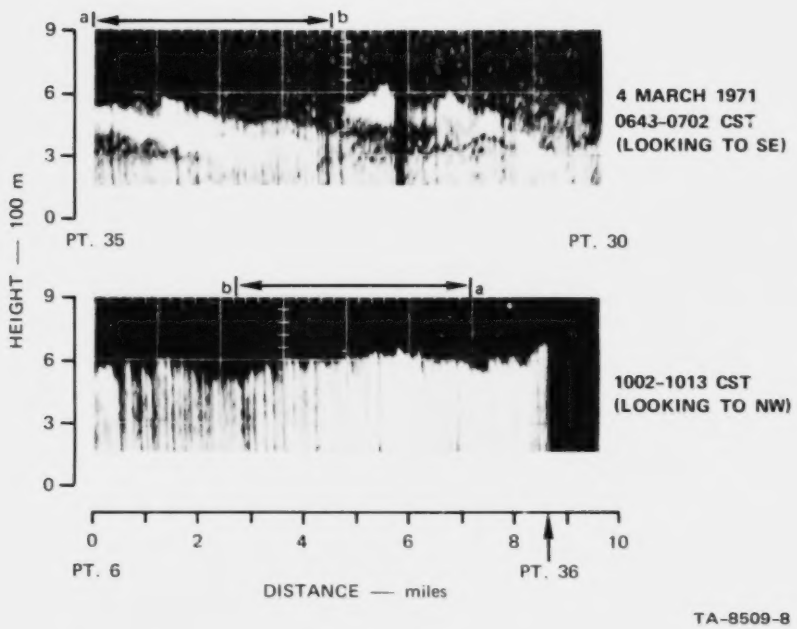

FIGURE 16 TIME CHANGES IN POLLUTION-LAYER STRUCTURE APPROXIMATELY ALONG WIND THROUGH EAST ST. LOUIS

"a-b" are over a common route segment (see Figure 15) but are separated in time by about three hours.

The early morning observations (top picture in Figure 16) indicate a rather uniform aerosol layer topping at about 300 m, overlaid by several plumes from industrial sources. The buoyancy of these plumes has apparently permitted them to penetrate into the stable air above the lower well-mixed layer. At the time the sky was clear, with an estimated surface wind from 240° at 5 knots.

The mid-morning cross section (bottom picture in Figure 16) shows that convective mixing has become dominant and has created a relatively uniform aerosol layer extending to a height of about 600 m. This was also the height of the tops of the plumes observed earlier and thus is probably the height of the base of a general, ambient, elevated inversion layer. The meteorological conditions at this time were much the same as earlier. The surface winds were from 220° at 5 knots.

A 16-mile cross section from extreme northwestern to central St. Louis is presented in Figure 17. This route lies approximately crosswind to the surface wind at that time, which was from 240° at 5 knots (see Figure 15). The main feature of interest in Figure 17 is the change in the height of the aerosol layer from about 250 m over northwestern St. Louis to about 500 m over central St. Louis. These observations contain considerable electronic noise, but the shape of the pollution layer is reasonably well-defined. Variations on the order of 100 m are apparent in the top of the mixed layer near central St. Louis.

Figure 18 shows a similar vertical cross section, except it extends from central St. Louis to the extreme south-southwestern edge of the city during the early afternoon on 1 March 1971 (see Figure 15). The surface winds were from 060° at about 10 knots. Thus, the route represented in

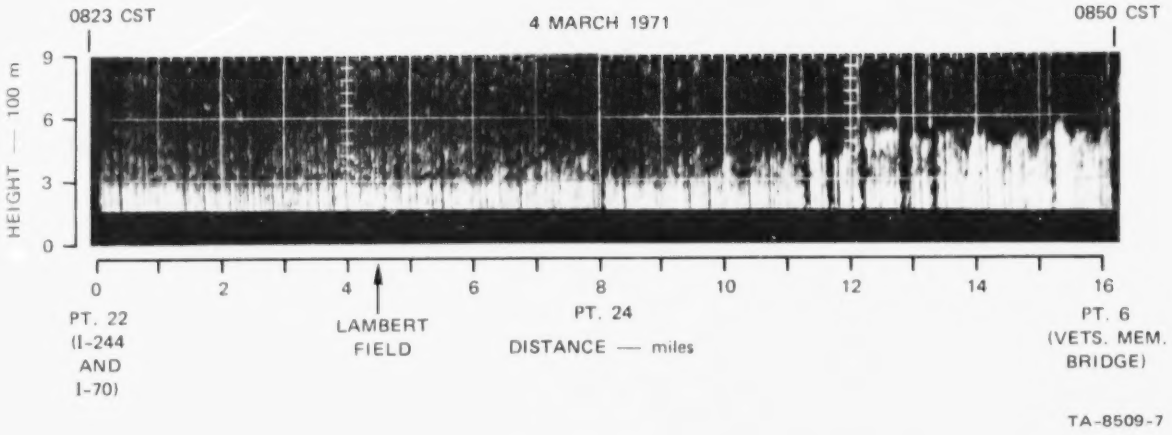

FIGURE 17 VERTICAL POLLUTION-LAYER STRUCTURE IN AN APPROXIMATELY CROSSWIND DIRECTION ALONG I-70 IN ST. LOUIS (LOOKING TO NORTHEAST)

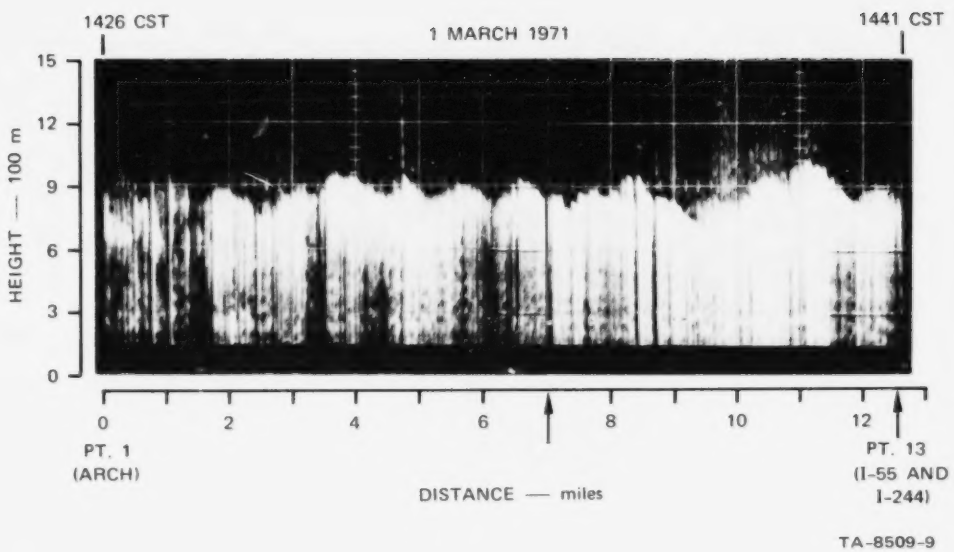

FIGURE 18 VERTICAL POLLUTION-LAYER STRUCTURE IN THE DOWNWIND DIRECTION ALONG I-55 FROM THE ARCH IN CENTRAL ST. LOUIS (LOOKING TO SOUTHEAST)

Figure 18 lies approximately in a downwind direction from central St. Louis. In this connection, it is interesting to note the slightly higher top and the greatly enhanced density of the pollution layer as it moves downwind from the central part of the city. This can be readily explained on the basis of the additional pollutants that would be added to the mixing layer from the many sources to the southwest, and thus downwind, from the arch in central St. Louis.

During the field program, attempts were made to measure the structure of the overall urban pollution plume or layer as it moves downwind from St. Louis. Figure 19 depicts a series of cross sections obtained approximately 10 miles downwind of central St. Louis near noon on 4 March 1971. The route followed is in a west-east direction (see Figure 15). Since the surface wind during this period was from 180° to 220° at 5 to 10 knots, the lidar route is approximately in a crosswind direction. As shown in Figure 19, during this mid-day period the mixing layer was apparently well developed, having a top at an average height of 700 m, with height variations of ±200 m. The shift in the urban-pollution plume position during the period indicates that the winds were becoming more westerly with time.

The plume width is difficult to judge but appears to be about 6 to 8 miles, except for the middle cross section where it is apparently somewhat wider. This 6-to-8-mile plume width seems to be reasonable, since this would encompass most of the heavily industrialized areas near the Mississippi River in St. Louis and East St. Louis.

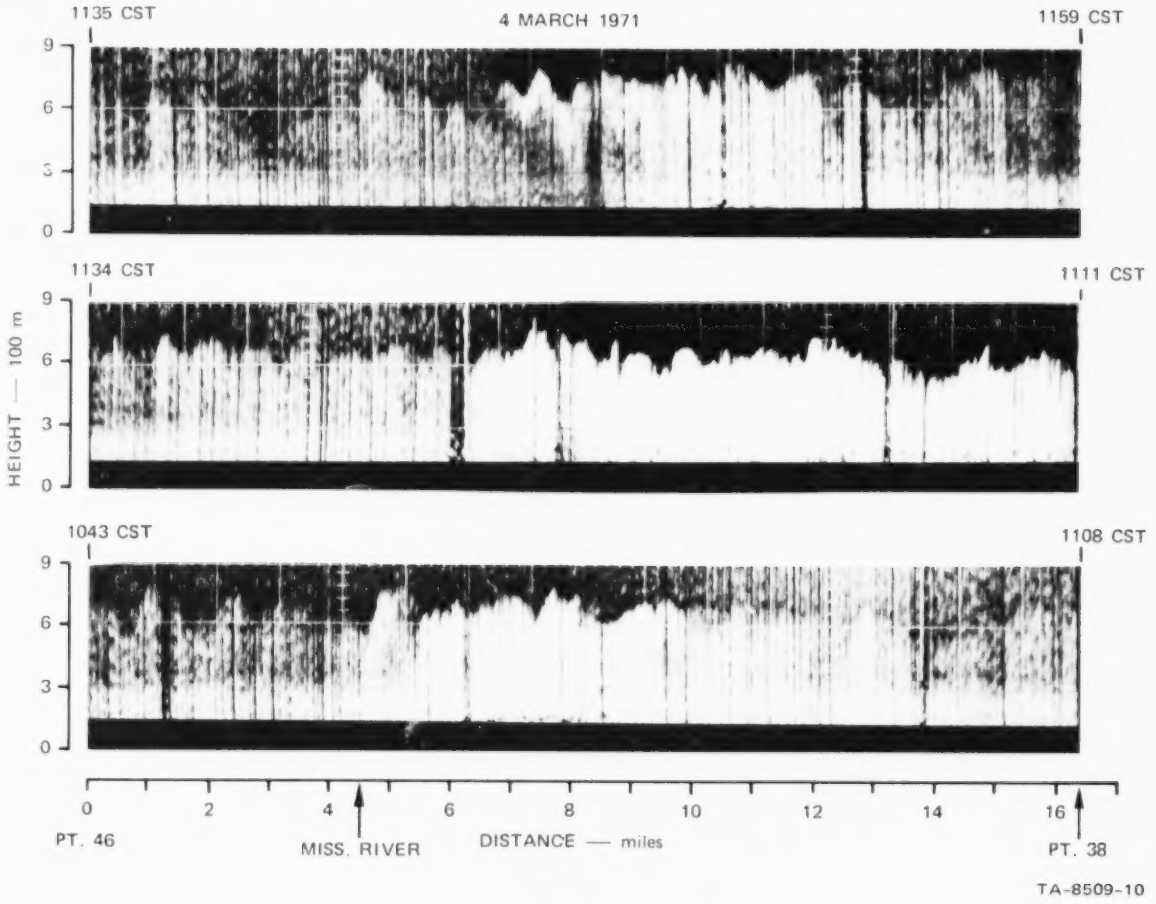

FIGURE 19 VERTICAL POLLUTION-LAYER STRUCTURE IN A WEST-EAST DIRECTION ALONG I-270 DOWNWIND OF CENTRAL ST. LOUIS (LOOKING TO NORTH)

VI RELEVANT SUBSEQUENT LIDAR APPLICATIONS

As previously mentioned, when the Mark VIII lidar system was applied in the three experiments sponsored under this contract, it was in each case the first test of the newly fabricated system in a particular operational mode or configuration. On the basis of these tests, the system was rapidly refined, resulting in significantly improved data quality for later experiments. In this section, we briefly present samples of some recent results from subsequent field studies to illustrate the current capabilities of the system.*

A. Diurnal Variation of the St. Louis Mixing Layer (NSF/SRI METROMEX Projects)

Figure 20 presents a height/time cross section of aerosol structure recorded over central St. Louis, obtained with the Mark VIII lidar (Uthe, 1972).† This figure shows the urban pollutants trapped within the stable air near the earth's surface. Clouds and haze are visible aloft and thus hinder the passage of the solar energy to the surface. The figure also shows that beginning about noon, a rapid deepening of the polluted layer--apparently caused by vertical air motions resulting from surface heating--effectively dilutes the urban pollutants. The convective cloud formation observed by the lidar during the afternoon could be related to precipitation anomalies that have been observed downwind of urban areas.

---

*These studies were not supported by this contract.

†Study sponsored by the National Science Foundation.

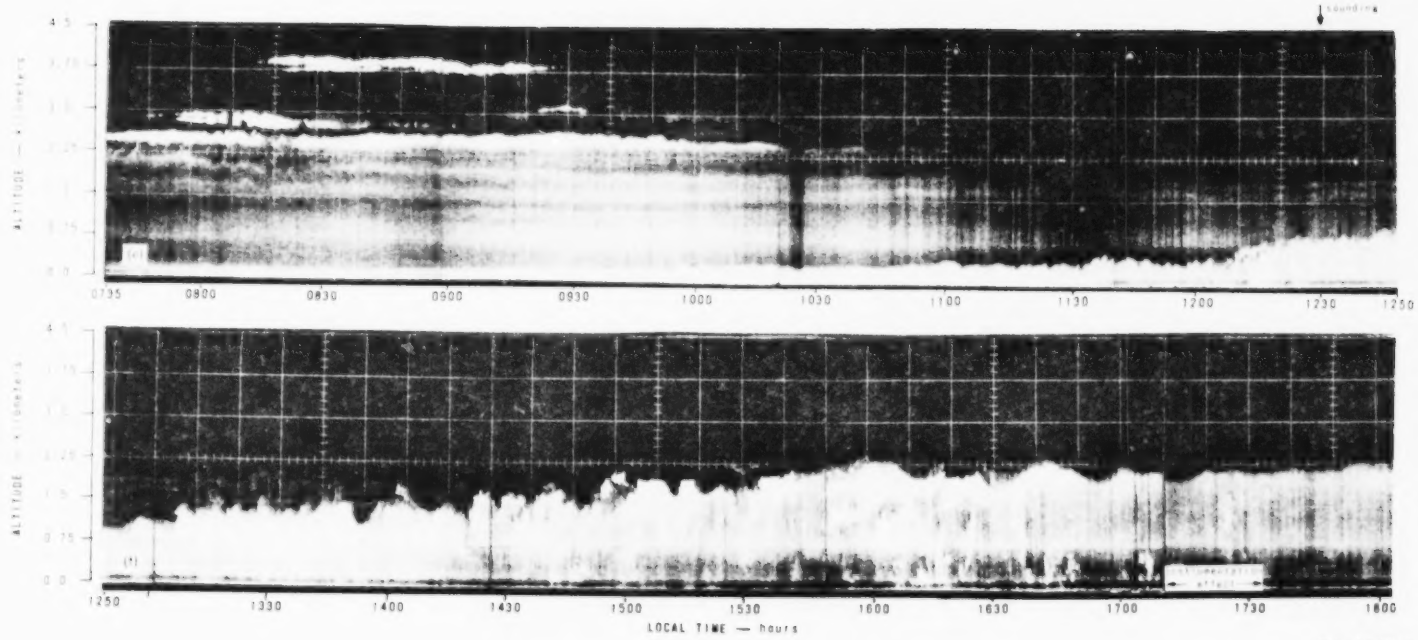

TA-1445-1

FIGURE 20 HEIGHT/TIME CROSS SECTION OF THE AEROSOL STRUCTURE OVER ST. LOUIS ON 13 AUGUST 1971 AS OBSERVED BY SRI/EPA MARK VIII LIDAR SYSTEM

B. Spatial and Temporal Variations of the Los Angeles Mixing Layer (EPA Project)

Figures 21 and 22 are examples of the results obtained with the Mark VIII mobile lidar system in a field study of mixing heights over the Los Angeles Basin in September 1972.* The 70-mile triangularly shaped freeway route over which the lidar observations were made is shown in Figure 23.

Of particular interest in Figure 21 is the rapid and substantial change in the structure of the mixing layer on the east side of the Basin as the marine air penetrates eastward during the afternoon. An upper aerosol layer is apparent near Azusa at 1550 PDT, possibly the result of vertical air currents along the heated south-facing slopes of the San Gabriel Mountains. A wind reversal from WSW winds at the surface to NE winds at 1000 m elevation was observed by the El Monte EMSU station at about this time. This vertical wind shear could have caused the waves apparent on the aerosol layers.

Noteworthy features of the mixing-height spatiotemporal pattern in Figure 22 include the enhanced vertical extent of the mixing layer near South El Monte at 1300 PDT and the eastward propagation of the marine layer (sea breeze) along Legs 2 and 3 between 1200 and 1400 PDT, as indicated by the large contour gradient of mixing height. In addition, larger mixing heights are observed over downtown Los Angeles at 1100 PDT--probably because of urban effects--and also in the Long Beach area at 1200 PDT, apparently because of vertical motions resulting from horizontal convergence of the air on the leeward side of the Palos Verdes Hills. This Palos Verdes Convergence Zone is a typical feature of the sea-breeze circulation in the Los Angeles Basin.

---

*Study conducted by W. B. Johnson, T. J. Lemmons, L. A. Knight, and R. E. Chalfant of the Meteorology Laboratory, EPA.

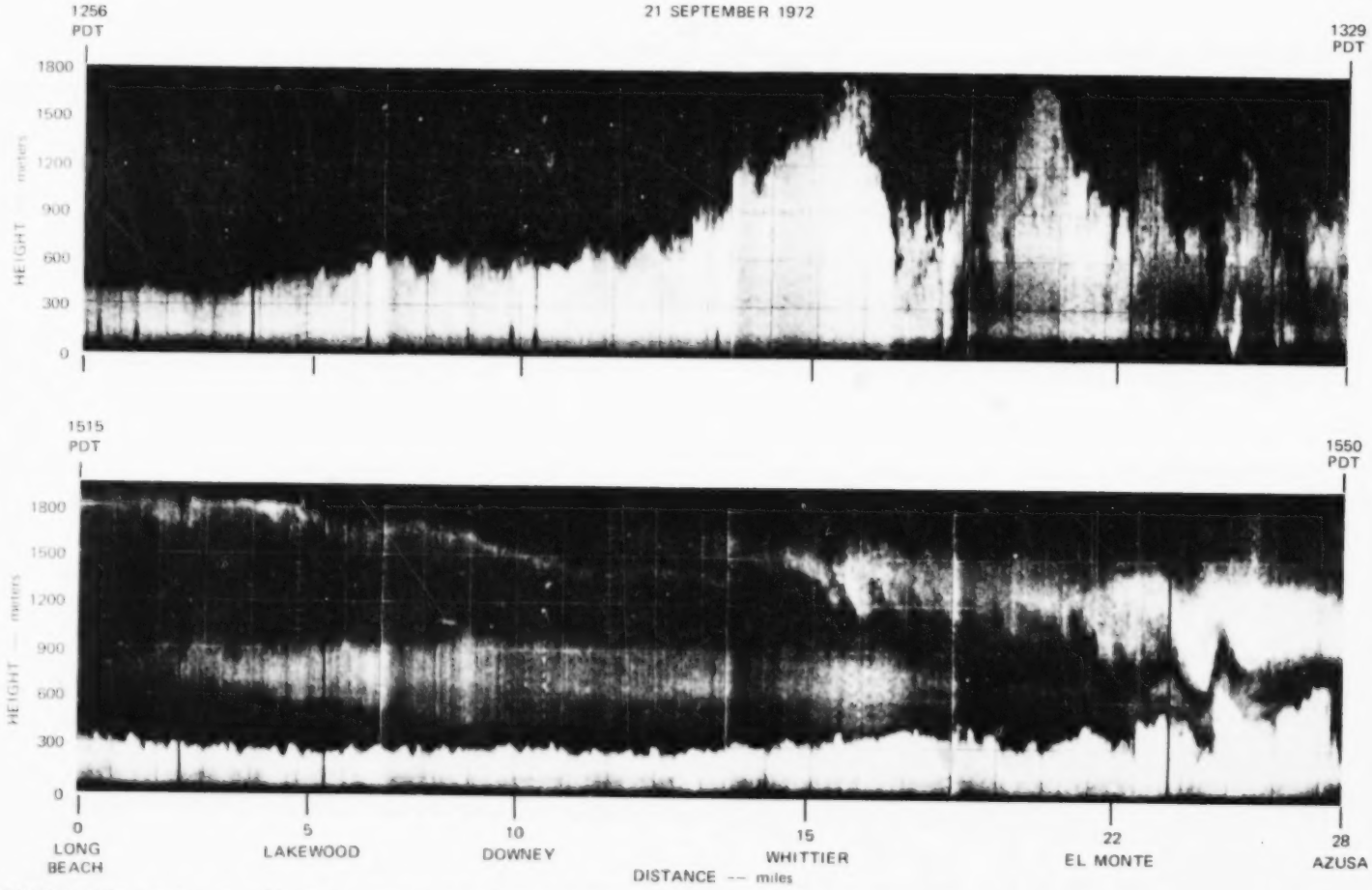

SOURCE: From a study conducted by W. B. Johnson, T. J. Lemmons, L. A. Knight, and R. E. Chalfant of the Meteorology Laboratory, E.P.A.

TA-653583-74

FIGURE 21 TIME EVOLUTION OF THE LOS ANGELES AEROSOL (SMOG) LAYER AS OBSERVED DURING AN EARLY AFTERNOON PERIOD BY THE MARK VIII LIDAR OVER A SOUTH-NORTH ROUTE ON THE EAST SIDE OF THE BASIN (On Highway I-605 between I-405 and I-210)

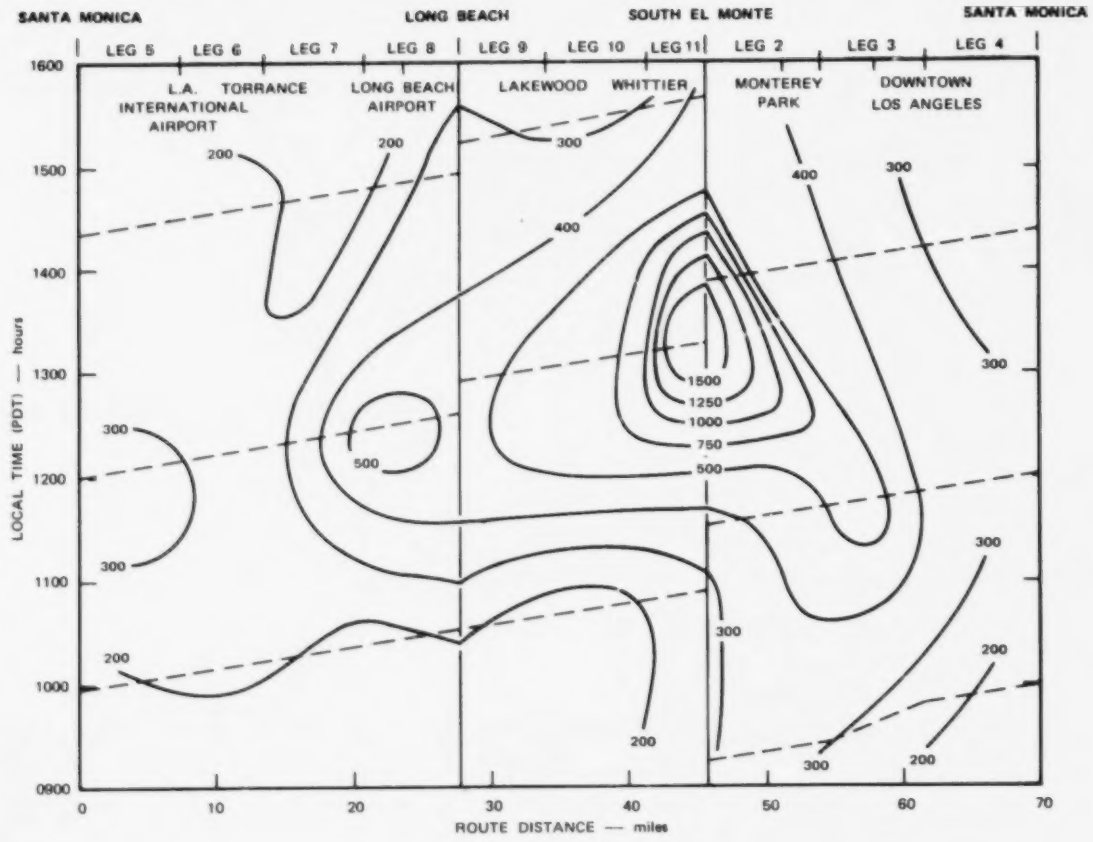

SOURCE: From a study conducted by W. B. Johnson, T. J. Lemmons, L. A. Knight, and R. E. Chalfant of the Meteorology Laboratory, EPA.

TA-653883-75

FIGURE 22 LOCATION-TIME CONTOURS OF LIDAR-OBSERVED AEROSOL MIXING HEIGHT (IN METERS) ALONG A 70-MILE FREEWAY LOOP OVER THE LOS ANGELES BASIN ON 21 SEPTEMBER 1972

The dashed lines indicate where and when the observations were made. The triangular route is illustrated in the accompanying figure.

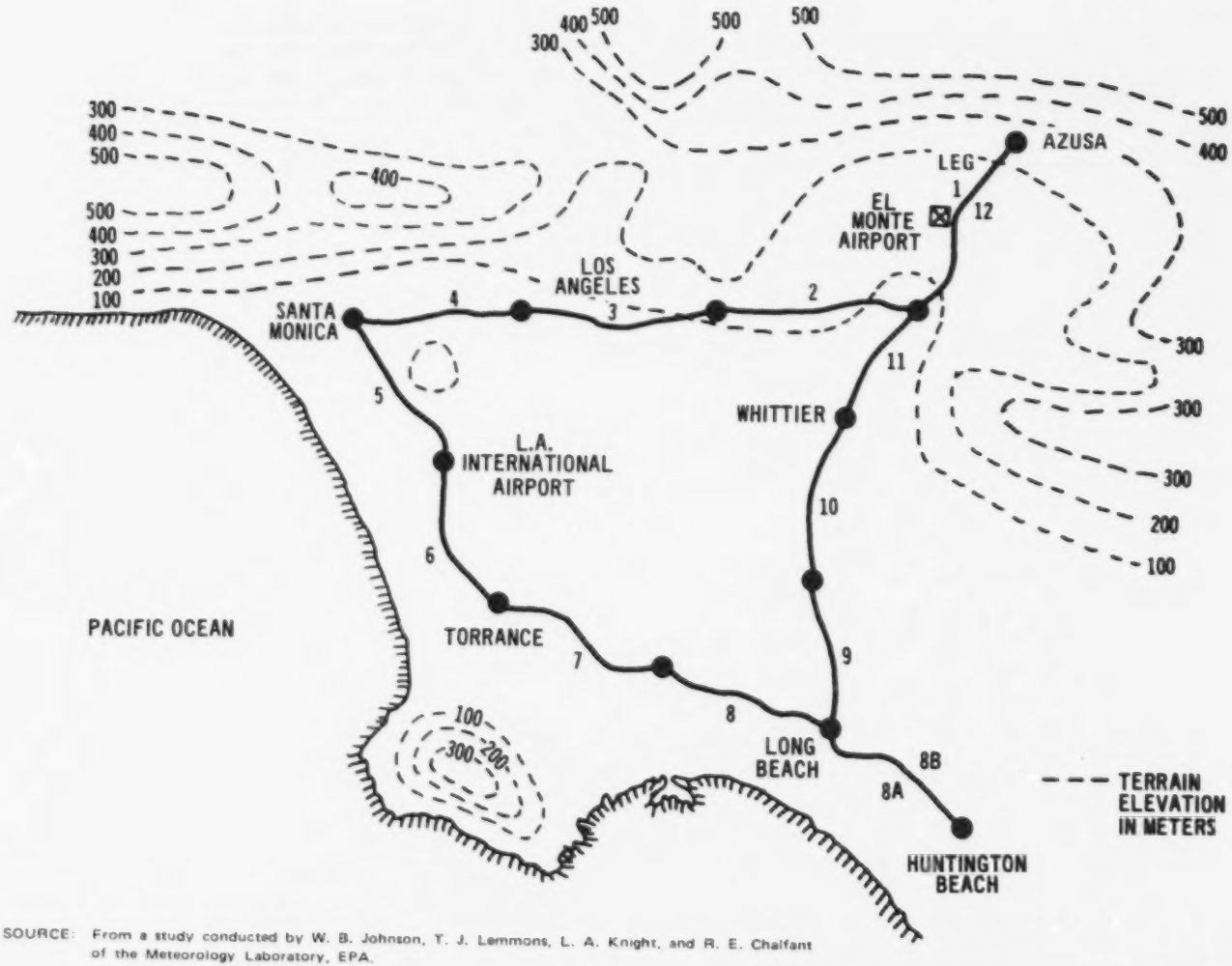

SOURCE: From a study conducted by W. B. Johnson, T. J. Lemmons, L. A. Knight, and R. E. Chalfant of the Meteorology Laboratory, EPA.

TA-653583-76

FIGURE 23 MOBILE LIDAR ROUTES, LOS ANGELES BASIN, SEPTEMBER 1972

VII CONCLUDING REMARKS

This project entailed the development and application of a sophisticated and unique atmospheric remote-probing system incorporating state-of-the-art electronic and optical technology. The technical problems that inevitably accompany the field testing of complex new systems of this nature were not completely avoided, but in every case these problems were overcome. The overall results of the field programs appear to confirm the usefulness of lidar systems of this type for air pollution and meteorological studies.

Perhaps the most significant feature of the Mark VIII system is its capability for analog processing and display of the data in real-time. This permits the inherent high data-rate advantage of the lidar technique to be exploited and largely eliminates the need for costly and time-consuming post-experiment data analysis.

"Seeing" the atmosphere in cross section has only recently become possible through the development of lidar. This new perspective should greatly help meteorologists to better understand the atmosphere and its capacity for diluting pollutants. Although the conventional lidar technique using direct backscattering has some basic limitations for applications beyond those in this study, a number of these can be overcome with advanced techniques currently under development, such as the use of multiple wavelengths. In addition, the operation of lidar systems in conjunction with other types of remote sensing devices offers considerable promise for the achievement of more comprehensive atmospheric measurements in days to come.

REFERENCES

Allen, R. J., and W. E. Evans, 1972: Laser radar (LIDAR) for mapping aerosol structure. Rev. of Sci. Inst., 43, 1422-1432.

Barrett, E. W., and O. Ben-Dov, 1967: Applications of the lidar to air pollution measurements. J. Appl. Meteor., 6, 500-515.

Clarke, J. F., 1969: Nocturnal boundary layer over Cincinnati, Ohio. Mon. Wea. Rev., 97, 582-589.

Collins, R.T.H., 1970: Lidar. Appl. Optics, 9, 1782-1788.

Gambling, D. J., and K. Bartusek, 1970: Lidar observations of tropospheric aerosols. Technical Report, Dept. of Physics, the University of Adelaide, Adelaide, Australia.

Gifford, F. A., 1971: Peak to mean concentration ratios according to a "top-hat" fluctuating plume model. Proceedings, AMS Conference on Air Pollution Meteorology, Raleigh, N.C., April 1971.

Hall, F. F., 1972: Temperature and wind structure studies by acoustic echo sounding. Remote Sensing of the Troposphere, Chapter 18, V. E. Derr, editor, Government Printing Office.

Hamilton, P. M., 1966: The use of lidar in air pollution studies. Int. J. Air/Water Poll., 10, 427-434.

Hamilton, P. M., 1967: Plume height measurements at Northfleet and Tilbury Power Stations. Atmos. Environ., 1, 379-387.

Hamilton, P. M., 1969: The application of a pulsed-light-rangefinder (lidar) to the study of chimney plumes. Phil. Trans. Roy. Soc. Lond., A265, 153-172.

Hosler, C. R., and T. J. Lemmons, 1972: Radiometric measurements of temperature profiles in the planetary boundary layer. J. Applied Met., 11, 341-348.

Preceding page blank

Johnson, W. B., 1969a: Lidar applications in air pollution research and control. J. Air Poll. Contr. Assoc., 19, 176-180.

Johnson, W. B., 1969b: Lidar observations of the diffusion and rise of stack plumes. J. Appl. Meteor., 8, 443-449.

Johnson, W. B., 1971: Lidar measurements of plume diffusion and aerosol structure. Proceedings, AMS Conference on Air Pollution Meteorology, Raleigh, N.C., April 1971.

Johnson, W. B., and E. E. Uthe, 1971: Lidar study of the Keystone stack plume. Atmos. Environ., 5, 703-724.

Johnson, W. B., W. F. Dabberdt, F. L. Ludwig, and R. J. Allen, 1971: Field study for initial evaluation of an urban diffusion model for carbon monoxide. Comprehensive Report, Contract CAPA-3-68 (1-69), NTIS Accession No. PB-210820, Stanford Research Institute, Menlo Park, California.

Little, C. G., 1972: Status of remote sensing of the troposphere. Bull. Amer. Met. Soc., 53, 936-949.

McAllister, L. G. 1972: Acoustic radar sounding of the lower atmosphere. Mathematics of Profile Inversion, NASA Technical Memorandum, NASA TMX-62, 150.

McCormick, M. P., and W. H. Fuller, 1971: Lidar applications to pollution studies. AIAA Paper No. 71-1056, Joint Conference on Sensing of Environmental Pollutants, Palo Alto, Calif., November 1971.

Olsson, L. E., W. L. Tuft, and W. P. Elliott, 1971: Observational study of the haze (mixing) layer in Western Oregon using laser radar, instrumented aircraft, and meteorological balloons. Paper presented at the 64th Annual Meeting of the Air Pollution Control Association, Atlantic City, New Jersey.

Pooler, F., and L. E. Niemeyer, 1970: Dispersion from tall stacks: an evaluation. Paper No. ME-14D presented at the Second Intern. Clean Air Congress, Washington, D.C., December 1970.

Schiermeier, F. A., and L. E. Niemeyer, 1970: Large Power Plant Effluent Study (LAPPES)--Vol. 1, Instrumentation, Procedures, and Data Tabulations (1968). NAPCA Publication No. APTD 70-2.

Schiermeier, F. A., 1970: Large Power Plant Effluent Study (LAPPES)--Vol. 2, Instrumentation, Procedures, and Data Tabulations (1967 and 1969). EPA Publication No. APTD-0589.

Schiermeier, F. A., 1972a: Large Power Plant Effluent Study (LAPPES)--Vol. 3, Instrumentation, Procedures, and Data Tabulations (1970). EPA Publication No. APTD-0735.

Schiermeier, F. A., 1972b: Large Power Plant Effluent Study (LAPPES)--Vol. 4, Instrumentation, Procedures, and Data Tabulations (1971). EPA Publication No. APTD-1143.

Scorer, R. S., 1958: Natural Aerodynamics. Pergamon Press, London and New York, 211-212.

Shaw, N. A., 1972: Acoustic sounding techniques for monitoring atmospheric structures. Argonne National Laboratory, Annual Report 1971-72 (ANL 7860).

Singer, I. A., and M. E. Smith, 1966: Atmospheric dispersion at Brookhaven National Laboratory. Intern. J. Air and Water Poll., 10, 125-135.

Uthe, E. E., 1972: Lidar observations of the urban aerosol structure. Bull. Amer. Met. Soc., 53, 358-360.

Uthe, E. E., and W. B. Johnson, 1971: Lidar observations of the lower tropospheric aerosol structure during BOMEX. Final Report, Contract No. AT(04-3)-115, Project Agreement No. 83, Stanford Research Institute, Menlo Park, Calif.

Uthe, E. E., and N. A. Shaw, 1973: A comparison of atmospheric structure as observed with lidar and acoustic sounder techniques. Paper presented at the Fifth Conf. on Laser Probing of the Atmosphere, Williamsburg, Va., June 1973.

Viezee, W., and J. Oblanas, 1969: Lidar-observed haze layers associated with thermal structure in the lower atmosphere. J. Appl. Meteor., 8, 369-375.

Appendix A

MARK VIII LIDAR SYSTEM DETAILS--
REPRINT OF JOURNAL ARTICLE* ENTITLED
"LASER RADAR (LIDAR) FOR MAPPING AEROSOL STRUCTURE,"
BY R. J. ALLEN AND W. E. EVANS

*Rev. Sci. Instruments, 43, October 1972.

Reprinted from:
THE REVIEW OF SCIENTIFIC INSTRUMENTS VOLUME 43, NUMBER 10 OCTOBER 1972

Laser Radar (LIDAR) for Mapping Aerosol Structure*

R. J. ALLEN AND W. E. EVANS
Stanford Research Institute, Menlo Park, California 94025
(Received 16 February 1972; and in final form, 20 March 1972)

This paper describes a third-generation experimental Q-switched, ruby laser radar or lidar useful for air pollution mapping and meteorological studies. This system differs from its predecessors in that it incorporates (1) automatic inverse-range-squared receiver gain compensation, (2) coaxial transmitter and receiver optics, (3) automatic scanning and pulsing at equal angle increments or time intervals for fixed operation, and at equal distances traveled for mobile operation, and (4) video disk storage and instant replay of scan sequences. Details of these improvements are included. Photographs of typical displays are also included to illustrate atmospheric returns recorded during range–height mapping of a smoke plume from an industrial plant, showing a cross section of the plume's structure; plan position mapping of the effluents from several industrial plants, indicating those emitting particulates; and distance–height mapping, showing differences in pollution and changes in the height of the inversion layer obtained while driving through a city.

INTRODUCTION

The development of the laser radar or lidar, as it has come to be known, has indeed provided a useful research tool for the study of the atmosphere, as predicted by Northend, Honey, and Evans[1] early in 1966. A third-generation ruby lidar has now been built—mounted within a truck (Fig. 1)—and is in operation mapping effluents from smoke stacks, smog layers above urban areas, the height of the inversion layer, and other related air pollution and meteorological phenomena.[2] This lidar system not only provides an improved instrument for air pollution and meteorological research but also a useful daytime or nighttime means for mapping the sources of effluents over a portion of a city from a single vantage point.

The new lidar system, called the SRI/NAPCA Mk VIII, was developed jointly under the sponsorship of Stanford Research Institute and the National Air Pollution Control Administration (now the Environmental Protection Agency). The primary improvements of the Mk VIII over its predecessors are described in this paper, along with the over-all system design and typical displays obtainable during field observations. The basic lidar system equations, receiver noise considerations, and general system parameters important in the design and use of the lidar were included in a previous paper[1] and should be reviewed for a greater understanding of the principles of lidar systems.

I. SYSTEM CONSIDERATIONS

For SRI lidar systems developed prior to the Mk VIII, it has been the practice to display and photographically record each individual oscilloscope trace or family of oscilloscope traces.[3] The log amplitude of the return signal shown in the photographic record is read manually at various ranges, as dictated by slope considerations and points of inflection in the trace. These data are analyzed and subsequently plotted automatically by special computer programs that account for $1/R^2$ corrections.[4] The plots produced by the computer include those that show the vertical cross section of particulate matter intercepted by the transmitted laser beam and indicate the gross relative concentrations.

One Mk VIII design goal was to incorporate a real-time display that would indicate in raster or map form the location, spatial distribution, and approximate concentrations of particulates relative to clear air and thus would allow an on-the-spot inspection of the atmospheric area being surveyed. At the same time, the data obtained were to be preserved for later computer processing and refinement. This goal presented some unique requirements due to the limited prf (30 pulses/min) and narrow transmitted beamwidth (under 1 mrad) satisfactory for obtaining the required performance during field observations. The bandwidth requirements to handle the narrow pulse widths (under 30 nsec) also presented some major limitations.

The system selected incorporates some unique signal processing circuitry and control logic, together with a television-type instant playback disk memory. This allows real-time display, as well as data recording (with some bandwidth limitations) for off-line processing. Either a radar type PPI (plan-position indication) or an RHI (range–height indication) intensity-modulated display format can be selected. A-scope and other derivations of the radar type display are also obtainable, as indicated later.

To obtain a uniform low-brightness two-dimensional presentation representing a clear air return at all ranges, it was necessary to correct for the inverse-range-squared ($1/R^2$) decay of the received usable signal. In principle, this could be accomplished in either the photomultiplier tube (PMT) or in the post-detection amplifier. Since a large dynamic range (>5 decades) was involved, the former method was selected to minimize PMT and amplifier saturation effects, especially for operation within a foggy atmosphere when the dynamic range of the useful signal information is very large. Over-all PMT gain can be

Preceding page blank

controlled by varying the gain of individual dynodes[5] or of combinations of dynodes. The objective is to control the total gain for a series of k dynodes (δ^k) in such a manner that the ratio of $\delta^k(t)/R^2$ will remain constant.

Recording of an elevation or azimuth angle label along with each lidar shot was circumvented and the display electronics were simplified by assigning addresses to appropriate locations on the disk. These details of the lidar design are described in Sec. II.

II. LIDAR DESIGN

A. System Description and Timing

The lidar system (Fig. 2) consists of the laser transmitter and receiver, parts of which are mounted on the pedestal—together with the coaxial optics—and called the "lidar head"; the head and pedestal position control; the video processing and storage section; and the displays. Position control of the head and pedestal and firing control can be either automatic or manual. In the automatic mode, the firing rate can be controlled in increments of time or increments of the distance traveled by the truck in which the Mk VIII is mounted. Between selectable limits, the pedestal can be moved automatically from left to right, and the lidar head can be moved automatically from horizontal to vertical and back to horizontal, in equal increments of degrees between shots. After the scan has been completed, the lidar can be programmed either to stop or to return immediately and repeat the scanning sequence. The head and pedestal can also be locked in a fixed position with the firing maintained at an automatic rate.

In the manual mode, the head can be stepped, and the firing can be controlled at will either from the head location or remotely from the electronics console. After a firing sequence has been completed the position control programmer can be used for sequentially addressing the video disk for immediate playback and display of the recorded signals. A volume control and speaker allow the program control pulses to be heard, a feature which has been found useful in monitoring the progress of an experiment.

The time between the manual or automatic command to fire the lidar and the actual lase is varied slightly to maintain proper phasing with the disk. Four main times are identified in Fig. 3 as GO, MATCH, FIRE, and LASE. The GO pulse occurs when the command to fire a shot is given. Whenever the disk address matches the externally specified address, the MATCH time occurs. Since the disk is rotating at 30 rps, the MATCH time can be any time from 0–66 msec after the GO time, depending upon the disk position at the time of GO.

The time between MATCH and FIRE is adjustable between 100 and 1000 μsec by a front-panel control. This adjustable MATCH–FIRE delay is provided so that the entire firing and subsequent recording process can be

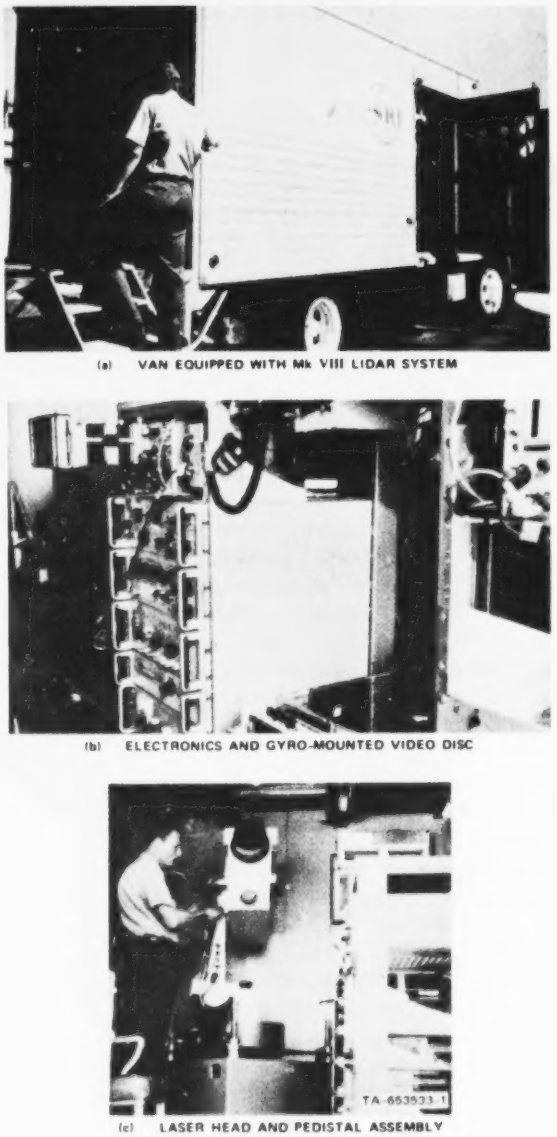

FIG. 1. View of van and Mk VIII lidar system.

delayed with respect to the disk-lidar coincidence time. The delay is used (1) to compensate for phase shifts introduced when a recorded disk is removed and later replaced at a slightly different angular position, (2) to offset a new data sequence slightly so that records will interleave between previously recorded records for fuller utilization of the available disk storage capacity, and (3) to provide time for the disk circuits to transfer between the read and write modes when the display is operated in a read-between-the-shots manner.

The FIRE time occurs when the signal is given to the

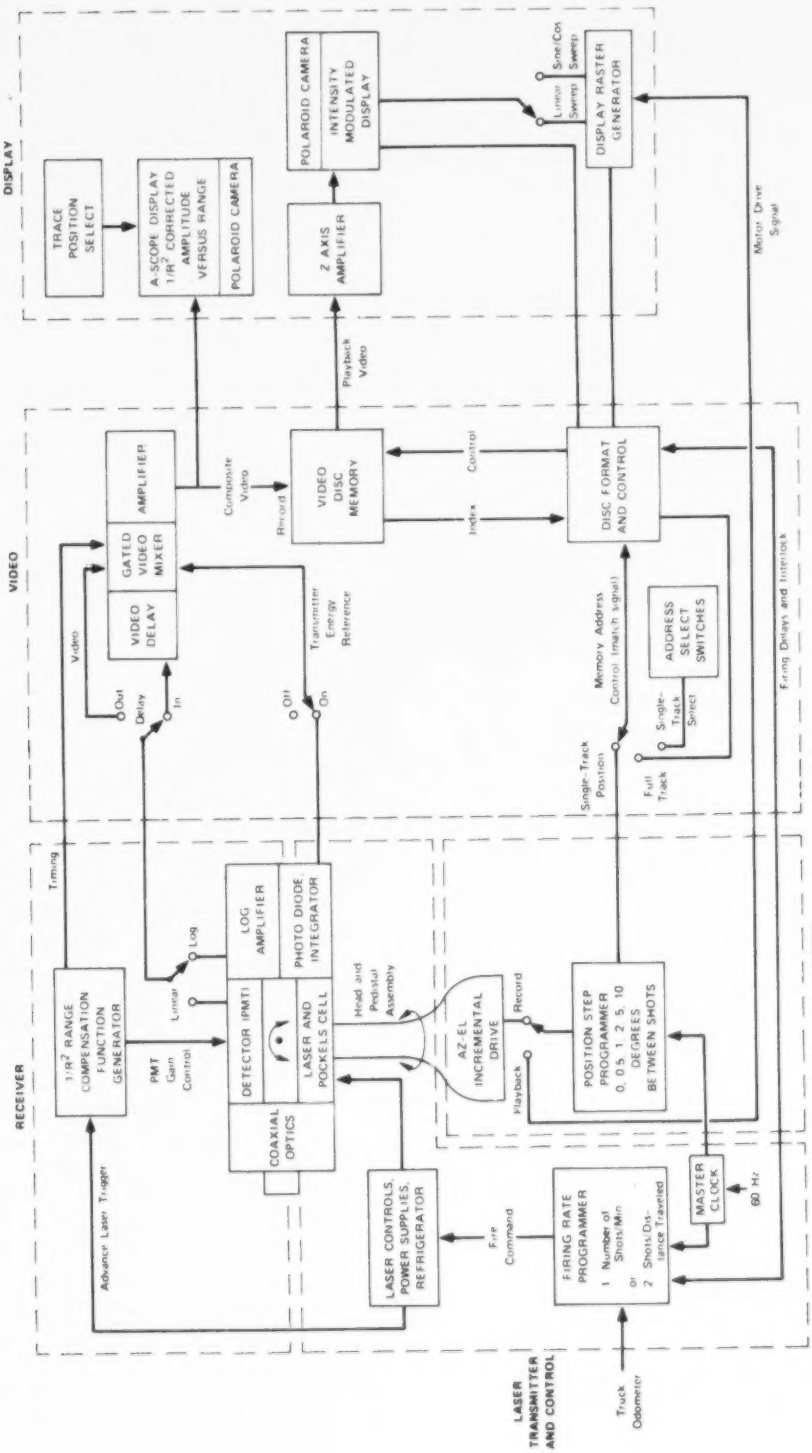

FIG. 2. Block diagram of the Mk VIII lidar system.

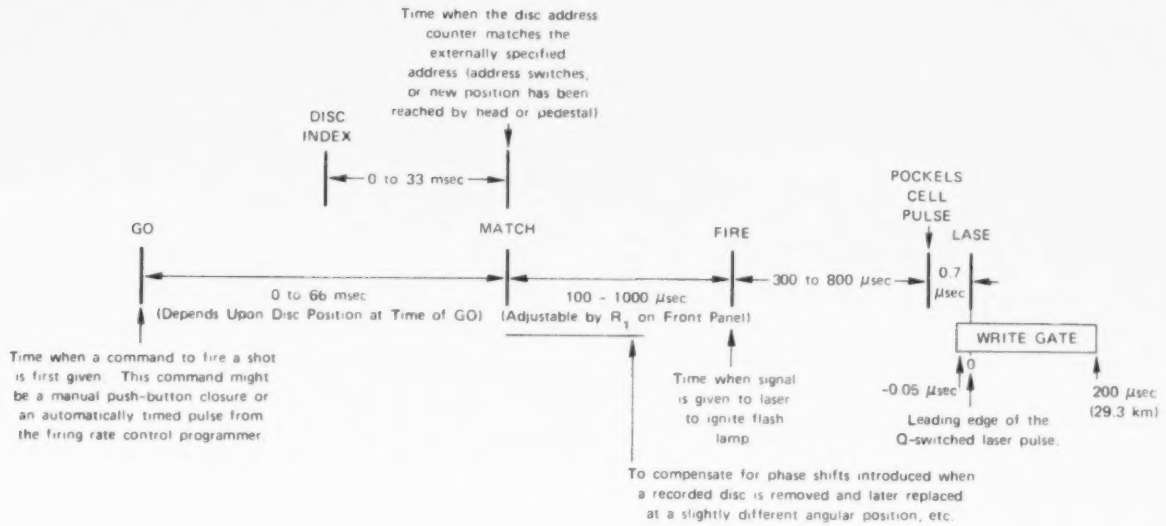

FIG. 3. Lidar system main timing.

laser to ignite the flash lamp. The actual LASE time, however, in this Holobeam laser system, is between 300 and 800 μsec later to permit maximum utilization of the flash lamp pump energy. This delay is adjusted by a front-panel control on the Pockels cell console.

An adjustable width WRITE GATE command to the disk memory unit telling it to record the video signal is issued slightly prior to the actual lase. By limiting the maximum range to 27.7 km (185 μsec), all shots can be recorded on a single track when the system is stepping in 1.0° increments from 0° to 180°. Reducing the WRITE GATE to 92 μsec allows recording 360 shots on a single track.

Repositioning the head or pedestal for the next firing actually is started immediately after each firing. Stepping follows in 0.1° increments at 60 steps/sec, allowing 10° to be stepped and settled between shots at the maximum firing rate of 30 pulses/min.

B. Coaxial Transmitter and Receiver Optics

Previous SRI lidar systems have used separate receiver and transmitter optical systems. Full convergence (overlap) of the transmitter laser beam and the receiver field of view has not normally been achieved within about 200–500 m of the front of the lidar, limiting the minimum range of operation. Coaxial transmitter and receiver optics were incorporated within the Mk VIII to allow closer-in operations.

Coaxial operation was accomplished by installing a front-surfaced elliptical mirror suspended on the same spider as the receiver secondary mirror and centered back to back within a Newtonian reflecting telescope (see Fig. 4). Double-concave and -convex AR coated lens enlarged the 9.5 mm laser beam from the rod to a 5 cm transmitted beam, decreasing the angular divergence from about 3 to $\frac{1}{2}$ mrad. This is a slightly greater divergence than that of the previous systems using a 15 cm primary transmitting mirror; however, the close-in capabilities ($> \approx 50$ m) are a worthwhile tradeoff. Provision was made for adjusting the position of the negative lens to ensure minimum laser spot size on a distant target. A removable prism and plug were provided to allow alignment of the laser cavity.

The laser is a standard Holobeam 300 series, Pockel's cell Q-switched ruby system. Optical pumping of the laser rod is accomplished by exciting a helical xenon-filled arc discharge lamp. Optimum pumping efficiency is achieved by a highly reflective noncorrosive reflector surrounding the flash lamp. The entire inside volume of the head is filled with circulating water to cool all the inside components.

A glass beam splitter, located at 45° with respect to the laser beam axis behind the rear mirror, reflects a small fraction of the incident laser beam that has leaked through the mirror. This is directed onto a ground glass diffuser which minimizes changes in apparent peak power levels due to hot spots within the laser rod. Light pipes direct the light pickup through a step optical attenuator and receiver narrow-band filter to the PMT. This feedback light path can then be used to produce an adjustable amplitude, zero time reference roughly proportional to the peak power transmitted, which is recorded and processed along with the return signal.

In addition, the energy of the transmitted laser beam is measured with a photo-diode pickup also located to detect the rear-mirror leakage. The output from the diode is integrated in a capacitor to produce a pulse at the start of

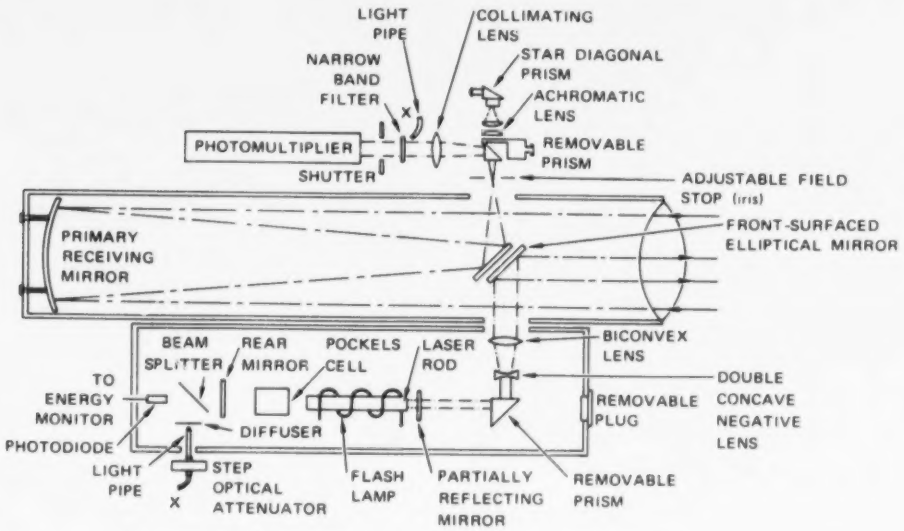

FIG. 4. Mk VIII transmitter and receiver coaxial optics.

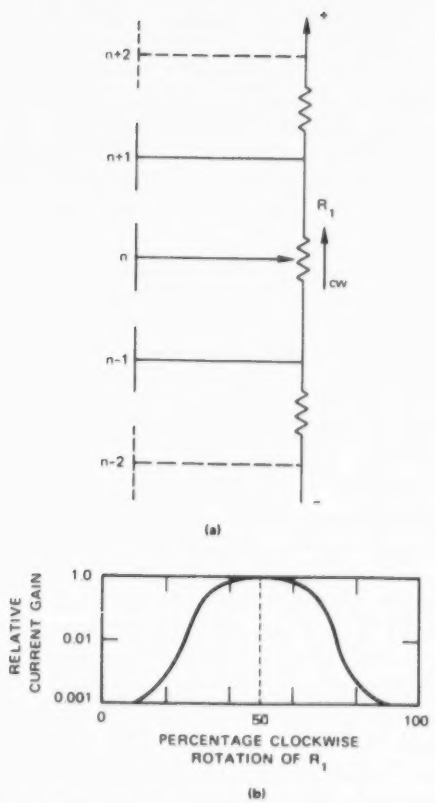

FIG. 5. (a) Test circuit for measuring dynode gain control characteristic. (b) Photomultiplier gain vs single dynode potential control.

the return trace whose amplitude is proportional to the energy transmitted. This energy pulse can also be inserted into the video trace at the option of the experimenter.

The lidar receiver (upper half of Fig. 4) consists of a 15 cm Newtonian telescope, an adjustable field stop, a removable prism, a collimating lens, a narrow-band filter, a shutter, a PMT, and an eyepiece/prism/lens arrangement. Radiation incident on the parabolic primary mirror is imaged by the diagonal secondary mirror onto the focal plane. An adjustable iris in the focal plane limits the receiver field of view to solid angles from 0.5–5.6 mrad. Radiation passing through the iris is normally collimated by a relay lens, passed through a narrow-band filter, and focused onto the PMT. A camera shutter and iris assembly are located directly in front of the PMT cathode. The removable prism can be opened to permit boresighting the telescope with a quick-alignment externally mounted riflescope and coaligning the receiver and transmitter axes.

C. Range Attenuation Compensation

The purpose of the range compensation function generator is to produce a modulating waveform for the PMT dynode chain that will increase the gain of the PMT according to the same function of time, or range, as the *in vacuo* decrease of the lidar return signals, i.e., $1/R^2$. As a result, the return signal levels at the output of the PMT will be independent of range over the controlled region. Numerous methods exist for dynamically varying the gain of photomultiplier tubes.[6,7] The one used here, which we have not seen described elsewhere, is simple and has been

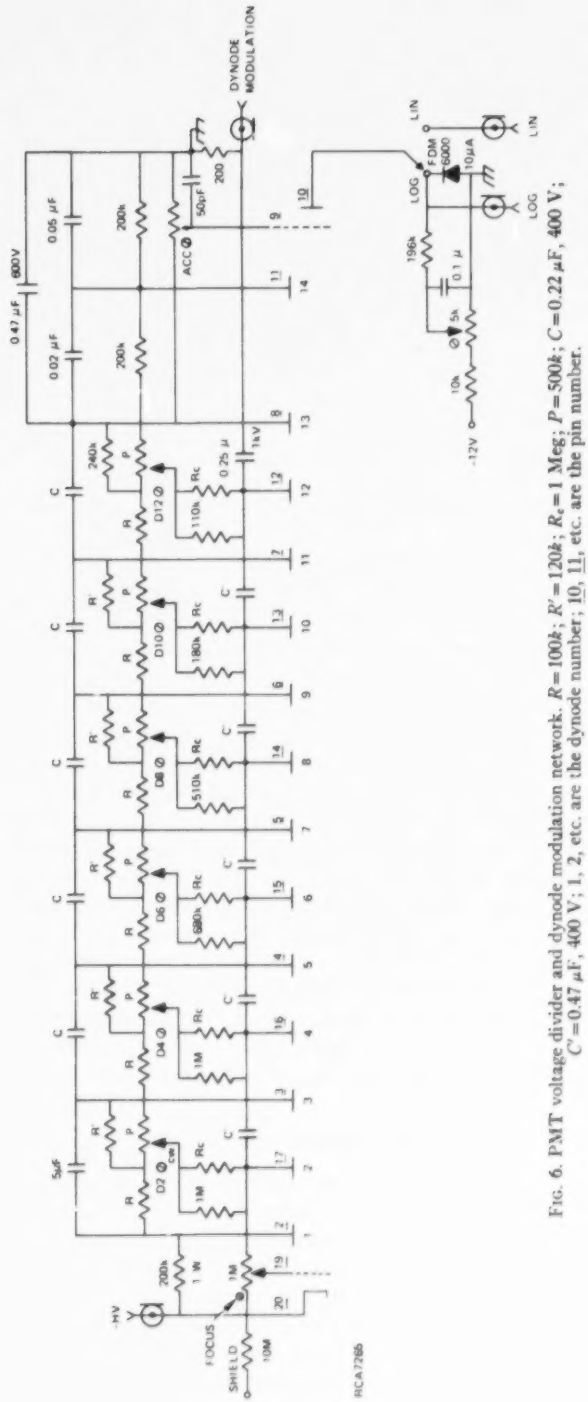

FIG. 6. PMT voltage divider and dynode modulation network. $R = 100k$; $R' = 120k$; $R_c = 1$ Meg; $P = 500k$; $C = 0.22$ μF, 400 V; $C' = 0.47$ μF, 400 V; 1, 2, etc. are the dynode number; 10, 11, etc. are the pin number.

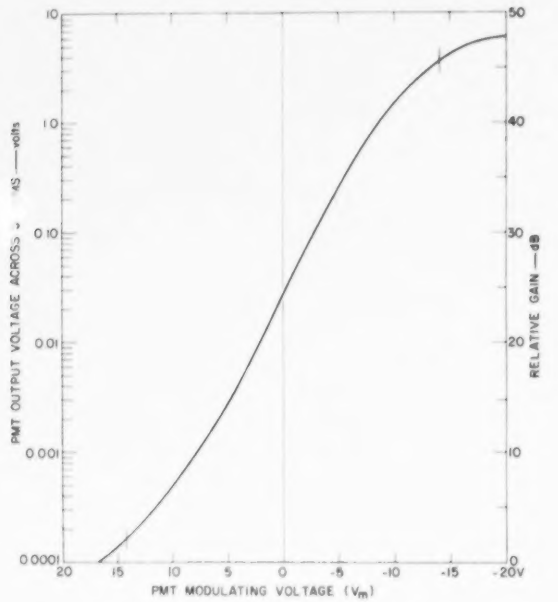

FIG. 7. Signal output from 7265 PMT vs modulating voltage supplied to six dynodes. HV = − 2400 V.

found to be well suited to our application, which requires fairly precise control over a large gain range.

The principle is illustrated in Fig. 5(a), where the potential of dynode n can be varied, from that of its next lower neighbor $n-1$ to that of its next higher neighbor $n+1$, by potentiometer R_1.

As R_1 is turned clockwise, the electron multiplication gain of the $(n-1)$ to n portion of the circuit increases and the gain of the n to $(n+1)$ portion decreases. The rates of these two opposing effects are different, however, with the result that the over-all gain of the two-stage combination varies over the hump-shaped characteristic shown in Fig. 5(b). The over-all gain can be controlled over a range of approximately 100:1 per stage pair, on either side of a broad maximum that occurs when the potential of dynode n is midway between the potentials of its two neighbors. Over a gain range of 10:1, the control characteristic is relatively linear in decibels vs volts. For the RCA 7265 and Ampex 56TVP photomultipliers, we have found a slightly more linear control characteristic on the positive side of the hump.

A principal feature is that the control procedure just described can be applied to a number of stage pairs in the dynode string, with independent and cumulative results. The same control voltage waveform can be capacitor or transformer coupled to each of the modulating stage pairs, and the maximum modulating voltage will always be well below 100 V. With the fixed-potential dynodes well

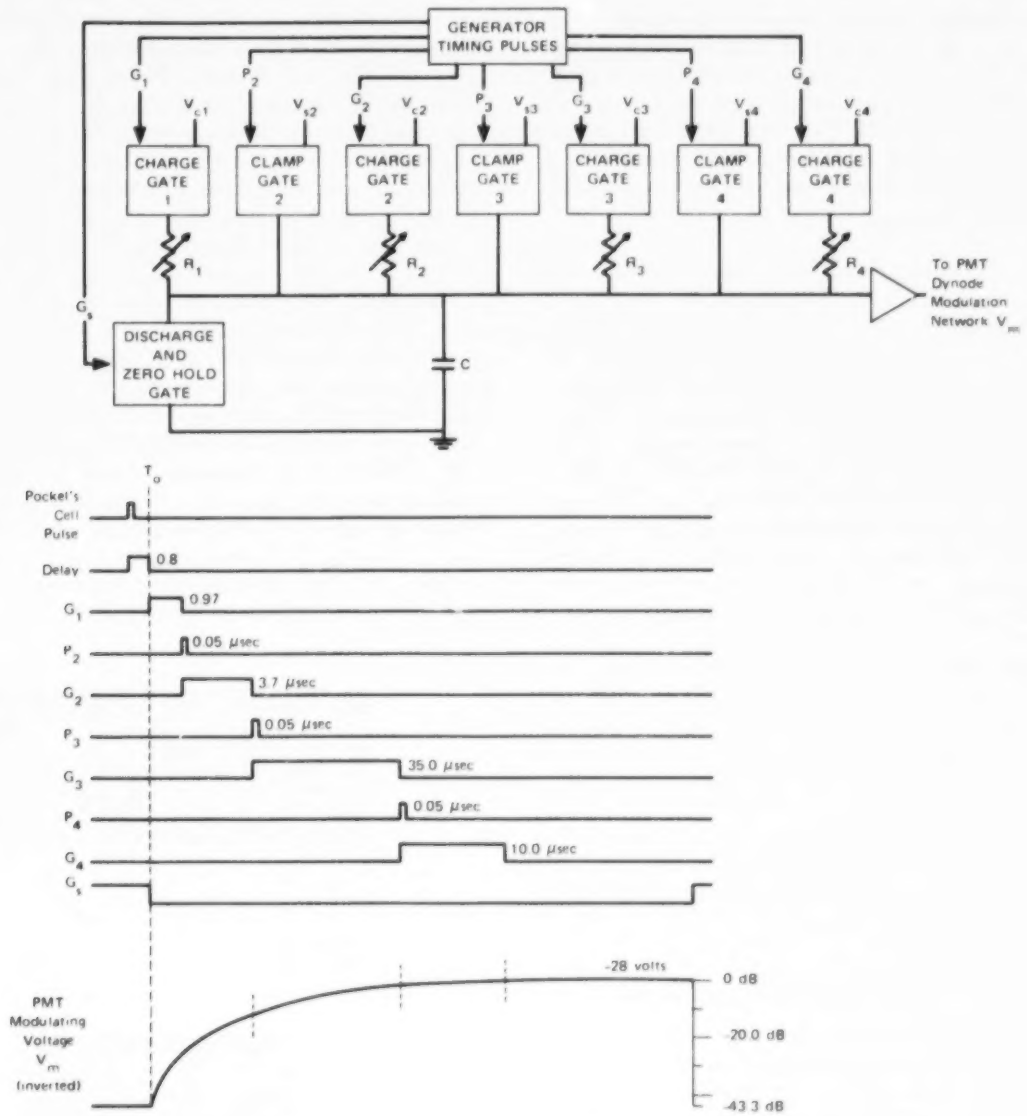

FIG. 8. Simplified block diagram of range compensation function generator, timing pulses, and modulating waveform.

bypassed to ground, much less capacitive coupling of the modulating waveform to the output electrode (anode) occurs than in the more usual case where the entire voltage divider is pulsed.

The complete photomultiplier circuit for the Mk VIII lidar is shown in Fig. 6. Normally each of dynodes D_2, D_4, D_6, D_8, D_{10}, and D_{12} is statically "detuned" by 7.5 dB (referred to input radiant power) by its associated potentiometer. This detuning desensitizes the receiver during its standby or interpulse periods and prevents anode overload from bright sky backgrounds. Immediately following each lidar transmitter pulse, the PMT gain is increased through a controlled range of 43.3 dB by a specially shaped negative-going 28 V modulating waveform.

The experimentally determined gain curve for an RCA 7265 photomultiplier with modulation on six dynodes is given in Fig. 7. The indicated end points define a range (referred to received signal power) over which the gain is controlled. This permits compensation for the $1/R^2$ signal dropoff over a range variation of 150:1. The actual span chosen was from a range of 50 m (0.333 μsec round trip delay) out to 7.5 km (50 μsec round trip delay). For ranges

less than 50 m, severe receiver overload is prevented by the fact that the receiving field of view is not well focused onto the coaxial transmitter beam. For reception beyond 7.5 km, the PMT gain is maintained at its maximum value for an additional 150 μsec (22.5 km), after which it is reduced to its minimum value to await the next shot. This low duty cycle operation limits the average anode current of the PMT to a safe value even for operation into a bright daylight sky.

The PMT modulating waveform V_m is approximated to yield a system accuracy of ±1 dB by four RC exponential charge curve segments generated in succession to form a continuous curve. A simplified diagram of the V_m generator, the gating control signals, and the PMT modulating voltage curve is shown in Fig. 8; V_m is produced across a single capacitor by three types of control circuits: DISCHARGE, CHARGE, and CLAMP. The DISCHARGE circuit discharges the capacitor and holds it at 0 V except during the presence of the adjustable control gate signal G_s, which disables the circuit, allowing the V_m waveform to be generated. The CHARGE circuit applies a preset charging voltage V_c through an adjustable resistor to the capacitor for a time interval determined by a preset control gate signal G. The CLAMP circuit clamps the capacitor to a selected starting voltage V_s during the short period of the clamp control pulse P at the beginning of each curve segment, except the first segment, which starts at 0 V. Thus, for the generation of the required four-segment waveform, one DISCHARGE circuit, three CLAMP circuits, and four CHARGE circuits are used. All the circuits of each type are identical, except for the components that control the differences in the curve segment characteristics.

D. Video Processing, Storage, and Display

The received range-compensated signal (and any noise) from the PMT can be routed either through a log amplifier or directly to the video section. Approximately 5 decades of wideband logging were achieved by employing an FDM 6000 diode directly in the PMT anode circuit and measuring the video voltage developed across it, by incorporating a Tektronix P6045 FET probe.

The transmitter energy reference pulse can be mixed with the output from the FET probe (Fig. 2). Mixing is controlled by an adjustable gating signal from the timing pulse generator in the range compensation unit and is accomplished in a gated integrated-circuit video amplifier. The gating signal is set to provide a 1 μsec reference energy pulse at the start of the video return trace. Video from the PMT may be delayed for 2 μsec (300 m) in a delay line when desired, to separate the transmitted energy reference and the close-in return trace. After amplification, the composite video is routed to the video disk memory for recording and later playback, and to the A-scope for immediate display and recording on Polaroid film.

Since the video disk rotates at 1800 rpm and is used in a mobile van, it is placed in gimbals to reduce the stress put on its drive shaft and bearings by the gyroscopic action. The bandwidth of the disk limits the range resolution of the recorded data to about 35 m. For occasions when more detailed quantitative data are required, the A-scope Polaroid method is used. Several returns can be placed on one Polaroid print by electronically positioning each trace between shots, with a manual positioning selector. A typical A-scope presentation is shown in Fig. 9(b).

Each return following the laser pulsing is stored in a given slot on the disk, controlled by either the setting of manually adjustable address switches or the position of the lidar head or pedestal. Full track addressing for ERASE or PLAYBACK is also selectable.

During playback from the disk, the recorded video signal is routed through a wideband Z-axis amplifier to a modified Tektronix 453 CRO. A display raster generator, controlled by signals from the position step programmer, provides either R-θ or rectangular rasters selectable for the type of

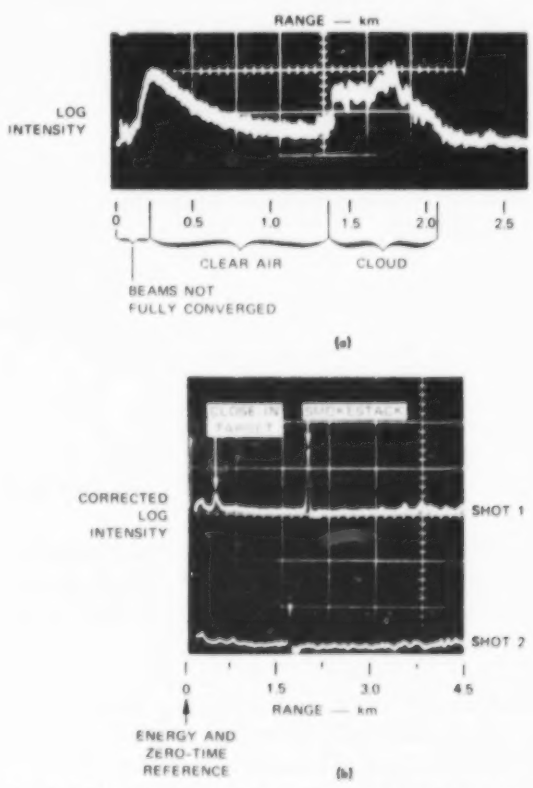

FIG. 9. Typical A-scope displays comparing Mk VIII and Mk V returns. (a) Mk V A-scope display without correction; (b) Mk VIII A-scope display with automatic inverse-range-squared ($1/R^2$) correction.

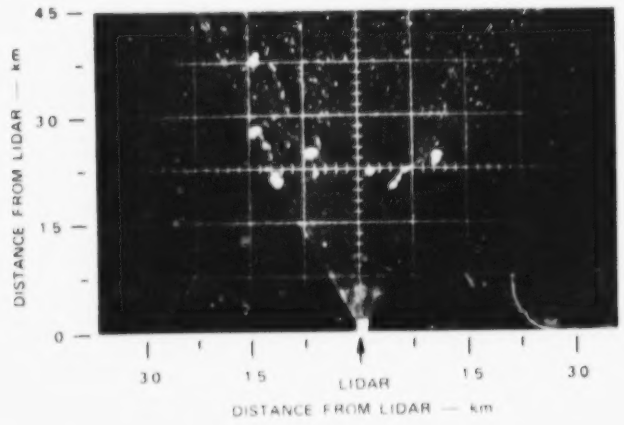

(a)

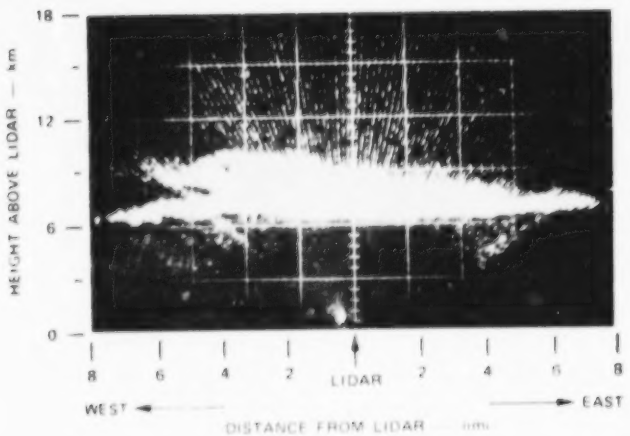

(b)

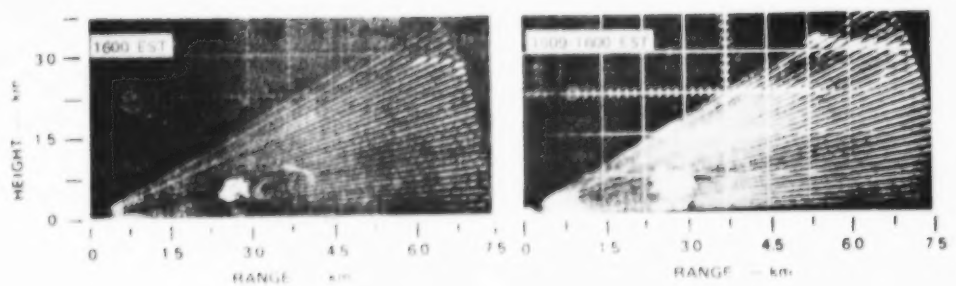

(c) (d)

FIG. 10. DSS playbacks using sin-cos sweep display. (a) Horizontal fan above an industrial area showing location of particulate sources; (b) overhead vertical fan showing cloud structure; (c) low angle vertical fan through plume, showing its cross section; (d) composite of a sequence of runs including (c) showing the plume spread and mixing.

experimental observation. Two types of $K\theta$ generators are available. One obtains the required sine- and cosine-modulated ramp waveforms via fast analog multipliers and provides a real-time display of all returns stored on a single track of the disk; i.e., up to 360 traces. The second type obtains the display sweeps with a sine–cosine potentiome-

ter mechanically coupled to a small stepper motor driven in parallel with the main stepper motor in the pedestal. This provides a geometrically more precise display than we have yet been able to obtain with the electronic "quick-look" circuit, but its use is limited to time-exposure photographic recording because of the restrictions on mechanical stepping speed and potentiometer wear. The displays discussed later (Fig. 10) were made by playing back the disk-recorded signals through the sin–cos potentiometer system. Somewhat better range resolution can be obtained by operating directly with the lidar output and exposing the photograph during the lidar scan, but because of the several chances for error, such real-time photography in the field is avoided where possible.

III. TYPICAL DISPLAYS OBTAINED DURING FIELD OBSERVATIONS

Since its completion, the Mk VIII lidar system has been used for observations at various locations within the United States. Typical display photographs are shown in Figs. 9–11. Figure 9 illustrates the difference between the A-scope presentation with and without $1/R^2$ correction. Figure 9(a) is a photograph obtained from an earlier model (Mk V) lidar while looking at a cloud. The first part of the return indicates that the transmitted beam and the receiver field of view were not fully overlapping (had not converged) until about 0.2 km. This is to be expected, since the Mk V transmitter and receiver optic axes are separated. Examination of the first part of the return in Fig. 9(b) shows a close-in target, indicating the advantages of the Mk VIII coaxial optics.

A second difference is the exponentially decaying return from clear air in the range of 0.2–1.3 km for the Mk V compared to a relatively flat clear air return within this region for the Mk VIII. Signals only appear above the base line for this $1/R^2$ corrected system. This allows the gain of the 'scope to be operated at a higher level when smaller signals are being examined.

Figure 10 shows 'scope photographs obtained by using the sin/cos sweep during disk playback. Figure 10(a) was obtained by scanning in equal azimuth steps over a horizontal plane, thus producing a horizontal fan over the area probed. This display is similar to a plan-position indication (PPI) display of a radar monitoring the position of ships within a harbor. In the lidar case, the scanned area is above several smokestacks located in an urban industrial area. The bright spots are the approximate locations of the source of the particulates; when superimposed over a map of the area, they correlate closely with the locations of the smokestacks producing the particulates polluting the atmosphere.

Figure 10(b) shows the display obtained after playback following an overhead vertical probe. The lidar was stepped in equal elevation angles, thus producing an overhead vertical fan pattern showing the structure of a cloud with its base around 6 km. Particulates suspended above the cloud appear as bright streaks, and pockets of particulates trapped below the cloud appear as bright areas.

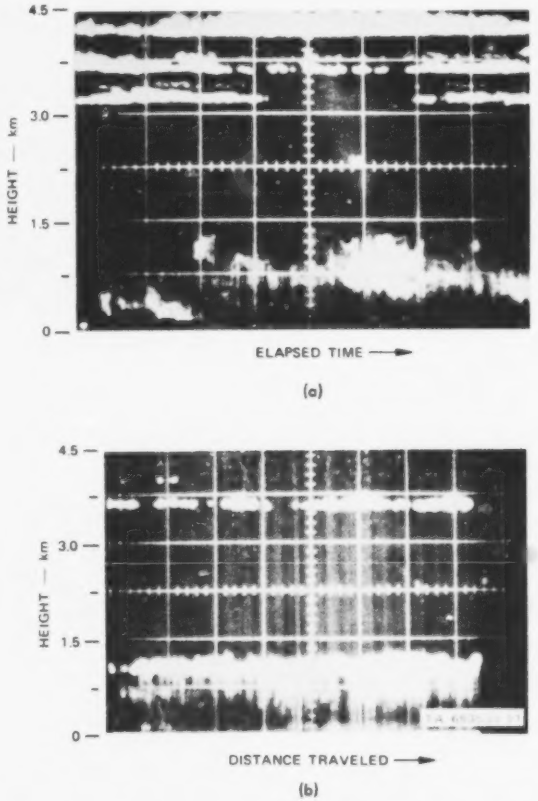

FIG. 11. Disk playback using linear sweep display. (a) Vertical time lapse showing changes of smog layer and clouds as a function of time; (b) vertical profile obtained while driving along freeway through an urban area. Smog trapped below inversion layer and cloud structure above are shown.

The downwind cross section of a smoke plume is shown in Fig. 10(c) and (d). The lidar was stepped in equal elevation steps from about 0°–60° above horizon, cutting through the plume 1.6 km downwind from the plant. The display produced is similar to a radar range–height indication (RHI). Figure 10(c) was produced from a single elevation scan; this type scan was first reported by Hamilton.[8] Figure 10(d) was produced from the disk playback of several elevation scans over the same vertical fan area in space.

The photograph in Fig. 11(a) was produced following a run with the lidar head in a fixed position, pointed straight up. The pulsing of the laser was in equal increments of time, with the returns being recorded as the smog and cloud

layers passed overhead. Changes can be seen in the concentrations of particulates within the smog layer and in the cloud formations with the passage of time. Lane, Ashwell and Dagnall[9] obtained some similar results using a pulsed neodymium system.

Finally, Fig. 11(b) shows a display of a vertical profile above an urban freeway. It was recorded on disk while driving along the freeway; by a connection to the truck odometer, the lidar was pulsed in equal distances traveled by the truck. Pockets and areas of heavier particulate concentration can be correlated with the van position at the time of the recording.

ACKNOWLEDGMENTS

The authors gratefully acknowledge the work of R. T. Wolfram, who performed the design of the range-squared compensation unit, and of N. B. Nielsen, who assisted in the development, checkout, maintenance, and operation of the lidar system. Special appreciation is extended to Dr. W. B. Johnson whose foresight in establishing the major system specifications and whose over-all guidance contributed much to the success of this project.

* Work supported in part by the National Air Pollution Control Administration under Contract No. CPA 70-49.

[1] C. A. Northend, R. C. Honey, and W. E. Evans, Rev. Sci. Instrum. **37**, 393 (1966).

[2] W. B. Johnson, "Lidar Measurements of Plume Diffusion and Aerosol Structure," AMS Conf. of Air Pollution Meteorology, Raleigh, N. C., 1971.

[3] R. T. H. Collis, Bull. Amer. Met. Soc. **50**, 688 (1969).

[4] W. B. Johnson and E. E. Uthe, Atmos. Environ. **5**, 703 (1971).

[5] *Photomultiplier Manual*, RCA Tech. Ser. PT-61, Harrison, N. J., 1970.

[6] R. A. Kaplin and R. T. Daily, IEEE J. Quantum Electron. **QE-3**, 428 (1967).

[7] V. Cohen, Electron. Engr. **40**, 206 (1968).

[8] P. M. Hamilton, Phil. Trans. Roy. Soc. London **A265**, 153 (1969).

[9] J. A. Lane, G. E. Ashwell, and A. Dagnall, Atmos. Environ. **5**, 49 (1971).

Appendix B

LIDAR DATA SUMMARY: HOMER CITY EXPERIMENT

Appendix B

LIDAR DATA SUMMARY: HOMER CITY EXPERIMENT

Date (1970)	Site Number	Cross Section Number	Start Time (EST)	Azimuth Angle (Deg.)
3 May	36	1	1601	207
		2	1607	207
		3	1613	185
		5	1653	207
		6	1742	207
		7	1745	160
4 May	30	10	0801	309
		11	0804	339
		12	0807	009
		15	0837	309
		18	0850	309
		20	0906	309
5 May	20	27	0922	150
		28	0928	124
		29	0931	94
		30	0936	150
		31	0940	124
		32	0943	94
5 May	37	34	1113	214
		35	1118	184
		36	1121	154
7 May	37	43	1131	214
		45	1137	191
		46	1143	154
		47	1147	214
		48	1151	191
		49	1155	154
		50	1200	214
		51	1205	191
		52	1207	154
		53	1210	214
		54	1215	191
		55	1219	154
		56	1221	214
		57	1225	191
		58	1228	154
		66	1446	215
		67	1451	191
		68	1459	164
9 May	37	70	0656	221
		72	0702	170
		73	0706	221
		74	0708	195
		75	0711	170
		77	0723	221
		78	0726	195
		80	0	170
		82	0733	221
		83	0735	195
		84	0738	170
		85	0743	221
		86	0748	195
		89	0757	221
		90	0801	195
		91	0807	170
		92	0811	221
		93	0814	195
9 May	37	94	0817	170
		96	0827	221
		97	0830	195
		98	0836	170
		99	0840	221
		100	0844	195
		101	0847	170
		102	0906	221
		103	0912	221
		104	0914	195
		105	0917	170
		106	0919	221
		107	0922	195
		108	0925	170
		109	0935	221
		110	0938	195
		111	0942	170
		112	0946	221
		113	0949	195
		114	0952	170
		115	0954	221
		116	0956	195
		117	0959	170
		118	1003	221
10 May	37	165	0548	221
		166	0551	183
		167	0555	134
		168	0606	194
		169	0611	179
		170	0615	134
		171	0620	194
		172	0624	179
		173	0627	134
		174	0651	194
10 May	38	175	0858	184
		176	0901	154
		216	1245	206
		217	1252	206
11 May	37	221	1001	184
		222	1004	154
		223	1009	124
		224	1012	184
		225	1015	154
		226	1018	124
11 May	20	241	1322	151
		242	1325	123
		243	1329	104
		244	1332	151
		245	1335	123
		246	1337	104
		253	1400	123
		254	1402	123
		255	1405	123
		256	1409	123
		257	1411	123
		258	1414	123
		259	1416	123
		260	1418	123

Preceding page blank

Date (1970)	Site Number	Cross Section Number	Start Time (EST)	Azimuth Angle (Deg.)
11 May	20	261	1422	123
		262	1424	123
		264	1431	123
		265	1434	123
		266	1437	123
		267	1439	123
		268	1443	123
		269	1447	123
		270	1451	123
		271	1455	123
		272	1458	123
		273	1500	151
		274	1503	123
		275	1506	104
		276	1509	151
		278	1511	123
		279	1514	104
		280	1516	151
		281	1518	123
		282	1520	104
		286	1531	151
		287	1535	123
		288	1538	104
		289	1541	151
		290	1543	123
		292	1546	104
		293	1549	151
		294	1553	123
		295	1555	104
		297	1600	151
		298	1602	123
		299	1604	104
		301	1610	151
		302	1613	123
		303	1616	104
		304	1618	151
		305	1621	123
		306	1624	104
		307	1626	151
		308	1628	123
		309	1631	104
		310	1636	151
		311	1639	123
		312	1645	104
		313	1648	151
		314	1650	123
		315	1652	104
		316	1656	151
		317	1658	123
15 May	40	409	1008	
		410	1012	085
		411	1016	057
		417	1119	114
		418	1120	085
		419	1124	057
		420	1128	114
		421	1130	085
		422	1133	057
		423	1137	114
		424	1141	085
		425	1146	057
		426	1150	114
		427	1153	085
		428	1158	057
		429	1201	114
		430	1203	085
		431	1206	057
		432	1209	114
		433	1213	085
		434	1217	057
		435	1220	114
		436	1224	085
		437	1228	057
		438	1232	114
		439	1236	085
		440	1240	057
		441	1244	114
		442	1248	085
		443	1253	057
15 May	36	446	1426	239
		447	1429	264
		448	1432	289
		449	1435	239
		450	1438	264
		451	1441	289
		452	1444	239
		453	1446	264
		454	1450	289
		458	1503	239
		459	1506	264
		460	1509	289
		462	1525	239
		463	1529	264
		464	1531	289
		465	1536	239
		466	1540	264
		467	1545	289
		468	1548	239
		469	1553	264
		470	1555	289
		485	1647	239
		486	1649	264
		487	1651	289
		491	1700	239
		492	1703	264
		493	1704	289

Appendix C

LIDAR DATA SUMMARY--ST. LOUIS EXPERIMENT

Appendix C

LIDAR DATA SUMMARY--ST. LOUIS EXPERIMENT

Date (1971)	Time (CST)	Run No.	No. of Shots	Route Points	Length (miles)	Weather, Remarks
1 March (Mon.)	0938-0948	32	156	2-11	7.8	○10 060/15-20 32°
	0954-1000	34	94	11-13	4.7	
	1001-1008	36	120	13-14	6.0	
	1009-1018	38	130	14-16	6.5	
	1019-1026	40	120	16-17	6.0	
	1027-1038	42	160	17-4	8.0	
	1046-1055	44	140	4-9	7.0	○10 060/15 40°
	1056-1103	46	130	9-13	6.5	
	1105-1112	48	120	13-14	6.0	
	1113-1120	50	120	14-16	6.0	
	1121-1130	52	140	16-18	7.0	
	1131-1148	54	153	18-1	7.6	80○10 060/10 45°
	1315-1324	56	140	1-11	7.0	80○15○10 060°/10
	1325-1331	58	110	11-13	5.5	
	1332-1339	60	120	13-14	6.0	
	1340-1348	62	120	14-16	6.0	
	1349-1357	64	140	16-18	7.0	
	1358-1413	66	145	18-1	7.2	
	1426-1433	68	140	1-11	7.0	
	1434-1441	70	110	11-13	5.5	
	1442-1450	72	120	13-14	6.0	
	1451-1459	74	123	14-16	6.1	
	1500-1509	76	140	16-18	7.0	90○/○10 060/10 50°
	1510-1525	78	150	18-1	7.5	
	1623-1627	80	67	1-52	3.3	
2 March (Tues.)	0820-0830	82	158	1-11	7.9	150○7-10 360/10-15 31°
	0831-0847	84	106	11-13	5.3	
	0848-0856	86	120	13-14	6.0	
	0857-0905	88	124	14-16	6.2	
	0906-0917	90	125	16-18	6.2	
	0918-0933	92	141	18-1	7.2	
	0957-1005	94	130	1-26	6.5	
	1006-1034	96	170	26-10	8.5	
	1037-1048	98	140	9-1	7.0	
	1049-1058	100	118	6-26	5.9	
	1059-1107	102	134	26-1	6.7	150○10 360/15 37°
	1110-1116	104	129	1-9	6.5	
	1117-1126	106	140	9-1	7.0	
	1127-1136	108	129	1-26	6.5	
	1137-1145	110	127	26-1	6.4	
	1146-1153	112	136	1-9	6.8	
	1252-1300	114	140	9-1	7.0	150○10 360/15
	1301-1310	116	129	1-26	6.5	
	1311-1321	118	130	26-1	6.5	
	1322-1330	120	138	1-9	6.9	
	1331-1340	122	132	9-2	6.6	
	1355-1407	124	98	?-4	4.9	Venice P. P. plume moving S
	1410-1423	126	57	4-29	2.8	
	1426-1437	128	54	29-4	2.7	
	1439-1449	130	55	4-29	2.8	
	1450-1502	132	57	29-4	2.8	
	1506-1516	134	120	1-26	6.0	
	1517-1530	136	122	26-1	6.1	
	1531-1539	138	136	1-9	6.8	
	1540-1551	140	145	9-1	7.2	
	1552-1600	142	128	1-26	6.4	
	1601-1612	144	134	26-1	6.7	120○10 360/15 37°

Preceding page blank

LIDAR DATA SUMMARY--ST. LOUIS EXPERIMENT (Continued)

Date (1971)	Time (CST)	Run No.	No. of Shots	Route Points	Length (miles)	Weather, Remarks
3 March (Wed.)	(No observations--snow)					50⊘V4 1-3 Snow 310/15-25
4 March (Thurs.)	0450-0459	146	130	1-26	6.5	◯10 270-300 5 22°
	0518-0528	148	136	26-1	6.8	Many steam plumes around city
	0529-0537	150	136	1-9	6.8	
	0538-0543	152	125	9-13	6.3	Plume near end of run
	0544-0550	154	127	13-14	6.4	
	0551-0600	156	124	14-16	6.2	
	0601-0612	158	156	16-18	7.8	
	0613-0629	160	173	18-1	8.6	
	0643-0702	162	171	35-30	8.6	
	0703-0717	164	131	30-32	6.6	
	0718-0739	166	148	32-6	7.4	
	0743-0800	168	142	1-18	7.1	
	0801-0812	170	161	18-16	8.1	
	0813-0822	172	153	16-22	7.7	
	0823-0835	174	171	22-24	8.6	◯10 240/5 35°
	0836-0850	176	171	24-6	8.6	
	1002-1013	178	171	6-36	8.6	/⊘7H 220/5 36°
	1024-1035	180	133	36-53	6.6	Plume near start of Run 1 78
	1043-1055	182	171	38-42	8.6	
	1056-1108	184	151	42-46	7.6	
	1111-1122	186	164	46-41	8.2	
	1123-1134	188	165	41-38	8.3	
	1135-1147	190	171	38-41	8.5	
	1148-1159	192	161	41-46	8.2	
	1200-1211	194	164	46-41	8.2	Plume just to S blowing to N
	1212-1223	196	165	41-38	8.3	
	1228-1235	198	109	39-41	5.5	
	1236-1247	200	157	41-46	7.9	
	1355-1405	202	96	46-27	4.8	
5 March (Fri.)	0437-0446	204	133	1-9	6.7	⊘/10 180/5 34°
	0447-0455	206	127	9-13	6.4	
	0456-0505	208	130	13-14	6.5	
	0506-0514	210	126	14-16	6.3	
	0515-0525	212	152	16-18	7.6	
	0526-0545	214	121	18-5	6.2	
	0555-0607	216	151	1-25	7.5	
	0608-0618	218	92	25-46	4.6	
	0619-0630	220	168	46-41	8.4	
	0631-0644	222	171	41-46	8.5	
	0645-0655	224	164	46-51	8.2	
	0656-0702	226	76	51-22	3.8	
	0703-0715	228	161	22-49	8.0	Max. haze Pt. 50 to Pt. 46
	0716-0725	230	152	49-43	7.6	
	0726-0730	232	55	43-42	2.8	
	0759-0807	234	134	42-46	6.7	
	0808-0818	236	144	46-50	7.2	
	0819-0826	238	103	50-22	5.2	
	0827-0833	240	104	22-50	5.2	◯10 200/10
	0928-0940	242	171	45-40	8.6	
	0949-1000	244	171	40-45	8.6	City plume moving N up river
	1001-1013	246	171	45-50	8.6	◯10 200/10-15
6 March (Sat.)	(No observations--snow)					

Appendix C

LIDAR DATA SUMMARY--ST. LOUIS EXPERIMENT (Concluded)

Date (1971)	Time (CST)	Run No.	No. of Shots	Route Points	Length (miles)	Weather, Remarks
7 March	0424-0428	248	53	1-52	2.7	30◎10 270/15 31°
(Sun.)	0436-0446	250	129	9-13	6.5	
	0447-0455	252	129	13-14	6.5	
	0456-0505	254	127	14-16	6.4	
	0506-0515	256	156	16-18	7.8	
	0516-0530	258	149	18-1	7.5	
	0532-0541	260	130	1-26	6.5	40◑25 270/15 33°
	0542-0551	262	137	26-1	6.8	
	0552-0601	264	135	1-9	6.8	
	0602-0612	266	135	9-1	6.8	
	0613-1631	268	155	1-18	7.7	
	0632-0649	270	157	18-2	7.9	
8 March	0638-0653	272	157	1-18	7.9	◯15 300/5
(Mon.)	0654-0703	274	120	18-16	6.0	
	0709-0715	276	104	16-15	5.2	
	0725-0733	278	154	15-13	7.7	
	0753-0802	280	122	12-9	6.1	
	0803-0816	282	133	9-1	6.7	
	0817-0822	284	135	1-26	6.8	
	0823-0837	286	119	26-1	6.0	
	0838-0844	288	146	1-9	7.3	
	0845-0859	290	136	9-1	6.8	
	0900-0921	292	171	-31	8.6	
	0922-0931	294	90	31-34	4.5	
	0932-0944	296	154	34-33	7.7	
	0945-1003	298	146	33-1	7.3	
	1005-1021	300	171	1-17	8.6	
	1022-1041	302	169	17-1	8.5	◯15 320/10-15 28°
	1219-1253	304	170	---	5/min.	Stationary near EMSU site
9 March	0431-0445	306	150	1-18	7.5	100◯/◯10 130/5 30°
(Tues.)	0446-0458	308	154	18-16	7.7	
	0507-0519	310	160	16-22	8.0	
	0520-0532	312	171	22-48	8.6	
	0533-0541	314	107	48-44	5.4	
	0542-0555	316	169	44-50	8.5	
	0556-0607	318	171	50-20	8.6	
	0608-0618	320	171	20-22	8.6	
	0620-0630	322	164	22-23	8.2	
	0632-0645	324	154	23-28	7.7	
	0646-0652	326	60	28-1	3.0	
	0720-0737	328	156	1-18	7.8	
	0738-0749	330	147	18-16	7.4	
	0750-0801	332	161	16-22	8.0	100◯/◯10 130/5-10
	0802-0813	334	153	22-49	7.7	
	0814-0826	336	166	49-43	7.8	
	0859-0912	338	163	45-50	8.4	
	0913-0923	340	153	50-21	6.7	80◑10 130/10
	0924-0933	342	89	21-19	4.5	
	0934-0942	344	127	19-22	6.4	
	0943-0956	346	171	22-24	8.6	
	0957-1011	348	171	24-8	8.6	
	1012-1022	350	156	8-9	7.8	Cahokia P.P. plume
	1023-1032	352	117	9-12	5.9	Nat. Lead Co. plume
	1033-1041	354	105	12-9	5.3	Nat. Lead Co. plume
	1042-1052	356	141	9-1	7.2	Cahokia P.P. plume
	1053-1108	358	156	1-18	7.8	
	1109-1121	360	150	18-16	7.5	
	1122-1132	362	162	16-22	8.1	
	1133-1144	364	154	22-47	7.7	
	1145-1157	366	156	47-43	7.8	
	1202-1216	368	133	46-26	6.7	
	1217-1228	370	124	26-1	6.2	

Appendix D

DESIGN CONSIDERATIONS FOR AN EYE-SAFE LIDAR SYSTEM

by R. J. Allen

Appendix D

CONTENTS

1. Summary D-5

2. Introduction D-6

   a. Background D-6

   b. Current Operational Safety Procedures D-7

   c. How to Reduce the Eye Damage Probability D-8

3. Eye Safety Exposure Labels for Various Lasers D-8

4. Changes to Current Lidar Systems to Improve Safety Aspects D-12

   a. Modifying Existing Lidar Systems D-12

   b. Supplement Existing Lidar Systems with Additional Equipment D-18

5. New Lidar Systems Designed to Reduce the Eye Damage Probability D-18

   a. Wavelengths Less Hazardous to the Eye D-20

   b. Continuous-Wave (CW) Lidar System D-21

6. Concluding Remarks D-22

REFERENCES D-23

Preceding page blank

Appendix D

DESIGN CONSIDERATIONS FOR AN EYE-SAFE LIDAR SYSTEM*

1. Summary

The probability of accidental eye damage from a lidar is extremely low when adequate safety precautions are taken. Those individuals using lidar systems have developed rigid operational safety procedures; as a result, no case of eye injury has been reported despite the extensive use of lidar systems for atmospheric research. However, even with these operational precautions and the inherent low probability of eye damage, it is possible that restrictions may eventually be placed on the use of high-power lidars in urban environments as long as the eye-damage probability is nonzero. Therefore, an objective of some importance is to develop lidar systems with improved eye safety.

Typical present-day lidar systems using wavelengths in the range from 530 to 1060 nm have minimum eye-safe ranges of several kilometers. This eye-safe range is reduced to a few hundred meters for a lidar operating at considerably shorter wavelengths, but system performance is severely degraded because of the increased molecular (Rayleigh) return at these wavelengths.

Changing system parameters (increasing receiver area, increasing the transmitted beam divergence, etc.) can help to a limited extent to reduce the eye-safe range. However, most of these changes also reduce the performance of the lidar system, and thus are only feasible for short-range (1 to 2 km) observations. Many applications require long-range operations.

---

*A portion of this study was sponsored by Stanford Research Institute.

Preceding page blank

Another approach is to slave the lidar system to a microwave radar system that would automatically prevent the lidar from firing whenever an aircraft or any other object entered the air space under surveillance. This safety device would be effective for both fixed and mobile lidar operations and could be added for a modest cost.

A more expensive but ultimate solution would be the development of a completely eye-safe lidar. Erbium-glass (1540 nm), erbium-YAG (1640 nm), and holmium-YAG (2090 nm) lasers all are in an eye-safe spectral region. In addition, the higher ratio of aerosol to Rayleigh backscattering for these longer wavelengths would enhance lidar system performance over that occurring at lower wavelengths. Unfortunately, present-day detectors for these wavelengths are relatively insensitive and seriously limit the range of operations. However, this may be a good approach for short-range studies.

Continuous-wave (CW) lidar systems have distinct advantages from an eye-safety standpoint over high peak-power, Q-switched systems. A lidar system of this type, using frequency modulation to extract information from the return signal, has recently been developed and successfully tested at SRI.

2. Introduction

a. Background

Lidar systems used for atmospheric probes are focused at infinity, and energy densities produced therefore will not harm the skin. The possibility of accidental eye damage is the only safety hazard. The probability of such eye damage from a lidar is extremely low when adequate safety precautions are taken. Despite the fairly extensive use of lidar

systems for atmospheric research in the past few years, no cases of eye injury have been reported. This is partly the result of the fairly extensive operational procedures that have been developed; these procedures will be described in the next subsection. In addition, the inherent nature of a laser pulse has lessened the safety problem. Typically, the pulse takes the form of a cylinder of light, initially 15 cm in diameter and 6 m long, traveling through the atmosphere at the speed of light. Each pulse is only 20 ns (0.00000002 s) in duration, and the pulses occur approximately one second apart for a typical system. The lidar is designed to totally prevent any emission of stray laser light from any direction other than that in which the unit is pointed.

b. Current Operational Safety Procedures

Operational procedures during observational periods with the existing lidar systems have been established to minimize the probability of accidental hazard to all within the range of the lidar. Our standard safety procedures for field experiments, which have been proved worthy by use in many projects, are as follows:

- Mechanical stops are placed on the equipment to confine the pointing angles to a specific field of view.
- Aiming and firing are under the supervision of an operator who uses an aiming telescope to monitor the field of view as well as a large surrounding area. This operator is the only person who can fire the lidar, and he does not allow the unit to be triggered until he is sure the area is clear.
- Another observer equipped with binoculars also keeps the entire firing area under surveillance. This observer is equipped with an override switch to prevent firing of the lidar when any human activity (airplane, ship, and the like) is sighted in the firing area.

- When not being fired, the lidar is always rendered completely safe by a switch that discharges the capacitor bank furnishing high voltage to the laser flash lamps. Without this high voltage supply, the lidar cannot be fired.
- As an additional precaution, the stowage position of the lidar is such that it is never pointed at eye level.

However, despite such operational precautions and the inherent low probability of eye damage, it is possible that the use of high-power lidars in urban environments may eventually be restricted to some degree as long as the eye-damage probability is nonzero.

c. How to Reduce the Eye Damage Probability

Eye damage probability can be reduced by designing a new lidar system that operates with an energy density wavelength less hazardous to the eye. Or, certain changes or additions could be made to the existing lidar equipment, some of which cause degradation in system performance. Each of these methods will be considered by comparing selected eye-safety improvement criteria with the degradation in observational performance using present-day lidars as a reference.

3. Eye Safety Exposure Levels for Various Lasers

If the energy density of the incident laser beam is of sufficient magnitude and of particular wavelength, damage can result in different parts of the eye. The damage produced by radiation within the 400 to 1350 nm* band is primarily to the retina; outside this band, the damage is primarily to the cornea or lens of the eye. However, the energy

*1000 nm = 1 micron.

density of the incident beam required to produce damage to the cornea is several orders of magnitude greater than the corresponding damage levels for the retina, at the most sensitive wavelengths.

The use of Q-switched lasers is basically more dangerous than CW systems. The absorption of energy in the pigmented tissues of each cell of the eye occurs in such a short time that the heat generated by the absorbing layers cannot be conducted to the surrounding media. Thus, the temperature of the cells can reach high values with low-energy input. For longer exposures that can result from CW lasers, for example, thermal conduction from the absorbing layers to the surrounding media plays a strong role; consequently, higher energies are required to raise the temperature sufficiently to cause damage.

Damage threshold levels have been obtained by exposing a large number of animals (such as rhesus monkeys) to laser radiation, observing lesions produced optholmoscopically, and extrapolating the results to humans. There have also been limited exposures to human subjects. On the basis of this data, a number of agencies have made recommendations for safe levels. The recommended safe levels, however, in some instances disagree by several orders of magnitude (Clarke, 1970).

The criteria used as a measure of eye safety for CW lasers is the ratio of maximum eye-safe power density (I_s) to the mean laser power density ($\bar{I}_e$) incident upon the eye for selected exposure times. When $I_s/\bar{I}_e \geq 1$, the lidar is defined as safe for the particular parameters involved. For pulsed lasers, the ratio of the <u>energy</u> densities are usually used, with the eye-safe energy density (J_s) being a function of the mode of the pulse operation (short-pulse 1 to 100 ns, or long-pulse around 1 ms). The minimum eye-safe range (R_e) in the absence of thermal turbulence can be calculated by using these criteria and the inverse square law from

$$R_e = \frac{2}{\theta_t}\left(\frac{\bar{P}_t T_e}{\pi I_s}\right)^{1/2} \qquad \text{CW lasers} \qquad \text{(D.1)}$$

$$R_e = \frac{2}{\theta_t}\left(\frac{\bar{P}_t \tau T_e}{\pi J_s}\right)^{1/2} \qquad \text{Pulsed lasers} \qquad \text{(D.2)}$$

where $\bar{P}_t$ is the power radiated by the transmitter averaged over the pulse duration, T_e is the atmospheric transmission between the lidar and exposed eye, θ_t is the full divergence plane angle of the transmitted beam in radians, and τ the transmitted pulse duration.

Table D-1 contains a summary of the minimum eye-safe range for typical lidar systems as calculated from Eqs. (D.1) and (D.2). The eye-safe densities were obtained from the sources indicated and were grouped according to wavelength and type of laser. Eye-safe energy density levels indicated for 1540 nm were determined by relating owl-monkey data at 694.3 and 1540 nm to the established safe exposure level for 694.3 nm. Values for 530 nm were obtained by dividing the 694.3 nm values by two. Levels indicated for 347.1 nm were obtained during experiments by Vassiliadis (1971). The levels shown in the table are the threshold data divided by a safety factor of 10.

The minimum eye-safe ranges were calculated by assuming the same average power for comparison purposes. Both day and night operation are tabulated for a clear standard atmosphere (worst case). Considerable improvement in the minimum eye-safe range can be noted when the transmitter beam divergence (θ_t) is increased from 0.5 mrad to 4 mrad. However, this decreases the lidar system performance during day-time operation. If only eye-safety is considered, the erbium and carbon dioxide laser appear to show the most promise.

Table D-1

PERMISSIBLE EXPOSURE LEVELS AT THE CORNEA AND COMPARISON OF EYE-SAFE EXPOSURE DISTANCES AT VARIOUS WAVELENGTHS

Wavelength λ	Type Laser	Part of Eye*	Q-Switched (1 to 100 ns) Eye-Safe Energy Density, J_s ($\mu j/cm^2$)		CW (exposure 1 to 10 ms) Eye-Safe Power Density, I_s (W/cm^2)		Minimum Eye-Safe Range (R_e) for Systems with Same Average Power† (clear standard atmosphere)			
							θ_t = 0.5 mrad		θ_t = 4 mrad	
			3 mm Day Pupil	7 mm Night Pupil	3 mm Day Pupil	7 mm Night Pupil	Day	Night	Day	Night
347.1 nm	2nd Harmonic of ruby	C	1.4×10^6 (3)	1.4×10^6 (3)	--	--	13.4 m	13.4 m	1.7 m	1.7 m
		R	> 8500 (3)	> 1500 (3)	--	--	< 164 m	< 366 m	< 21.5 m	< 50.7 m
488 and 514.5 nm	Argon	R	--	--	0.14 (1)	0.026 (1)	42.3 m	97.2 m	5.3 m	12.3 m
530 nm	2nd Harmonic of neodymium	R	5.3 (3)	0.98 (3)	--	--	3.7 km	11.2 km	759 m	1.54 km
632.8 nm	Helium-neon	R	--	--	0.14 (1)	0.026 (1)	42.4 m	97.5 m	5.35 m	12.4 m
694.3 nm	Ruby	R	10.6 (1)	1.95 (1)	--	--	3.16 km	5.85 km	566 m	1.2 km
1060 nm	Neodymium	R	638 (1)	117 (1)	--	--	591 m	1.3 km	78.3 m	180.7 m
1540 nm	Erbium-glass		7×10^6 (2) (1)	7×10^6 (2) (1)	--	--	6 m	6 m	0.8 m	0.8 m
10600 nm	Carbon dioxide	C	--	--	8 (1)	8 (1)	5.6 m	5.6 m	0.7 m	0.7 m

*C--Cornea; R--Retina.

†0.5 W (assumed obtainable for helium-neon).

Sources: "Laser Health Hazards Control," Air Force Manual 161-8 (1 April 1969).
"Keep an Eye on Erbium," Laser Focus (January 1971).
A. Vassiliadis, et al., "Ocular Laser Threshold Investigations," SRI Project 8209, U.S. Air Force (March 1971).

4. Changes to Current Lidar Systems to Improve Safety Aspects

Certain changes may be able to be made to typical lidars (such as the SRI Mark V or Mark IX and the EPA Mark VIII) that will result in a reduction of the minimum eye-safe range (R_e). These include modifying the equipment or supplementing the equipment with additional devices. Each of these general categories will be discussed separately without considering the economics entailed.

a. Modifying Existing Lidar Systems

Modifications to the lidar system (such as increasing the diameter of the parabolic mirror within the receiver) and the effect that each change has on the minimum eye-safe range can best be studied by combining the lidar performance equations (Northend, Honey, and Evans, 1966; Ross, 1966) with the eye-safety Equation (D.2) and then solving for the ratio of the initial (R_{eo}) to the reduced (R_e) minimum eye-safe ranges. This produces the equations shown in Table D-2 for signal, background, and detector noise limited cases.* The lidar systems can be modified by

---

*Unwanted currents produced in the output of a laser detector can be caused by background, signal, detector, and thermal noises. When one of these noise currents predominates (say greater than 10:1), terms in the lidar equations associated with these lessor currents may be dropped. This greatly simplifies these equations.

The criteria for determining which of the noise currents limit operation of the lidar system are listed in Table D-3. In general, when the detector has high current gain such as a PMT (typically 10^6), the thermal noise terms can be dropped. When operating a lidar with a bright day-sky or cloud background, the background noise is the controlling term for wavelengths of 694.3nm and below. At night, backgrounds will be extremely low. Detector noise can be the limiting factor when operating at wavelengths around 1060 nm during the night. Improvement in performance may be obtained by cooling the detector in this case.

Table D-2

PARAMETERS INFLUENCING THE MINIMUM EYE-SAFE RANGE ($\theta_{to} \leq \theta_{ro}$)

Signal noise limited

$$\frac{R_{eo}}{R_e}(i_{sn}) = \frac{\theta_t}{\theta_{to}}\left(\frac{J_s}{J_{so}}\right)^{1/2}\left(\frac{P_{to}\,\tau_o}{P_t\,\tau}\cdot\frac{T_{eo}}{T_e}\right)^{1/2} = \frac{\theta_t}{\theta_{to}}\cdot\frac{R_{xo}}{R_x}\,\frac{\left(I_s/i_{sn}\right)_o}{\left(I_s/i_{sn}\right)}\cdot\frac{D_r}{D_{ro}}\left(\frac{q\,\eta_r}{q_o\,\eta_{ro}}\cdot\frac{B_{Do}}{B_D}\right)^{1/2}\left(\frac{J_s}{J_{so}}\cdot\frac{\beta' T_x^2}{\beta'_o T_{xo}^2}\cdot\frac{T_{eo}}{T_e}\right)^{1/2} \quad (D.3)$$

Background noise limited

$$\frac{R_{eo}}{R_e}(i_{bn}) = \frac{\theta_t}{\theta_{to}}\cdot\frac{R_{xo}}{R_x}\left[\frac{\left(I_s/i_{bn}\right)_o}{\left(I_s/i_{sn}\right)}\cdot\frac{\theta_{ro}}{\theta_r}\cdot\frac{D_r}{D_{ro}}\right]^{1/2}\left[\frac{q\,\eta_r}{q_o\,\eta_{ro}}\cdot\frac{B_\lambda}{B_{\lambda_o}}\cdot\frac{B_{Do}\,\Delta\lambda_o}{B_D\,\Delta\lambda}\right]^{1/4}\left[\frac{J_s}{J_{so}}\cdot\frac{\beta' T_x^2}{\beta'_o T_{xo}^2}\cdot\frac{T_{eo}}{T_e}\right]^{1/2} \quad (D.4)$$

Detector noise limited

$$\frac{R_{eo}}{R_e}(i_{dn}) = \frac{\theta_t}{\theta_{to}}\cdot\frac{R_{xo}}{R_x}\cdot\frac{D_r}{D_{ro}}\left[\frac{\left(I_s/i_{dn}\right)_o}{\left(I_s/i_{dn}\right)}\cdot\frac{q\,\eta_r}{q_o\,\eta_{ro}}\right]^{1/2}\left[\frac{B_{Do}\,I_{dco}}{B_D\,I_{dc}}\right]^{1/4}\left[\frac{J_s}{J_{so}}\cdot\frac{\beta' T_x^2}{\beta'_o T_{xo}^2}\cdot\frac{T_{eo}}{T_e}\right]^{1/2} \quad (D.5)$$

Note: D_r is the diameter of the receiver optics, and R_{eo} values are listed in Table D-1.

See Section D.4.a. that follows for an explanation of these symbols.

Table D-3

CRITERIA FOR DETERMINING NOISE CONDITIONS

Background Noise (limited)	Signal Noise (limited)	Detector Noise (limited)	Terminal Noise (limited)
$\frac{P_b}{P_s} \geq \frac{10}{1}$	$\frac{P_b}{P_s} \leq \frac{1}{10}$	$\frac{qP_b}{I_{dc}} \leq \frac{1}{10}$	$\frac{e\mu^2 R_L qP_b}{kT} \leq \frac{1}{10}$
$\frac{qP_b}{I_{dc}} \geq \frac{10}{1}$	$\frac{qP_s}{I_{dc}} \geq \frac{10}{1}$	$\frac{qP_s}{I_{dc}} \leq \frac{1}{10}$	$\frac{e\mu^2 R_L qP_s}{kT} \leq \frac{1}{10}$
$\frac{e\mu^2 R_L qP_b}{kT} \geq \frac{10}{1}$	$\frac{e\mu^2 R_L qP_s}{kT} \geq \frac{10}{1}$	$\frac{e\mu^2 R_L I_{dc}}{2kT} \leq \frac{10}{1}$	$\frac{e\mu^2 R_L I_{dc}}{2kT} \leq \frac{1}{10}$

where

$$\frac{P_b}{P_s} = \frac{2\pi^2}{c} \cdot \frac{\vartheta_r^2 \Delta\lambda}{(P_t \tau)} \cdot \frac{R_x^2 B_\lambda}{B' T_x^2}$$

$$\frac{qP_b}{I_{dc}} = \frac{\pi}{4} \frac{q\vartheta_r^2 \beta_\lambda A_r \eta_r \Delta\lambda}{I_{dc}}$$

$$\frac{qP_s}{I_{dc}} = \frac{c}{8\pi} \cdot \frac{q(P_t \tau) A_r \eta_r \beta' T_x^2}{I_{dc} R_x^2}$$

Note: See Section D.4.a. that follows for an explanation of these symbols.

changing wavelengths (frequency doubling), or by maintaining the same wavelength and changing other parameters. Each will be considered separately.

1) Without Changing Wavelength

When modifications are made without changing wavelength, the ratio of the initial to changed (or changed to initial) values of the following terms equals one and may be dropped from consideration: eye-safe energy density (J_s), atmospheric transmission between the lidar and exposed eye (T_e), volume backscattering coefficient (β'), two-way atmospheric transmission (T_x^2), and background radiance of the scattered solar radiation (B_λ). From the remaining terms, it may be concluded that the minimum eye-safe range (R_e) is reduced as the square root of a reduction in the transmitted power output (P_t). However, reducing R_e by this method also reduces the maximum range (R_x) of detection of a given target in direct proportion.

On the other hand, R_e may be reduced as $P_t^{1/2}$ without changing the performance of the lidar system (i.e.,

$$I_{so}/i_n \div I_s/i_n = 1 \text{ and } R_{xo}/R_x = 1)$$

- For the signal noise limited case; R_e is reduced
  - --Directly in proportion to the increase in the diameter of the receiver optics, D_r
  - --Directly as the square root increase in the PMT cathode sensitivity, q
  - --Directly as the square root increase in the transmission efficiency of the receiver optics, η_r

--Inversely as the square root increase in the bandwidth of the electronics, B_D

- For the background noise case, R_e is reduced as

$$D_r^{1/4}, \quad q^{1/4}, \quad \eta_r^{1/4}, \quad 1/B_\lambda^{1/4}, \quad 1/B_D^{1/4} \text{ and } 1/\Delta\lambda^{1/4}$$

- For the detector noise limited case, R_e reduces as

$$D_r, \quad q^{1/2}, \quad \eta_r^{1/2}, \quad 1/B_D^{1/4}, \text{ and } 1/I_{dc}^{1/4}$$

If the existing lidars were modified to accept an 8-inch diameter mirror, P_t could be reduced and the system would still have the same performance and R_e would be reduced by 25 percent for the signal and detector noise limited cases but only by 7 percent for the background noise limited case.

If the RCA 7265 PMT were replaced with the new RCA C31034, R_e could be reduced by 55 percent for the signal and detector noise limited cases and 33 percent for the background noise limited case.

Decreasing the bandwidth of the postdetection electronics while helping the eye-safe problem would further limit the spatial resolution of the structure within the aerosol under observation; therefore, this should not be considered. Probably not much room for improvement exists in the transmission efficiency of the receiver optics other than perhaps with the narrow-band filter.

Decreasing the predetection bandwidth ($\Delta\lambda$) must be within the constraint of $\Delta\lambda \gg B_D$ (Ross 1966). The Mark VIII optical filter is 11.3 Å wide at its 1/2 - maximum transmission point that converts to a

frequency of 2.65 X 10^{17} Hz and certainly meets the constraint. If $\Delta\lambda$ is reduced to 5 Å, R_e reduces by 18.4 percent for the background limited case.

2) By Frequency Doubling

Frequency doubling techniques have improved greatly in the last few years. A second harmonic with a power output of 4 percent of the fundamental was all that could be obtained around 1968. Now power output of 40 percent is achievable.

An examination of Table D-1 indicates that the second harmonic of ruby is very attractive from the eye-safe standpoint. Also, an examination of available PMT's indicates an advantage at these shorter wavelengths. However, there is an overriding limitation. The prime function of a lidar working at this wavelength is to detect aerosols by backscattering techniques and to distinguish between clear air (Rayleigh) and the aerosol concentration. Therefore, the ratio of coefficients for these two types of scattering is an important consideration. An examination of this ratio indicates that operation at the second harmonic of ruby is not a good choice for sea level operation.

The second harmonic of neodymium is very close to the center of the visible region, and as can be seen from Table D-1, the minimum eye-safe range is greatly increased. The PMT detector has always been the weak link in the neodymium lidar system. A big improvement is obtained by going to the second harmonic. However, this performance gain is achieved only by increasing the eye hazard, which makes the change to the second harmonic of neodymium unfeasible.

b. Supplement Existing Lidar Systems with Additional Equipment

The probability of accidental eye damage could be reduced by controlling the lidar firing with a microwave radar system slaved to the lidar. When an aircraft enters the air space under surveillance, the radar system would automatically prevent the lidar from firing by some interlocking technique. The beam divergence of the radar ($\theta_R + \Delta\theta_R$) would have to be greater than that of the lidar (θ_t) by an amount such that an aircraft traveling at a velocity $v_a + v_a \cos \alpha$ at a given range R from the lidar would not be able to enter a lidar beam moving at an angular rate of $\pm \omega$ without being detected by at least N pulses of the radar. Specifically (Figure D-1),

$$(PRF)_R > \frac{N K v_a (1 + \cos \alpha) + R\omega}{R(\theta_R + \Delta\theta_R - \theta_t)(1 + \cos \alpha)}$$

Since θ_t is characteristically much less than θ_R for existing lidar systems, these conditions are easily obtainable for radar detection of aircraft to ranges greater than the minimum eye-safe range.

5. New Lidar Systems Designed to Reduce the Eye Damage Probability

If a new class of lidar systems were to be constructed with the prime consideration being eye safety, several different approaches show promise. These include selecting wavelengths less hazardous to the eye, using modulated CW lasers, incorporating pulse integration techniques, and selecting Q-switched or dye lasers with lower energies but compensating for performance loss by varying other parameters as discussed in the previous section. New lidar system considerations will now be presented disregarding cost factors at this time.

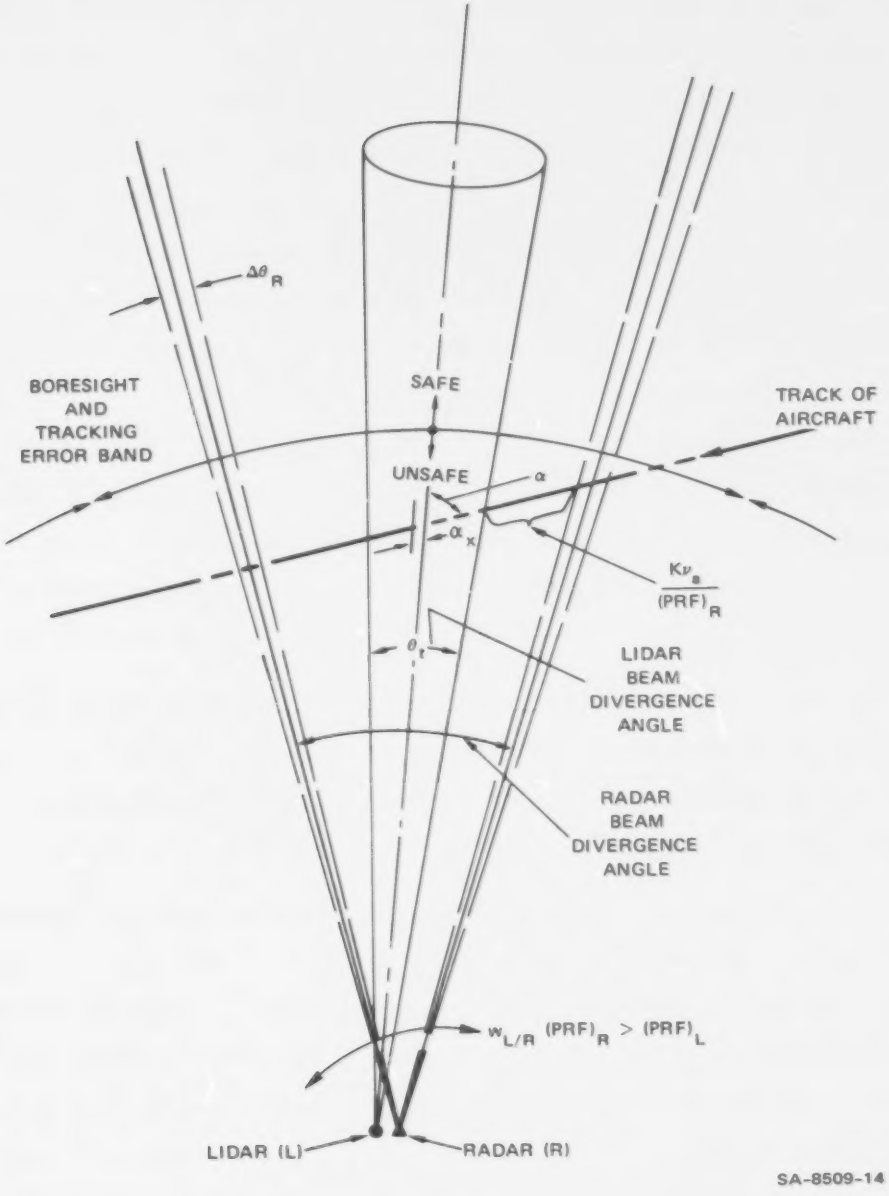

FIGURE D-1 CO-LOCATED RADAR SLAVED TO LIDAR POSITION CONTROLLER

a. Wavelengths Less Hazardous to the Eye

As can be seen by examining Table D-1, an erbium laser operating at a wavelength of 1540 nm is quite favorable from an eye-safety standpoint. A major problem in designing a lidar system in the 1540 nm region is with the detector. Noise equivalent power (NEP) values and time constants are higher than for detectors used in existing lidar systems resulting in poorer receiver performance. Some gain can be realized by cooling the detector, but this means increases in primary power and size. This can be offset somewhat, however, because higher transmitted energies can be tolerated. As was indicated in Table D-1, a ruby system with $\bar{P}_t \tau = 0.5$j and $\theta_t = 0.5$ mrad has a daytime minimum eye-safe range (R_e) = 3.16 km; whereas, for an erbium laser with the same characteristics, R_e = 10 m. As reported in Laser Focus (January 1971), a 100-mj, 50-ns erbium laser has been built. The availability of higher energy units in the near future is unknown; however, it should be safe to assume that a 1.4 j laser head could be designed.

Other lasers in the near-IR region that might be investigated are the erbium-yag at 1640 nm and holmium-yag at 2090 nm. The ratio of aerosol to Rayleigh backscattering would favor lidars around these wavelengths over those at lower wavelengths.

In the UV region, on the other hand, the detector performance for a lidar system using a second harmonic ruby laser is somewhat improved over that for ruby and is greatly improved over neodymium wavelengths. The minimum eye-safe range for a second harmonic ruby 0.5-j, 0.5-mrad laser is about 164 m during the day and 366 m at night, which is not as good as the erbium. Operation at this wavelength is within an atmospheric window as is the case with erbium. The ratio of aerosol to Rayleigh backscattering, however, would discourage the use of the second harmonic of ruby.

b. Continuous-Wave (CW) Lidar System

As was indicated earlier (Table D-1), a CW laser has a distinct advantage from an eye-safety standpoint over a high-peak-power Q-switched system. A CW system with the same average power output as a pulsed laser in the 600-nm region would improve the daytime minimum eye-safe range from 3.16 km down to 42.4 m.

To extract information from the return signal, the CW wave must be modulated. From an examination of the different modulation methods (pulse, amplitude, frequency) discussed in the open literature,* it appears that the frequency modulation (FM) techniques show the most promise. Information as a function of range is obtained by changing the modulation frequency to be slow enough that it does not return to the same frequency in the time it takes the light energy to go back and forth at the maximum range of interest. The detected return signal is then heterodyned with the modulation frequency to produce a difference frequency. The frequency of this difference (or beat) is then indicative of the range. The amplitude of the received CW carrier is a function of the scattering medium within the indicated range interval.

An SRI study (Jackson, 1970) has been conducted showing the feasibility of this technique for day or nighttime measurement of plume opacity. This system, designed for air pollution control monitoring, has a simple readout indicating the Ringelmann number. A modulation frequency deviation of 2.5 MHz was considered, producing a range resolution on the order of 30 meters. A similar type system could undoubtedly be designed for general atmospheric probing with a PPI type display such as used in the Mark VIII lidar. The sweep of the PPI scope would be synchronized with the FM modulation and the intensity of the scope modulated by the amplitude of the return signal.

---

*For example, see Ross (1966).

6. Concluding Remarks

Lidar has proved to be a most valuable instrument for many atmospheric applications over the past ten years. It is true that a very small but finite eye hazard exists when lidar systems are used in the atmosphere. However, it should be remembered that the probability of accidental eye damage is extremely low when proper operational precautions are applied. This fact appears to make any restrictions on lidar use which reduces its capabilities for atmospheric studies both unnecessary and undesirable. In addition, as discussed here, a number of additional steps may be taken to further reduce the eye-damage probability or to eliminate it completely.

In light of this technical discussion, the modest cost of some of these safety steps, such as the addition of a small microwave radar to lidar systems, appears to make them worthwhile.

Appendix D

REFERENCES

Clarke, A. M., "Ocular Hazards from Lazer and Other Optical Sources," Critical Reviews in Environmental Control, Vol. 1, pg. 307 (1970).

Jackson, D. W., "Development of a CW Lidar for the Remote Measurement of Smoke-Plume Opacity," SRI Report ELD 69-165, Stanford Research Institute, Menlo Park, California (22 January 1970).

"Keep an Eye on Erbium," Laser Focus (January 1971).

"Lazer Health Hazards Control," Air Force Manual 161-8 (1 April 1969).

Northend, C. A., Honey, R. C., and Evans, W. E., "Laser Radar (Lidar) for Meteorological Observations," Review of Scientific Instruments, Vol. 37, No. 4, pp. 393-400 (April 1966).

Ross, M., Laser Receivers (John Wiley and Sons, Inc., New York, New York, (1966).

Vassiliadis, A., et al., "Ocular Laser Threshold Investigations," SRI Project 8209, U.S. Air Force (March 1971).